

Washington University in St. Louis
Washington University Open Scholarship

All Theses and Dissertations (ETDs)

Winter 1-1-2012

Multi-contrast Photoacoustic Microscopy

Junjie Yao

Washington University in St. Louis

Follow this and additional works at: <https://openscholarship.wustl.edu/etd>

Recommended Citation

Yao, Junjie, "Multi-contrast Photoacoustic Microscopy" (2012). *All Theses and Dissertations (ETDs)*. 1025.
<https://openscholarship.wustl.edu/etd/1025>

This Dissertation is brought to you for free and open access by Washington University Open Scholarship. It has been accepted for inclusion in All Theses and Dissertations (ETDs) by an authorized administrator of Washington University Open Scholarship. For more information, please contact digital@wumail.wustl.edu.

WASHINGTON UNIVERSITY IN ST. LOUIS

School of Engineering & Applied Science
Department of Biomedical Engineering

Dissertation Examination Committee:

Lihong Wang, Chair
Mark Anastasio
Dennis Barbour
Joseph Culver
Jin-Moo Lee
Lan Yang

Multi-contrast Photoacoustic Microscopy

by

Junjie Yao

A dissertation presented to the
Graduate School of Arts and Sciences
of Washington University in
partial fulfillment of the
requirements for the degree
of Doctor of Philosophy

December 2012

St. Louis, Missouri

Contents

List of Figures	vii
List of Tables	x
Acknowledgements	xi
Abstract	xii
1. Introduction	1
2. Optical-resolution photoacoustic microscopy	2
3. Multi-contrast photoacoustic microscopy	6
3. 1. Photoacoustic microscopy of capillaries enhanced by Evans blue	6
3.1.1. Methods	7
Animal preparation	7
Mode of injection of EB	8
3.1.2. Results	8
Spatially continuous capillary imaging using EB as a contrast agent	8
Dynamics of EB diffusion out of the blood stream	10
Dynamics of the EBA clearance	12
3.1.3. Conclusions and discussion	14
3.2. Photoacoustic microscopy in transverse blood flow imaging	15
3.2.1. Methods	16
3.2.2. Results	20

Phantom study.....	20
Animal study.....	23
3.2.3. Conclusions and discussion	27
3.3. Photoacoustic microscopy in total blood flow imaging.....	27
3.3.1. Methods.....	28
3.3.2. Results.....	30
Phantom study.....	30
Animal experiment.....	33
3.3.3. Conclusions and discussion	35
3.4. Photoacoustic microscopy in metabolic rate of oxygen measurement	36
3.4.1. Methods.....	39
Hyperthermia experimental protocol	40
Tumor cell culture.....	40
Inoculation of tumor cells	41
Hemodynamics measured by mPAM	41
Melanoma volume estimation using mPAM	43
Fitting for the profile of blood flow speed.....	43
Statistical analysis.....	44
3.4.2. Results.....	44
MRO ₂ quantification under normothermia	44

Change in MRO_2 induced by systemic hyperthermia	45
Change in MRO_2 induced by local cryotherapy	47
Early cancer detection by measuring tumor-induced change in MRO_2	49
3.4.3. Conclusions and discussion	55
4. Improvements in photoacoustic microscopy	57
4.1. Double illumination photoacoustic microscopy	57
4.1.1. Methods.....	58
4.1.2. Results.....	60
Phantom study.....	60
Animal study	62
4.1.3. Conclusions and discussion	64
4.2. MEMS scanning mirror based fast scanning photoacoustic microscopy	65
4.2.1. Methods.....	66
4.2.2. Results.....	69
Phantom study.....	69
Animal study	71
4.2.3. Conclusions and discussion	74
5. Biomedical applications of multi-contrast photoacoustic microscopy (tomography)	75
5.1. Immediate alterations in intestinal oxygen saturation and blood flow following massive small bowel resection as measured by photoacoustic microscopy	76

5.1.1. Materials and methods	77
Experimental design.....	77
Operative technique	78
Intestinal sO ₂ and blood flow measured by photoacoustic microscopy	78
Statistical analysis.....	79
5.1.2. Results.....	79
Arterial and venous oxygen saturation	79
Tissue oxygen extraction	81
Arterial and venous blood flow.....	82
5.1.3. Conclusions and discussion	83
5.2. Non-invasive photoacoustic tomography and microscopy of mouse brain metabolism <i>in vivo</i>	86
5.2.1. Materials and methods	88
2-NBDG.....	88
Noninvasive photoacoustic computed tomography (PACT)	89
Optical-resolution photoacoustic microscopy (OR-PAM)	89
Fluorescence imaging	90
Animal preparation	91
Forepaw stimulation.....	92
Image co-registration	93

Signal processing	93
5.2.2 Results.....	96
PACT of 2-NBDG and blood phantom	96
PACT of mouse brain	97
PACT of cortical responses to forepaw stimulations.....	98
Fluorescence imaging of cortical responses to forepaw stimulations.....	101
5.2.3. Conclusions and discussion	102
6. Future work.....	104
References.....	107

List of Figures

Figure 1. Schematic of second-generation of optical-resolution photoacoustic microscopy	3
Figure 2. EB enhanced photoacoustic imaging of mouse ear microvessels	9
Figure 3. Dynamics of EB diffusion out of the blood stream into surrounding tissue.	11
Figure 4. Clearance dynamics of EBA..	12
Figure 5. Quantitative analysis of EBA clearance.	13
Figure 6. Probe-beam geometry for the transverse flow measurement.	17
Figure 7. Sequential A-scans used to calculate the bandwidth broadening.	17
Figure 8. Bidirectional scanning to determine the flow direction.	19
Figure 9. Photoacoustic flow measurement on microsphere phantom..	21
Figure 10. Photoacoustic flow imaging of microsphere phantom.	22
Figure 11. PA imaging of sO ₂ and blood flow in a mouse ear.	24
Figure 12. Quantitation of PA flow measurement in mouse ear.	25
Figure 13. Blood flow measurement in a chicken embryo.	26
Figure 14. Total flow measurement on bovine blood.	31
Figure 15. Quantification of total flow measurement with fixed Doppler angle.	32
Figure 16. Doppler angle measurement on the bovine blood phantom.	33
Figure 17. Three-dimensional PAM of a mouse ear.	34
Figure 18. Total flow measurement in mouse ear.	35
Figure 19. mPAM measurements of sO ₂ and blood flow in the mouse ear.	39
Figure 20. Label-free quantification of metabolic rate of oxygen (MRO ₂) <i>in vivo</i>	45
Figure 21. mPAM measurement of hemodynamic responses to a hyperthermic challenge	47
Figure 22. mPAM monitoring of hemodynamic responses after cryotherapy.	48

Figure 23. mPAM quantification of blood flow rate within 30 days after the treatment.	49
Figure 24. mPAM detection of early-stage melanoma by measuring MRO_2	50
Figure 25. mPAM measurements in absolute units	51
Figure 26. mPAM differentiation of blood vessels and melanoma.	52
Figure 27. Histological validation of melanoma detection.	53
Figure 28. mPAM detection of early-stage glioblastoma by measuring MRO_2	54
Figure 29. Histological validation of glioblastoma detection.	55
Figure 30. Label-free mPAM of hypermetabolism and hyperoxia of early stage cancer	56
Figure 31. . Schematic of DI-PAM. d1,2; Rayleigh range.	59
Figure 32. Lateral resolution under double illumination illumination.....	61
Figure 33. Penetration depth of double-illumination PAM.	61
Figure 34. DI-PAM of mouse ear in vivo.	63
Figure 35. DI-PAM of the small intestine of a C57BL/6 mouse in vivo.....	64
Figure 36. Schematic of MEMS-OR-PAM.	68
Figure 37. MEMS-scanning mirror.....	69
Figure 38. Line spread function used to measure the lateral resolution of the system	70
Figure 39. MEMS-OR-PAM imaging depth	70
Figure 40. Scanning trace correction of MEMS-OR-PAM.	71
Figure 41. MEMS-OR-PAM of blood flow dynamics of the vasculature in a mouse ear.....	72
Figure 42. MEMS-OR-PAM of flow dynamics of carbon particles.....	74
Figure 43. Oxygen saturation (sO_2) of the terminal mesenteric vessel	80
Figure 44. Photoacoustic microscopy images of intestinal microvascular structure	81
Figure 45. Tissue oxygen utilization pre-operatively, post-sham, and post-SBR	82

Figure 46. Blood flow of the terminal mesenteric vessel	83
Figure 47. 2-NBDG (C ₁₂ H ₁₄ N ₄ O ₈).	88
Figure 48. Photoacoustic and fluorescence imaging systems.	91
Figure 49. Time course of forepaw stimulation.	93
Figure 50. Multi-wavelength PACT <i>in vitro</i> and <i>in vivo</i>	97
Figure 51. High-resolution OR-PAM imaging of the mouse brain after PACT imaging.	98
Figure 52. PACT of the cortical responses to forepaw stimulations.	99
Figure 53. Quantification of the cortical region covered by responding vessels.	100
Figure 54. Correlation of the hemodynamic response and glucose response.	101
Figure 55. Fluorescence imaging of mouse brain responses to forepaw stimulations.	102

List of Tables

Table 1. Comparison of fast scanning methods.....	66
---	----

Acknowledgements

I'd like to thank my advisor, Dr. Lihong Wang, whose mentoring and guidance is always the key power that drives me through my PhD study. In addition to the academic supervising, Dr. Wang also helps me to set up a high ethical standard which I will benefit from for my life. I'd also appreciate useful discussions and help from all my lab members, especially Dr. Konstantin Maslov, Dr. Lidai Wang, Chi Zhang, Dr. Dakang Yao, Dr. Song Hu, Dr. Amos Danielli, Arie Krumholz and Dr. Amy Winkler. This work was sponsored by National Institutes of Health (NIH) grants R01 EB000712, R01 EB008085, R01 CA134539, U54 CA136398, R01 CA157277, and R01 CA159959.

ABSTRACT OF THE DISSERTATION

Multi-contrast Photoacoustic Microscopy

by

Junjie Yao

Doctor of Philosophy in Biomedical Engineering

Washington University in St. Louis, 2012

Professor Lihong V. Wang, Chairperson

Photoacoustic microscopy is a hybrid imaging modality with high spatial resolution, moderate imaging depth, excellent imaging contrast and functional imaging capability. Taking full advantage of this powerful weapon, we have investigated different anatomical, functional, flow dynamic and metabolic parameter measurements using photoacoustic microscopy. Specifically, Evans-blue dye was used to enhance photoacoustic microscopy of capillaries; label-free transverse and axial blood flow was measured based on bandwidth broadening and time shift of the photoacoustic signals; metabolic rate of oxygen was quantified *in vivo* from all the five parameters measured by photoacoustic microscopy; whole cross-sectional imaging of small intestine was achieved on a double-illumination photoacoustic microscopy with extended depth of focus and imaging depth; hemodynamic imaging was performed on a MEMS-mirror enhanced photoacoustic microscopy with a cross-sectional imaging rate of 400 Hz. As a maturing imaging technique, PAM is expected to find new applications in both fundamental life science and clinical practice.

1. Introduction

For centuries, the development of optical microscopes has revolutionized fundamental life science and clinical practice [1]. By magnifying minuscule cellular and subcellular features, optical microscopes provide a powerful tool for studying tissue components and their dynamic interactions. Its excellent imaging contrast in soft tissue has made optical microscopy the most widely used imaging modality in the biomedical community [1].

The visual power of optical microscopy relies on sharp optical focusing. Such power is rapidly reduced as photons travel deeper into biological tissue, a highly scattering medium for electromagnetic waves in the optical spectral range. When photons reach the optical diffusion limit (~ 1 mm in tissue), they have typically undergone tens of scattering events, which randomize the photon paths and thus prevent tight focusing [2]. Although modern optical microscopic techniques have released biologists from the confines of ten-micrometer-thick *ex vivo* tissue slices to a world of volumetric *in vivo* tissue, optical microscopy is still challenged to image at depths beyond the optical diffusion limit while maintaining high resolution. For decades, engineers have made scant progress by using pure optical approaches to fight scattering. Fortunately, the emerging technique of photoacoustic tomography (PAT) has pointed out a new direction, converting photon energy into ultrasound energy on the basis of the photoacoustic effect [3-14].

In PAT, as photons travel in tissue, some of them are absorbed by biomolecules and their energy is partially or completely converted into heat. The heat then induces an initial pressure rise, which propagates in tissue as a wideband acoustic wave [15-17]. An ultrasonic transducer or transducer array detects the acoustic wave to form an image, which maps the original optical energy deposition in the tissue. Since ultrasonic scattering by tissue ($\sim 1.2 \times 10^{-3} \text{ mm}^{-1}$ in human skin at 5 MHz) [18] is more than three orders of magnitude weaker than optical scattering ($\sim 10 \text{ mm}^{-1}$ in human skin at 700 nm) [2], PAT can achieve fine acoustic resolution at depths beyond the optical diffusion limit. In addition, since the photoacoustic signal amplitude is proportional to the optical energy deposition, PAT is sensitive to the rich optical absorption contrast of tissue.

Several previous Review articles have given comprehensive coverage of PAT, focusing on instrumentation [4-6], contrast agents [8, 19], or biomedical applications [20-23]. The goal of this paper is to review a major implementation of PAT, photoacoustic microscopy (PAM). PAM has achieved spatial resolution ranging from sub-micrometer to sub-millimeter, at maximum imaging depths ranging from a few hundred micrometers to a few millimeters [3, 6]. Distinct from reconstruction-based PA computed tomography (PACT) [24-31], the other major implementation of PAT, PAM employs raster-scanning of optical and acoustic foci and forms images directly from acquired depth-resolved signals [3]. PAM maximizes its detection sensitivity by confocally aligning its optical illumination and acoustic detection. While the axial resolution of PAM is primarily determined by the imaging depth and the frequency response of the ultrasonic transducer, its lateral resolution is determined by the combined point spread function of the dual foci. PAM can be further classified into optical-resolution PAM (OR-PAM), where the optical focusing is much tighter than acoustic focusing [32], and acoustic-resolution PAM (AR-PAM), where the acoustic focusing is tighter [33, 34]. In addition, photoacoustic endoscopy (PAE) is considered as a variant of PAM for internal organ imaging, which is typically rotational scanning based. In PAM, while the depth-resolved acoustic waves render 1D PA images (A-scan), two-dimensional raster scanning generates 3D PA images (C-scan).

In this dissertation, we will focus on the system construction and applications of OR-PAM. First, we will introduce the system characteristics of OR-PAM, including the spatial resolution, maximum imaging depth and imaging speed. Next, we will describe the different methods for oxygen saturation, flow speed and metabolic rate of oxygen measurements in multi-contrast OR-PAM. Then, we will highlight the improvements of OR-PAM in its imaging depth and imaging speed. In the end, we envision future developments.

2. Optical-resolution photoacoustic microscopy

The scalability of PAM originates from its optical and acoustic focusing [3]. Within the optical diffusion limit, OR-PAM has a great advantage over AR-PAM in spatial resolution because the optical beam can be easily focused to a much tighter spot than the acoustic detection, owing to shorter optical wavelengths.

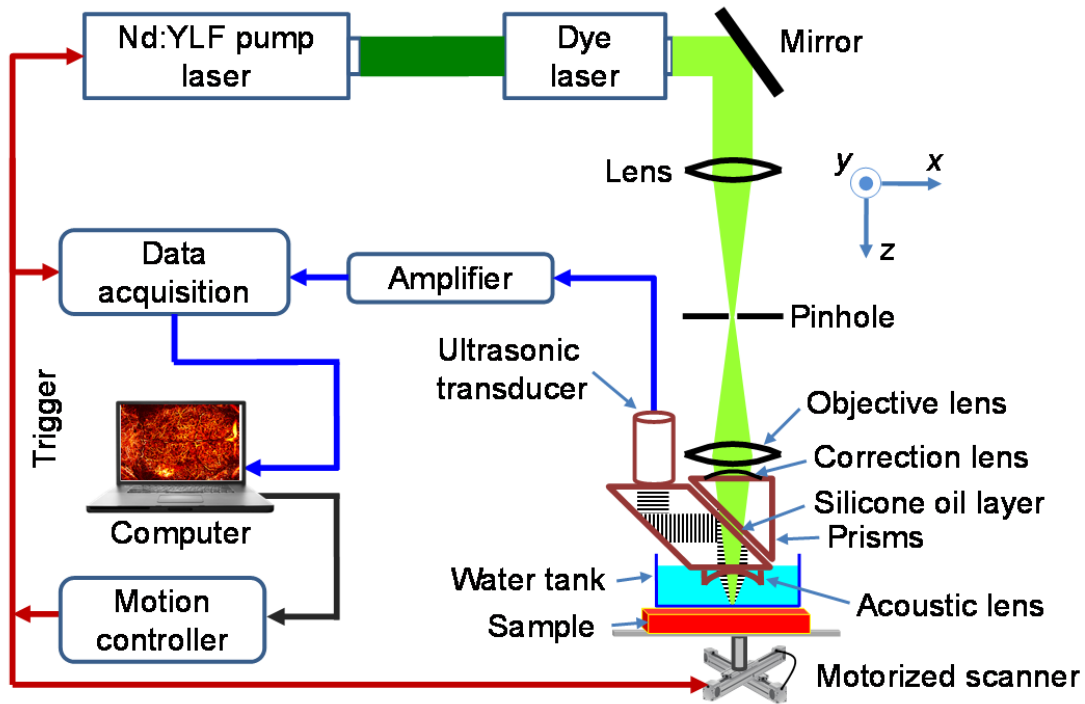


Figure 1. Schematic of second-generation of optical-resolution photoacoustic microscopy

Figure 1 shows a newly developed second-generation OR-PAM, which has shown a robust capability to non-invasively image microvasculature using endogenous contrast with high spatial resolution (lateral: $\sim 5 \mu\text{m}$; axial: $\sim 15 \mu\text{m}$) [32]. A tunable dye laser (CBR-D, Sirah) pumped by a Nd:YLF laser (INNOSAB, Edgewave, 523 nm) serves as the light source. The laser pulse is reshaped by a 25- μm -diameter pinhole and focused onto the surface of the mouse ear by a microscope objective lens (Olympus 4 \times , NA=0.1) with a pulse energy of $\sim 100 \text{ nJ}$. Ultrasonic detection is achieved through a spherically focused ultrasonic transducer (V2012-BC, Panametrics-NDT), which is placed confocally with the objective. The detected PA signal is then amplified, digitized, and saved. A volumetric image is generated by recording the time-resolved PA signal (A-line) at each horizontal location of the two-dimensional raster scan. The motion controller provides the trigger signals for laser firing, data acquisition, and motor scanning.

Since the acoustic focal diameter ($\sim 45 \mu\text{m}$) is more than ten times as wide as the optical focal spot, the detection sensitivity within the optical focus is approximately uniform. Therefore, the lateral resolution of OR-PAM $R_{L,OR}$ is given by the diffraction-limited spot size of the optical focus [3, 35],

$$R_{L,OR} = 0.51 \frac{\lambda_o}{NA_o} \quad (1)$$

where λ_o is the optical wavelength and NA_o is the numerical aperture of the optical objective. The constant 0.51 reflects the full width at half maximum (FWHM) of the optical focal spot in light intensity. For a wavelength of 570 nm and an NA_o of 0.13, the lateral resolution of G2-OR-PAM was experimentally determined to be $2.56 \mu\text{m}$, which agrees to Eq. (1) [36]. This resolution is sufficient to resolve the cortical capillaries (diameter: $5\text{-}10 \mu\text{m}$) of a nude mouse with the scalp removed but skull intact. From Eq. (1), the lateral resolution of OR-PAM can be scaled down by either increasing the objective NA_o or using a shorter excitation wavelength, with the maximum imaging depth scaled accordingly.

It should be pointed out that the lateral resolution of OR-PAM is the finest at the depth corresponding to the focus of the optical objective for OR-PAM. At the two ends of the focal zone, the lateral resolution degrades by $\sqrt{2}$ due to diffraction. The focal zone for OR-PAM can be computed as $Z_{OR} = 1.8\lambda_o / NA_o^2$. At the ends of twice the focal zone, the lateral resolution degrades by a factor of 2.

The axial resolution of OR-PAM can be estimated by the formula, $R_{A,OR/AR} = 0.88v_A / \Delta f_A$, which is based on the assumption that the PA response to a point target follows a Gaussian frequency profile [3, 37]. Δf_A is the PA signal bandwidth, which can be approximated as the detection

bandwidth of the ultrasonic transducer and is often proportional to its central frequency f_A . However, this is based on the assumption that the PA signal bandwidth is much wider than the detection bandwidth. As mentioned above, high-frequency components of acoustic waves are attenuated faster than low frequency ones, and thus, PA signal bandwidth decreases with imaging depth, resulting in worse axial resolution at greater depths. Using ultrasonic transducers with a central frequency of 50 MHz and a one-way -6 dB bandwidth of 100%, G2-OR-PAM in Figure 1 has achieved the same axial resolution of 15 μm .

The maximum imaging depth of OR-PAM is limited to ~ 1 mm in tissue due to optical scattering [36]. The optical attenuation by tissue includes both absorption and scattering [2]. Compared with absorption, scattering has a relatively weak dependence on wavelength. In general, an excitation wavelength within the tissue optical window around 700 nm helps achieve a deeper penetration because of the relatively low absorption of both hemoglobin and water, two major absorbers in tissue [2, 38]. As a gold standard, OR-PAM can achieve a depth-to-resolution ratio (DRR) of ~ 80 . The DRR is defined as the ratio of the maximum imaging depth to the axial resolution, representing the number of resolution pixels in the depth dimension.

As a high-resolution imaging modality, OR-PAM requires 2D raster scanning for 3D imaging. Compared with confocal microscopy and two-photon microscopy, PAM does not need depth scanning. Nonetheless, fast imaging speed is desirable to capture dynamics and eliminate motion artifacts caused by breathing and heart beating. The traditional OR-PAM systems with ball-screw mechanical scanning have a typical cross-sectional (B-scan) scanning rate of 1 Hz [33-35]. This translates into an image acquisition time of 7 min for OR-PAM. Finer resolution PAM

systems, such as SW-PAM, need more pixels per unit area, resulting in an even longer data acquisition time [35].

3. Multi-contrast photoacoustic microscopy

Originating from optical absorption, photoacoustic signals can be used to derive a number of physical, chemical and functional parameters of the absorber and its microenvironment. Since a single parameter may not be able to fully reflect the true physiological and pathological conditions, multi-parameter PAM can provide a more comprehensive understanding, thus benefiting the diagnosis, staging and treatment of diseases.

3. 1. Photoacoustic microscopy of capillaries enhanced by Evans blue

Total concentration of hemoglobin (C_{Hb}) is the most commonly used blood perfusion index. At the isosbestic wavelengths of hemoglobin (e.g., 498 nm, 568 nm and 794 nm), the PA signal amplitude reflects the C_{Hb} distribution in relative values, regardless of the oxygenation level of hemoglobin [39].

However, RBC flow in capillaries is discontinuous and changes greatly over time [40-42]. Because RBCs are the only noticeable optical absorbers in capillaries, it is highly likely that no absorber is present in a particular voxel during the laser pulse, which results in discontinuous capillaries in a RBC-based PA image. In order to acquire a complete capillary image and gain information about the capillary's functional state[43], the use of an exogenic contrast agent is compelling.

We use Evans Blue (EB) dye for this purpose. EB has strong absorption in visible and near-infrared light, with a peak at 620 nm. EB is non-toxic and is used in measurement of blood

volume [44], lymph node location [45], microvascular permeability [46, 47], blood-retinal barrier breakdown [48], capillary perfusion [42] and blood plasma flow [40] among other applications. In the blood stream, EB mainly binds to serum albumin in a reversible manner, so it is uniformly distributed in the plasma, maximizing the chance to get a complete capillary network image. Under normal conditions, the EB-albumin (EBA) complex is confined to blood vessels, while the free dye more readily diffuses out into extravascular tissue. The diffused dye is bound to the surrounding tissue proteins, and finally cleared out by either metabolism or excretion [49-52].

3.1.1. Methods

Animal preparation

The ears of adult, 6- to 8-week-old nude mice (Hsd: Athymic Nude-FoxI^{NU}, Harlan Co.; body weight: ~20 g) were used for all *in vivo* experiments here because their small thickness allowed us to verify some of the PA results by using a standard bright field optical microscope. The nude mouse ear model has a well-developed vasculature and has been widely used to study tumor angiogenesis and other microvascular diseases [53]. Before data acquisition, the animal was anaesthetized by an intraperitoneal injection of 85% ketamine and 15% xylazine (100 μ l/g body weight). During data acquisition, the animal was placed on a warming pan (37° C), and its head was held steady with a dental/hard palate fixture. The animal was kept still by using a breathing anesthesia system (E-Z Anesthesia, Euthanex). After experiment, the animal recovered naturally and was returned to its cage. All experimental animal procedures were carried out in conformity with the laboratory animal protocol approved by the Animal Studies Committee of School of Medicine at Washington University in St. Louis.

Mode of injection of EB

A 6% or 3% EB w/v solution (Sigma, St. Louis, MO) was prepared by dilution of the dye in phosphate-buffered saline (PBS, pH 7.5). Before injection, the solution was filtered through a 5- μm filter. An intravenous injection of EB was made to either of the dorsal veins of the tail. The injection lasted for about 10–20 seconds.

3.1.2. Results

Spatially continuous capillary imaging using EB as a contrast agent

Two irradiation wavelengths 570 nm and 610 nm were chosen for RBC imaging and EB imaging, respectively. An area of 2 mm \times 2 mm was chosen as the field of interest (FOI) near the margin of the nude mouse ear, where the capillary density was higher. Before the dye injection, control images were acquired with a scanning step size of 2.5 μm at 570 nm and 610 nm. The total scanning time for a complete volumetric data set was \sim 30 min for each wavelength. In order to get sufficient imaging contrast and sensitivity of the capillaries, a relatively high concentration of EB in the blood plasma should be reached. Here 0.2 mL of 6% EB solution was injected in a nude mouse (body weight: \sim 20 g). The total blood volume of the mouse was about 1.2 mL [54]. Thus the concentration of EB in the blood stream was \sim 1%, corresponding to an absorption coefficient of \sim 1000 cm^{-1} at 610 nm [55], which is \sim 20 times higher than that of blood (\sim 50 cm^{-1}). Two PA images at 610 nm were acquired, one immediately after the dye injection and the other 30 min later. Transmission optical microscopic images at 4 \times magnification were acquired before and after injection.

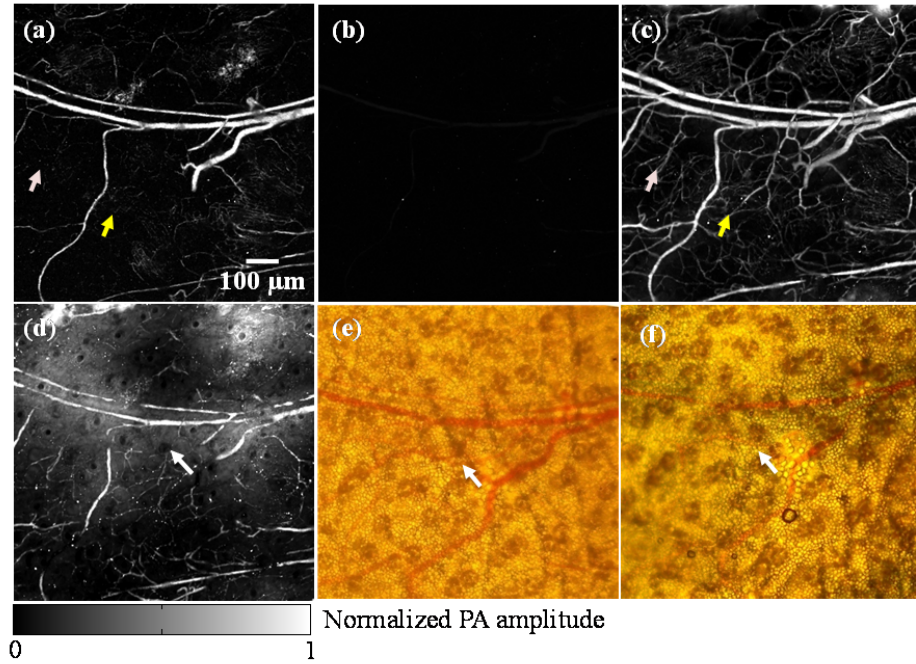


Figure 2. EB enhanced photoacoustic imaging of mouse ear microvessels. (a, b) PA microvascular image before dye injection acquired at 570 nm (a) and at 610 nm (b). Arrows in (a) point to the fragmentary capillaries. (c) PA image acquired at 610 nm right after EB (6%, 0.2 mL) injection via tail vein. Arrows in (c) point to the continuous capillaries. (d) PA image acquired at 610 nm acquired 30 min after injection. (e, f) Transmission microscopic images of the same area before (e) and after (f) injection. Arrows in (d), (e) and (f) point to sebaceous glands. All the photoacoustic images were scaled to the same level of PA signal.

Before dye injection, a PA image was acquired at 570 nm. Hemoglobin has strong absorption at this wavelength, which provided high imaging contrast and a high signal to noise ratio (>40 dB). Veins and arteries larger than $10\ \mu\text{m}$ in diameter contained a higher area density of RBCs and appeared uniformly bright. However, smaller capillaries, containing a single of RBCs, looked discontinuous and fragmentary. As a control, another image was acquired at 610 nm. The signal was very weak due to the low hemoglobin absorption at 610 nm, which was only one-twentieth of that at 570 nm. Right after the dye injection, the microvascular network appeared continuous as shown in Fig. 2c. Dense capillaries could be observed, as indicated by arrows. All the capillaries appear ‘broken’ in Fig. 2a became smooth and continuous. Moreover, the capillary branching points that were invisible in Fig. 2a could be clearly distinguished. The blood vessels

in Fig. 2c appear somewhat thicker than those in Fig. 2a, which was possibly because the plasma volume was larger than the RBC volume. The discernable blood vessel volume in the plasma-based image appeared to be more than 50% greater than that disclosed in the RBC-based image. The image in Fig. 2d was acquired at 610 nm 30 min after dye injection. It shows that a considerable amount of EB had diffused out of the blood vessels into the surrounding tissue but did not diffuse into the sebaceous glands, which appear as brown patches in the transmission microscopic images.

Dynamics of EB diffusion out of the blood stream

EB is removed from the vascular system principally by diffusing into extravascular tissue. At high dye concentrations, in the first few hours, it is mainly the free EB rather than the EB-albumin complex that diffuses out. The fixation of the free EB molecules by tissue proteins causes more dye to leave the blood to maintain chemical equilibrium, until the tissue proteins become saturated [49-52, 56]. To better understand the diffusion dynamics, we monitored the dye diffusion over time and quantified the diffused dye volume in the tissue. Here, a smaller area of 1 mm \times 1 mm was imaged near the margin of the nude mouse ear, so more data sets could be acquired over time due to the shorter scanning time of \sim 10 min. Control images at 570 nm and 610 nm were acquired before dye injection. After 0.1 mL of 6% EB solution was injected, the dye molar concentration in the plasma was \sim 0.52 mM, which was a high concentration compared with the combination capability of albumin [52]. Right after injection, serial images at 610 nm were acquired every 20 min until the dye diffusion was observed to have reached saturation.

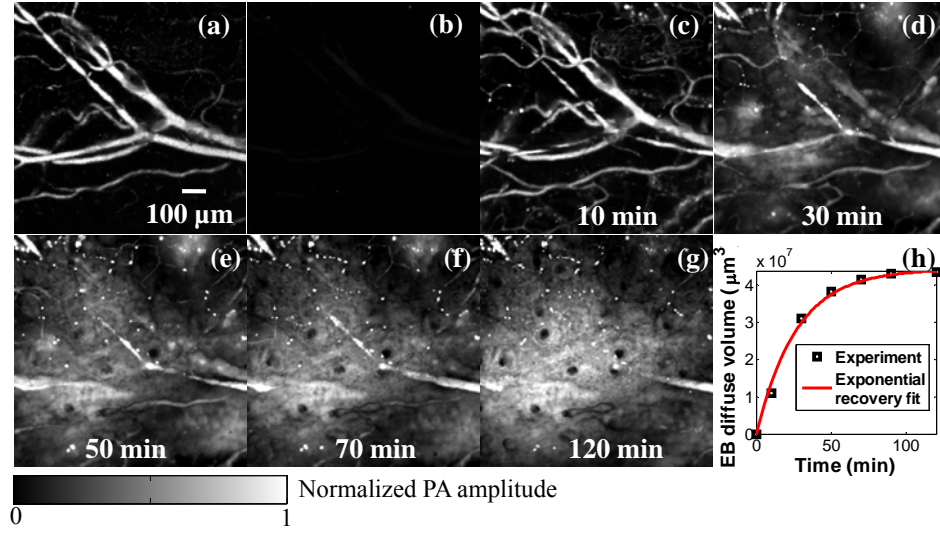


Figure 3. Dynamics of EB diffusion out of the blood stream into surrounding tissue. (a, b) PA images acquired before EB injection at 570 nm (a) and at 610 nm (b). (c)-(g) PA images acquired at 610 nm after EB (6%, 0.1 mL) injection at different times. (h) Partial volume of EB diffused into surrounding tissue. An exponential recovery model was used to fit the experiment data. All the photoacoustic images were scaled to the same level.

As before, control images at 570 nm and 610 nm were acquired before dye injection (Fig. 3a and 3b). The whole microvascular network within the field of view showed up with denser and more continuous capillaries right after the 0.1 mL of 6% EB solution was injected (Fig. 3c). Sequential images were acquired at different time points from 30 min to 120 min (Figs. 3d-g). The partial volume of the free EB molecule diffused into extravascular tissue increased gradually and reached a plateau after ~2 hours. If the dye left the blood vessels in a passive diffusion pattern, the extravascular dye volume could be fitted by an exponential recovery model [57].

$$Q_T(t) = Q_e[1 - \exp(-kt)] \quad (2)$$

where $Q_T(t)$, Q_e are the dye volumes at time t and equilibrium, respectively, and k is the dye diffusion rate. The fit result shows that EB indeed diffused in a passive pattern (Fig. 3h). However, EB did not diffuse into the sebaceous glands, so more and more ‘dark cavities’ were

formed as the diffusion went on. Blood vessels were embedded in the diffused dye and capillaries became nearly invisible.

Dynamics of the EBA clearance

At low dye concentrations, EB exists almost exclusively in the form of EBA [52]. EB permeates wherever albumin is present. Therefore, the clearance dynamics of the EBA may be used to estimate the albumin metabolic rate in tissue [52].

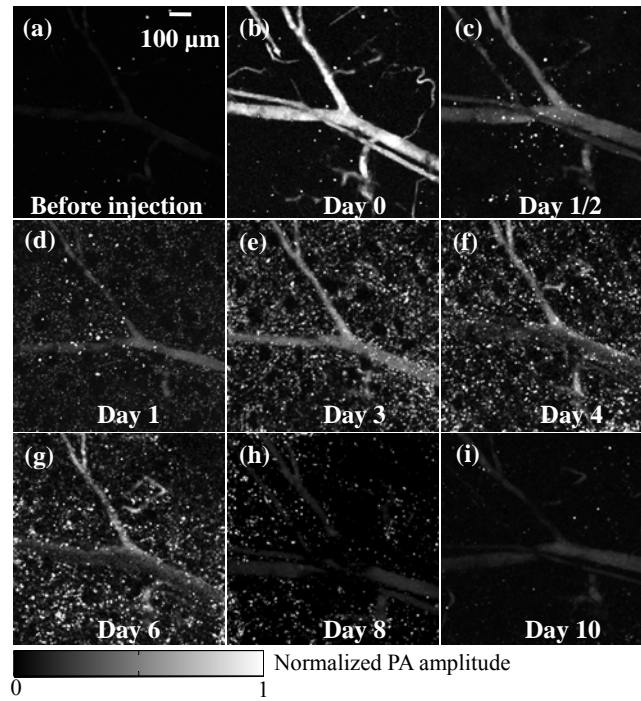


Figure 4. Clearance dynamics of EBA. Before EB injection, (a) was acquired at 610 nm. On $\frac{1}{2}$ –10 days following EB (3%, 0.05 mL) injection, images (b)–(i) were acquired at 610 nm. All the photoacoustic images were scaled to the same level.

To better understand the clearance dynamics, in our work the EBA volume in the tissue was monitored by PA imaging. An imaging area of 1 mm \times 1mm was chosen on the nude mouse ear, and control images at 570 nm and 610 nm were acquired before dye injection. Then 0.05 mL of 3%

EB solution was injected via the tail vein. Serial images were acquired at 610 nm every one or two days, until EBA had nearly completely cleared out.

Before dye injection, Fig. 4a was acquired at 610 nm as a control image. Fig. 4b–i were acquired on different days after dye injection. The EBA volume out of the blood vessels was calculated. Quantified clearance was shown in Fig. 5. The EBA volume in the extravascular tissue reached maximum on Day 3 and then decreased to the base line by Day 10.

A two-compartment model was used to fit the EBA volume in the extravascular tissue.

$$\begin{aligned}\frac{dQ_V}{dt} &= -k_1 Q_V \\ \frac{dQ_T}{dt} &= k_1 Q_V - k_2 Q_T\end{aligned}\tag{3}$$

where Q_V , Q_T are the EBA volumes in the blood stream and extravascular tissue, respectively. k_1 is the diffusion rate of EBA from the blood stream into the extravascular tissue, and k_2 is the clearance rate of EBA in the tissue. The results were consistent with the standard histological studies of long term EBA decline [56, 58].

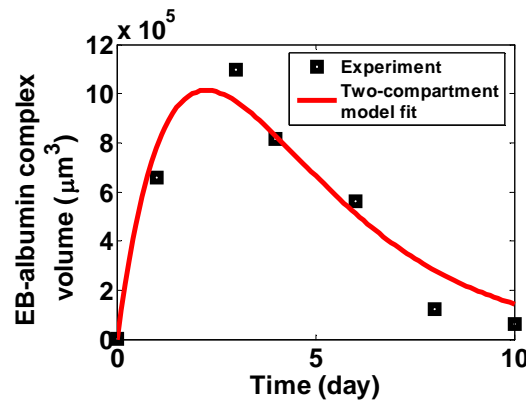


Figure 5. Quantitative analysis of EBA clearance. After EB (3%, 0.05 mL) injection, the diffused EBA volume in the surrounding tissue reached maximum on Day 3, and decayed to the baseline by Day 10. A two-compartment model was used to fit the experiment data.

3.1.3. Conclusions and discussion

In this work, we demonstrate the feasibility of using Evans Blue dye as a contrast agent to enhance *in vivo* photoacoustic microvascular imaging. Complete and continuous microvascular networks especially capillaries were imaged with the contrast of EB. And as to our knowledge, it is the first time that PA imaging has been used to study the dynamics of EB diffusion and EBA clearance.

The photobleaching of EB may be crucial for quantitative study. In a previous study [55] for a pulsed Nd:YAG laser (532 nm, 50 Hz, 14 ns pulse) and static 0.3% EB solution, photobleaching started after 1 min irradiation with an energy deposition of 20 mJ/pulse cm². In our study, the energy pulse deposition was about 100 mJ/pulse cm². However, the irradiation time was only 7 ns at each imaging position, which is much shorter than the reported photobleaching exposure time. Therefore, the influence of photobleaching on the quantitative study can be ignored, and the possibility that the apparent clearance of the dye was caused by photobleaching can be excluded.

At high EB concentrations, it is mainly the free dye that passively diffuses out of the blood vessels over tens of minutes. At low EB concentrations, as in most biological applications [40, 45, 47, 58, 59], it is mainly the EBA that diffuses out of the blood vessels, and thus it is usually used as an indicator of the vessel leakage level. Our study was implemented under baseline conditions, where the blood vessel was leakage-resistant for albumin, so relatively high EB concentrations were used here to study the dynamics. However, a high contrast PA image does not depend on whether free EB dye or EBA caused dye diffusion into extravascular tissue. The key point here is that the potential application of PA imaging combined with EB for physiological and pathological studies has been well demonstrated. Moreover, to test the imaging

sensitivity, a commonly used EB injection dose (30 mg/kg body weight) was used. The diffused EBA can be clearly observed due to the high absorption contrast between the dye-protein complex and background tissue hence the imaging sensitivity is sufficient for the biological applications.

It is interesting that EB and EBA did not diffuse into the sebaceous glands, where ‘dark cavities’ were formed in the PA images, possibly caused by the denser structure or the biochemical properties of the sebaceous glands. The physiological characteristics of sebaceous glands have been thoroughly studied [60]. PA imaging facilitated by EB can provide three-dimensional structural and functional information of sebaceous glands, which are very important growth indexes during carcinoma development.

3.2. Photoacoustic microscopy in transverse blood flow imaging

Combining the spatial resolution of ultrasound imaging with the contrast of optical absorption in deep biological tissues, photoacoustic imaging has been widely used in high-sensitivity structural and functional imaging with micrometer-scale spatial resolution [26, 32, 33, 61]. It has also shown the potential for measuring blood flow [62-64]. Previously, photoacoustic Doppler (PAD) shift was observed from flowing particles illuminated by an intensity-modulated continuous-wave (CW) laser beam [62, 63]. This physical phenomenon provides a basis for photoacoustic Doppler flowmetry in optically scattering media [62]. However, the sensitivity of this method depends mainly on the FFT time window, which limited the three-dimensional imaging speed [65]. Furthermore, because a CW excitation source was used without frequency chirping, depth could not be resolved. Like the other flowmetries based on the Doppler frequency shift, PAD flowmetry was sensitive to the Doppler flow angle. In PA imaging of microvascular networks, the transverse component of the flow is sometimes dominant. When the Doppler angle

approaches 90°, the PAD frequency shift almost vanishes. Previous works in the fields of optical coherence tomography and ultrasound imaging have demonstrated the feasibility of using the bandwidth broadening to provide quantitative information on transverse flow [66-68]. However, in those works the flow direction could not be determined due to the symmetry of the optical objective or ultrasonic transducer. In the current work, we propose a method to measure both the transverse flow speed based on bandwidth broadening and the flow direction based on bidirectional scanning.

3.2.1. Methods

Sources of broadening include geometry, transit time, Brownian motion, velocity gradient and turbulence [62, 66]. The contribution of Brownian motion to the overall broadening has been shown to be small and consequently neglected [69]. The contributions of the velocity gradient and turbulence can be minimized if the spatial resolution is high enough. The contributions of transit time and geometry are equivalent within the focal region [70, 71]. and can be derived either from diffraction theory or beam-to-flow ray theory, as shown in Fig. 6 [67].

The bandwidth, B_d , is given by

$$B_d = 2 f_0 \frac{v}{c} \sin \theta \sin \varphi \approx f_0 \frac{v}{c} \frac{W}{F} \sin \theta, \quad (4)$$

where v is the flow velocity; c is the speed of sound; θ is the Doppler angle; φ is the aperture angle of the acoustic lens; and f_0 , W , and F are the center frequency, the diameter, and the focus length of the ultrasonic transducer, respectively. The bandwidth is proportional to the transverse flow and is maximized when the Doppler angle is 90°.

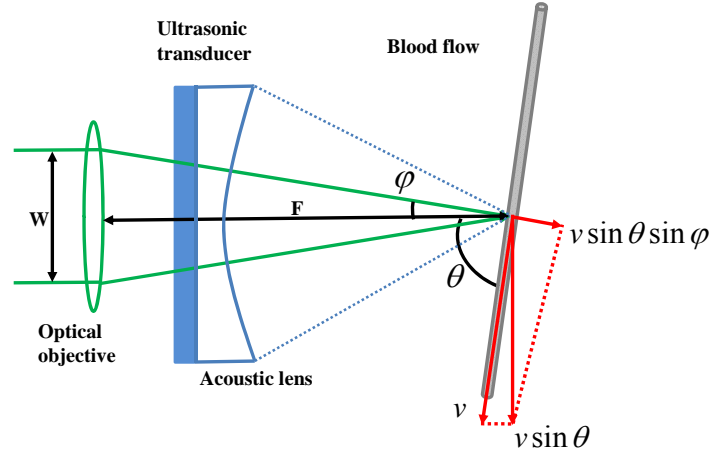


Figure 6. Probe-beam geometry for the transverse flow measurement.

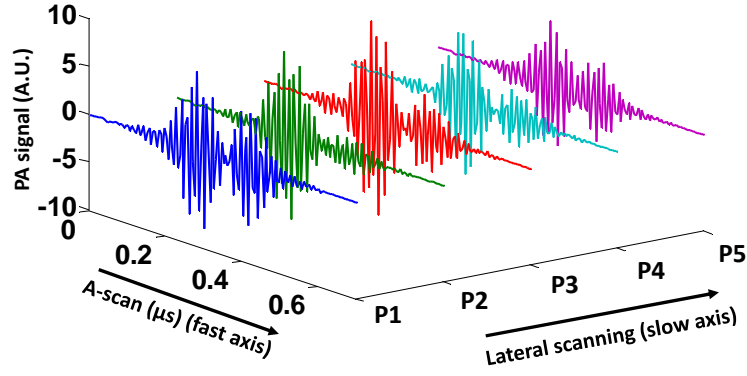


Figure 7. Sequential A-scans used to calculate the bandwidth broadening.

Because the resultant photoacoustic wave induced by pulse-laser excitation was wide-band, we used the standard deviation of the sequential A-line scans to estimate the bandwidth broadening (Fig. 7) [72, 73]. The digitized PA signal $p(t)$ was first passed through a digital bandpass filter to increase the signal-to-noise ratio. The complex function $\tilde{p}(t)$ was determined by the Hilbert transformation from $p(t)$. The bandwidth broadening is given by

$$B_d = \frac{k}{T} \left(1 - \frac{\left| \sum_{j=1}^n \tilde{p}_j \tilde{p}_{j+1}^* \right|}{\sum_{j=1}^n \tilde{p}_j \tilde{p}_j^*} \right)^{1/2}, \quad (5)$$

where T is the time interval between sequential A-scans, n is the number of sequential scans used to compute the standard deviation, and k is an experimentally determined constant factor associated with the imaging system [72, 73]. The structural information was provided by the envelope amplitude of each A-scan, and the flow information was provided by the bandwidth broadening computed from sequential A-scans.

Here, it is necessary to point out that OR-PAM, where the RBC number within the tight optical focus is limited, differs from the acoustic-resolution PAM (AR-PAM). In AR-PAM where the acoustic focus provides the lateral resolution, the high RBC density may increase the difficulty to detect the signal fluctuation caused by RBC flow. This can be potentially solved using low concentration contrast agents, such as nanoparticles. The imaging depth then can be extended into the diffuse regime. The proposed method should work in both cases, and the difference is accounted for by k in Eq. (5).

In the current imaging system, the sample was translated by the scanning motor. Hence, the bandwidth broadening was actually determined by the combination of the flow velocity and the motor scanning velocity (Fig. 8). Therefore, a bidirectional scanning was used to determine the flow direction. The motor first scanned with velocity \vec{v}_{m+} , and then switched to velocity \vec{v}_{m-} . \vec{v}_{m-} has the same value as \vec{v}_{m+} but in the opposite direction. The measured flow speeds under the two scanning directions are given by the combination speeds of the flow and the motor as follows:

$$\begin{aligned}
v_{f_m+} &= (v_f^2 + v_m^2 + 2v_f v_m \cos \phi)^{1/2} \\
v_{f_m-} &= (v_f^2 + v_m^2 - 2v_f v_m \cos \phi)^{1/2},
\end{aligned} \tag{6}$$

where v_{f_m+} and v_{f_m-} are the measured speeds with motor-scanning velocities \vec{v}_{m+} and \vec{v}_{m-} , respectively; v_m is the motor scanning speed; ϕ is the angle between \vec{v}_{m+} and the flow velocity \vec{v}_f , and $|\cos \phi|$ can be provided by structural PA imaging. Solving for the flow speed gives

$$v_f = \begin{cases} \left| \frac{v_{f_m+}^2 - v_{f_m-}^2}{4v_m \cos \phi} \right| & \text{for } \phi \neq 90^\circ \\ \frac{\sqrt{2}}{2} (v_{f_m+}^2 + v_{f_m-}^2 - 2v_m^2)^{1/2} & \text{for } \phi = 90^\circ \end{cases} \tag{7}$$

If $v_{f_m+} > v_{f_m-}$, we get $\phi < 90^\circ$ and vice versa. Therefore, the flow direction can be determined.

In case that $v_{f_m+} = v_{f_m-}$, which means that the flow is perpendicular to the motor-scanning direction, the flow direction can be determined at other positions, because the flow path is usually nonlinear.

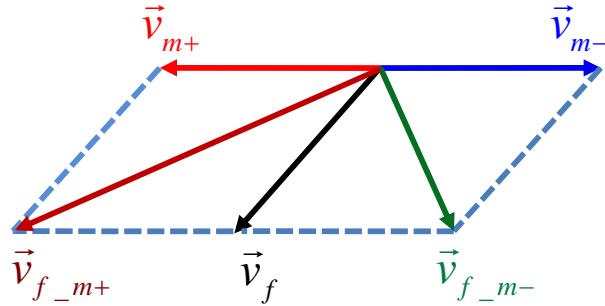


Figure 8. Bidirectional scanning to determine the flow direction.

3.2.2. Results

Phantom study

A straight capillary tube (inner diameter: 260 μm) and a 0.1% solution of red-dyed particles (diameter: 6 μm) were used to study the dependence of the bandwidth on the flow velocity. The flow with speeds for 0 to 2.5 mm/s was controlled by a 1 mL syringe driven by a syringe pump and illuminated at 570 nm. Although the scan angle can be generalized, in this instance, the bidirectional scanning was along the tube ($\phi = 0^\circ$). The flow direction was the same as \vec{v}_{m+} .

In this experiment, we extracted the data from the center of the capillary (Fig. 9a, $\theta = 90^\circ$). When the flow velocity was zero, the bandwidth broadening was caused only by the motor scanning, no matter the scanning direction. When the scanning was in the same direction as the flow (\vec{v}_{m+} , square), the bandwidth increased as the flow speed increased. When the scanning was opposite to the flow (\vec{v}_{m-} , triangle), the bandwidth first decreased as the flow speed increased. However, when the flow speed exceeded the scanning speed, the bandwidth began to increase. The turning point indicated the motor-scanning speed v_m . After subtraction of the contribution of the motor scanning, the bandwidth profiles at the speeds of 2.3 mm/s (circle) and 1.6 mm/s (square) are shown in Fig. 9b. A parabolic flow model was used to fit the experimental results (solid curves). Data points on the bottom half of the capillary tube (the right side of the plot) were fewer than on the upper half, because light penetration was limited.

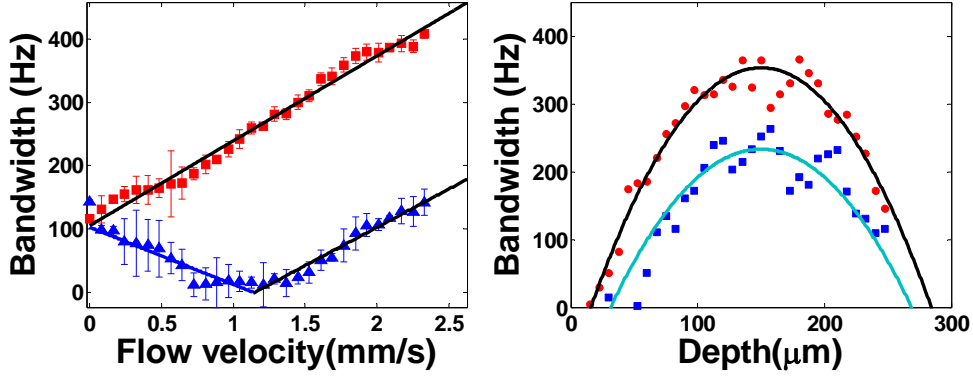


Figure 9. Photoacoustic flow measurement on microsphere phantom. (a) Bandwidth as a function of flow velocity with a bidirectional motor scanning speed of 1.1 mm/s and Doppler angle of 90° . The motor scanning direction was either the same as the flow direction (\vec{v}_{m+} , square) or opposite to the flow direction (\vec{v}_{m-} , triangle). Solid curves, theoretical predictions fitted with Eq. (2). Error bar, standard error. (b) Flow profiles at flow velocities of 2.3 mm/s (circle) and 1.6 mm/s (square), after subtraction of the contribution of the motor scanning. Solid curves, fitted parabolic flow profiles.

A tube laid in a zigzag pattern was used to get the structural and flow information simultaneously.

The flow speed was set to be 1.3 mm/s and the flow direction varied from segment to segment.

Three adjacent segments of the tube, denoted as S_1 , S_2 and S_3 in Fig. 10a, were imaged. The

bidirectional scanning was along the longitudinal axis of these segments. The flow directions in

S_1 and S_3 were the same as \vec{v}_{m+} while the flow direction in S_2 was the same as \vec{v}_{m-} .

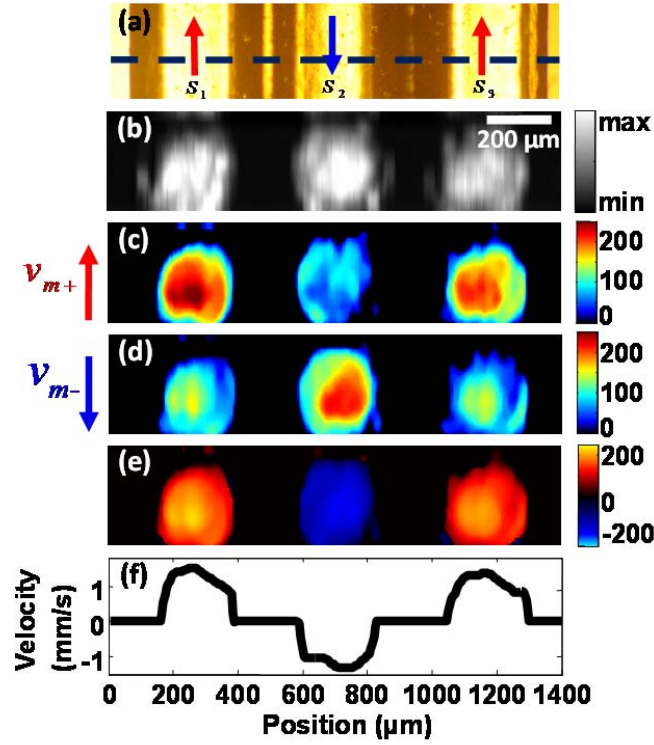


Figure 10. Photoacoustic flow imaging of microsphere phantom. (a) A transmission optical microscopy image of three adjacent segments of a tube laid in a zigzag pattern. The flow directions in S_1 and S_3 were the same as \vec{v}_{m+} , and the flow direction in S_2 was the same as \vec{v}_{m-} . (b) A cross section of the structural image. The approximate position of the cross section is indicated by the dashed line in (a). The scale bar for (b)-(e) is shown in (b). (c) The bandwidth image when the motor scanned in \vec{v}_{m+} . (d) The bandwidth image when the motor scanned in \vec{v}_{m-} . (e) The bandwidth image after subtraction of the contribution of the motor scanning. The positive flow (with the same direction as \vec{v}_{m+}) is shown in red and the negative flow (with the same direction as \vec{v}_{m-}) is shown in blue. (f) The speed profile indicated by the dashed line in (e).

One cross section of the PA structural image is shown in Fig. 10b, and the approximate position of the cross section is indicated by the dashed line in Fig. 10a. The measured bandwidths when the motor scanned in \vec{v}_{m+} and \vec{v}_{m-} were quantified, as shown in Figs. 10c and 10d, respectively. Because the flow directions in S_1 and S_3 were the same as \vec{v}_{m+} , and the flow direction in S_2 was opposite to \vec{v}_{m+} , the measured bandwidth in S_1 and S_3 was greater than that in S_2 when the

motor scanned in \vec{v}_{m+} (Fig. 10c). For the same reason, the measured bandwidth in S_1 and S_3 was smaller than that in S_2 when the motor scanned in \vec{v}_{m-} (Fig. 10d). After subtraction of the contribution of the motor scanning, the bandwidth in all three segments became similar (Fig. 10e), which means that the flow speed within the tube was consistent. The positive flow (with the same direction as \vec{v}_{m+}) is shown in red and the negative flow (with the same direction as \vec{v}_{m-}) is shown in blue. The negative bandwidth is only used to indicate the flow direction. The calculated flow profile indicated by the dashed line in Fig. 10e is shown in Fig. 10f. At the boundary of the tube, the particle density and the flow speed were relatively low, which resulted in instability in the calculation. The signal from the tube wall also contributed to the calculation error.

Animal study

In vivo experiment was performed on the ear of a 6-week-old mouse (Hsd:ND4, Swiss Webster; Harlan, Indianapolis, IN). A volumetric dataset was acquired at 560 nm and 570 nm under bidirectional scanning on a 2 mm \times 1 mm area with a scanning speed of 0.75 mm/s and a step size of 0.625 μ m. The motor speed vibration ($< 5\%$ of the scanning speed) can be ignored in our study. Before data acquisition, the animal was anaesthetized by an intraperitoneal injection with a dose of 87 mg/kg ketamine and 13 mg/kg xylazine, and kept still by using a breathing anesthesia system (E-Z Anesthesia, Euthanex). All experimental animal procedures were carried out in conformity with the laboratory animal protocol approved by Washington University in St. Louis. The PA signal acquired at 570 nm maps the total hemoglobin concentration, which provides structural information of the vasculature (Fig. 11a). The dual-wavelength measurements were used to calculate sO₂ using a previously published method [74] (Fig. 11b). A trace of the averaged sO₂ values along the main vascular trunk is shown in Fig. 12a.

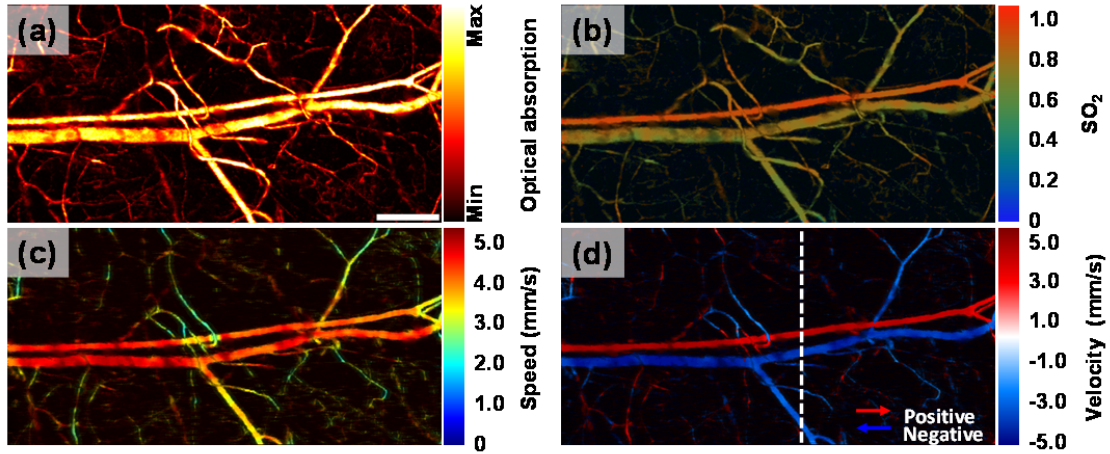


Figure 11. PA imaging of sO₂ and blood flow in a mouse ear. (a) MAP image of structure. Scale bar = 250 μ m. (b) MAP image of sO₂ by measurements at 560 nm and 570 nm. (c) MAP image of blood flow speed with magnitude only based on the Doppler broadening of bandwidth. (d) MAP image of blood flow velocity with directions. The positive and negative flow directions are shown in pseudocolors.

Bidirectional scanning measurements at 570 nm were used to calculate the Doppler broadening of bandwidth with eight sequential A-scans in one B-scan (Doppler angle: $\sim 90^\circ$), which provided the transverse blood flow images (Figs. 11c-d). Because the heart of a mouse beats at up to ~ 8 Hz and the frame rate for B-scans was ~ 1 Hz, the bidirectional scans most likely caught different phases of the systole and diastole. To mitigate the variation of the measured speed and better determine the flow direction, we averaged over 3-by-3 pixels. The positive and negative flows are shown in red and blue, respectively. A trace of the averaged speeds along the main vascular trunk is shown in Fig. 12b. Velocity profile indicated by the dashed line in Fig. 11d is shown in Fig. 12c. The flow speeds decrease from mother vessels to daughter vessels. The flow directions can also help to distinguish arterioles from venules. The imaged vessels that flow blood away from the heart are arterioles (marked in red in Fig. 11d), while the imaged vessels that flow blood back to the heart are venules (marked in blue in Fig. 11d). This classification is consistent with the categorization based on the sO₂ measurement as shown in Fig. 11b.

Saturation may exist here because the maximum measured speeds have reached the saturation point observed in the phantom study.

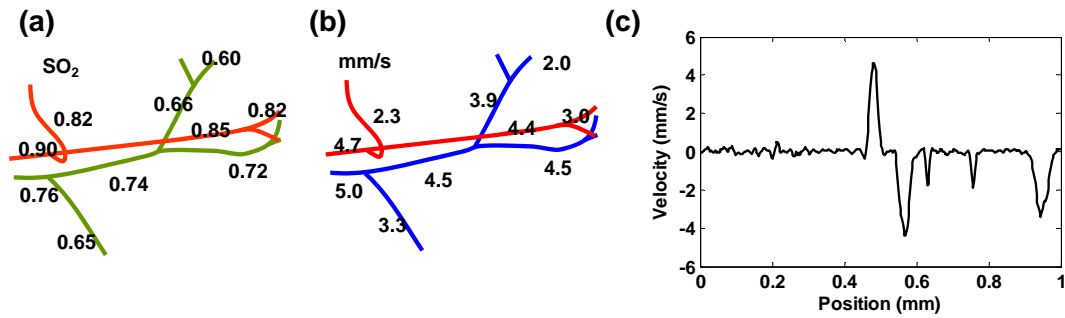


Figure 12. Quantitation of PA flow measurement in mouse ear. (a) Trace of SO_2 values, averaged along the main vascular trunk. (b) Trace of the blood flow speeds, averaged along the main vascular trunk. (c) Velocity profile of the blood flow indicated by the dashed line in Figure 11(d).

Another experiment was performed on a stage-16 chicken embryo. The chicken embryo has been widely used as a model to study the relationship between hemodynamics and circulatory diseases [75]. For our study, since the chicken embryo has a relatively slow blood flow speed and heart beating rate [75], the time course of the blood flow can be sufficiently sampled without speed saturation. A chicken embryo was first removed from a fertile white leghorn chicken egg (Sunrise Farms, Catskill, NY) after approximate 60 h of incubation and then cultured in phosphate buffered saline (PH: ~ 7.0). Infrared light was applied to the embryo during the experiment to maintain its activity (Temperature: $\sim 30^\circ C$).

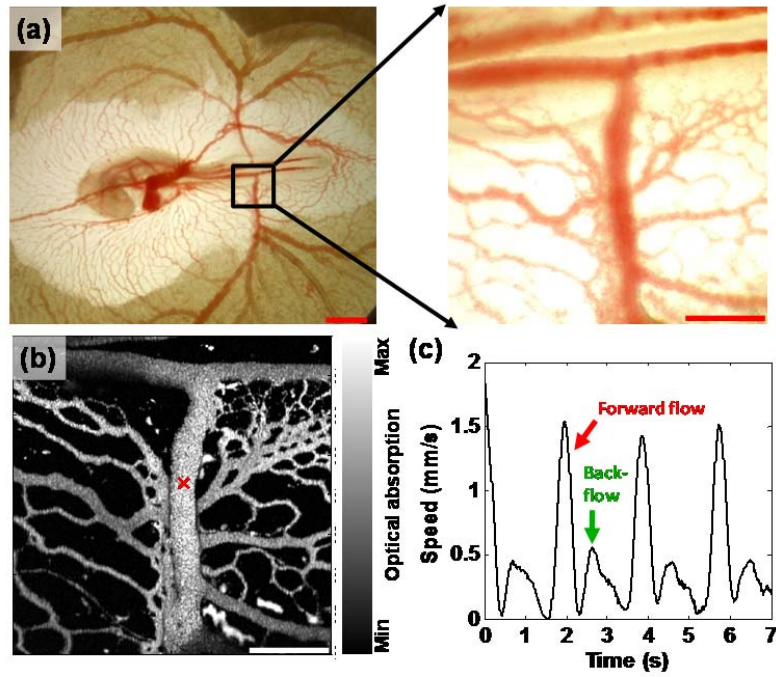


Figure 13. Blood flow measurement in a chicken embryo. (a) Left: a transmission optical microscopy image of a chicken embryo (stage 16). Scale bar = 2 mm. Right: a region of interest ($\sim 2 \text{ mm} \times 2 \text{ mm}$) imaged at a higher magnification ($\times 32$). Scale bar = 500 μm . (b) A PA image of the same area. Scale bar = 500 μm . (d) Time course of the blood flow speed at the position indicated by the cross in (b).

A transmission optical microscopy image of the entire embryo was acquired (Fig. 13a, left). An area of $\sim 2 \text{ mm} \times 2 \text{ mm}$ around the right lateral vitelline vein was imaged at a higher magnification (Fig. 13a, right), and a PA image of the same area was acquired at 570 nm (Fig. 13b). The time course of the flow speed at the center of a vessel, marked by a cross in Fig. 13b, was measured using eight sequential A-scans without motor scanning. The Doppler angle was $\sim 90^\circ$. The forward and backward flows are clearly observed (Fig. 13c). The measured flow speeds are consistent with those observed previously *in ovo* [75]. The opposite flow directions were confirmed using the optical microscopy. The spectral analysis of the time course indicates a heart beating rate of $\sim 0.5 \text{ Hz}$, which is consistent with the visual observation.

3.2.3. Conclusions and discussion

In theory, the maximum measurable speed is ~ 7.4 mm/s, which is limited by the 2 kHz maximum laser repetition rate and the light focus diameter in our system. It can be improved by increasing the laser repetition rate or enlarging the light focal spot. Both the minimum measurable speed and the speed sensitivity are around 0.1 mm/s, which are determined by the signal-to-noise ratio (SNR), which can be improved by averaging multiple measurements. With motor scanning, small vessels may not have sufficient SNR to keep the speed sensitivity. This problem can be solved by increasing the A-scan repetition rate or switching to M-mode measurement. The latter, however, will lose the flow direction information.

Bidirectional scanning can help to determine the flow direction along the scanning line. However, if \vec{v}_f is perpendicular to the scanning line, which gives $v_{f_m+} = v_{f_m-}$, the direction cannot be determined. One solution is to determine the flow direction at other positions of the same blood vessel. Another solution is to use four-directional scanning, including back and forth scanning along two orthogonal scanning lines. All the flow directions can be covered at the expense of imaging time.

3.3. Photoacoustic microscopy in total blood flow imaging

So far, photoacoustic flow measurements have focused on either the axial [76-79] or transverse [64, 80-83] component of the flow vector. However, to quantify the total flow vector, the Doppler angle (angle of the flow direction relative to the axis of the received acoustic wave) is needed. The Doppler angle can be estimated by tracing the vessel centerline either manually or automatically in a volumetric image. In practice, however, volumetric information is not always available, as in the case of *M*-mode imaging. In addition, despite the additional time required for

volumetric imaging, accurate estimation of the Doppler angle is challenging if the system's axial and lateral resolutions are too different. Here, using PAM, we propose a simple method for measuring total flow and the Doppler angle by combining the axial and transverse flow measurements. Briefly, the axial flow speed is estimated from the phase shift between consecutive Hilbert transformed pairs of A-lines [65]. The sign of the phase shift provides the axial flow direction. The transverse flow speed is quantified from the bandwidth broadening via the Fourier transformation of sequential A-lines [81]. The transverse flow direction can be measured by bi-directional scanning [81]. We first verified this method by flowing bovine blood in a plastic tube (inner diameter: 200 μm) at different total speeds (0–7.5 mm/s) and Doppler angles (30–330°). Then, in a mouse ear, we measured the total flow speed and Doppler angle *in vivo*.

3.3.1. Methods

Inspired by previous work in ultrasound imaging [84] and optical coherence tomography [65], we use the following formula to compute the axial component v_a pixelwise:

$$v_a = \frac{1}{2\pi} \cdot \frac{c}{T} \cdot \frac{\Delta\phi}{f_0}, \quad (8)$$

where c is the speed of sound in water (1500 m/s), T is the time interval between the two consecutive A-lines acquired in *M*-mode, $\Delta\phi$ is the phase shift in each pixel between two consecutive A-lines, and f_0 is the central frequency of an ultrasonic transducer. The phase shift $\Delta\phi$ is quantified via the Hilbert transformation. The sign of $\Delta\phi$ provides the axial flow direction, where positive $\Delta\phi$ means a flow towards the ultrasonic transducer and vice versa. The axial flow

velocity v_a is related to the total flow velocity v through $v \cdot \cos(\theta)$, where θ is the Doppler angle (Fig. 6).

It has also been demonstrated above that the transverse flow component v_t , which equals $v \cdot \sin(\theta)$, can be estimated based on Eq. (4) [66, 67, 81]. For a PAM system with confocal alignment but different optical and acoustic focal sizes, k in Eq. (4) mostly accounts for the discrepancy in the two foci. In the case of the optical-resolution PAM (OR-PAM) used in this study [32], shown in Fig. 1, where the optical focusing ($\sim 5 \mu\text{m}$) is much tighter than the acoustic focusing ($\sim 45 \mu\text{m}$), B_d mainly comes from the PA amplitude fluctuation caused by particles passing through the optical focal zone. Therefore, k is mostly determined by the beam geometry of the optical focusing and equals 0.02 here. Several other minor factors, such as Brownian motion, particle size and shape, and velocity distribution across the focal zone may contribute to B_d . Since all these bandwidth broadening mechanisms have a linear dependence on the mean transverse velocity [76], their contributions can also be incorporated into k . The transverse flow direction can be measured by bi-directional scanning, as long as the transverse flow is not perpendicular to the scanning line [81]. If the transverse flow has a positive projection along the positive scanning direction, we define it as a positive flow, and vice versa.

From the axial and transverse flow components, the Doppler angle θ can be derived as $\theta = \tan^{-1}(v_t / v_a)$, which ranges from 0° to 360° . Since the inverse tangent covers angles ranging only from -90° to 90° , θ needs to be adjusted according to the flow direction. In Matlab, function *tan2* can be used instead of *tan* to account directly for the flow direction. The total flow speed v is computed by $v = \sqrt{v_a^2 + v_t^2}$.

3.3.2. Results

Phantom study

Defibrinated oxygenated bovine blood (B-A8775, Materials Bio, hematocrit: 44%) was used for the flow phantom. The blood flowed in a transparent plastic tube (508-001, Silastic, inner diameter $\sim 200\ \mu\text{m}$), driven by a syringe pump (BSP-99M, Braintree Scientific) with a 5 mL syringe (Multifit; Becton, Dickinson & Co). Two experiments were performed using this phantom. First, by changing the pumping speed, the mean flow speed was adjusted from 0 to 7.5 mm/s, with a step size of 0.25 mm/s, while the Doppler angle was fixed at 30° . Second, by mounting the tube on a goniometer stage (GN05, Thorlabs), the Doppler angle was adjusted from 30° to 330° with a step size of 30° , while the mean total flow speed was fixed at 1.0 mm/s. If we take the blood density as $1060\ \text{kg/m}^3$ and the blood viscosity as $3 \times 10^{-3}\ \text{kg/(m}\cdot\text{s)}$ at room temperature, the Reynolds number was estimated to be far less than 1. Therefore, the flow in the tube was considered to be laminar [85]. It is worth mentioning that the $1/e$ penetration depth of light at 590 nm in oxygenated blood is $\sim 130\ \mu\text{m}$, which is greater than the radius of the plastic tube.

In the phantom studies, 3200 consecutive A-lines were acquired at each position across the tube (*M*-mode). For axial flow measurement, each A-line was passed through a digital band-pass filter centered at 50 MHz, with a $-6\ \text{dB}$ bandwidth of 20%. A moving smoothing operation was then performed over each eight sequential A-lines to increase SNR. Fig. 14a is a typical *M*-mode image across the center of the tube, with a Doppler angle of 30° and mean total flow speed of 1.25 mm/s. Fig. 14b shows three representative A-lines with a time interval of 3.3 ms. The axial flow speed profile was then calculated from the average phase shift between two consecutive A-lines after each A-line was Hilbert transformed. For transverse flow measurement, the original

data without filtering was used. The transverse flow was quantified along the lateral direction at each depth, where the bandwidth was computed via the Fourier transformation [80, 81].

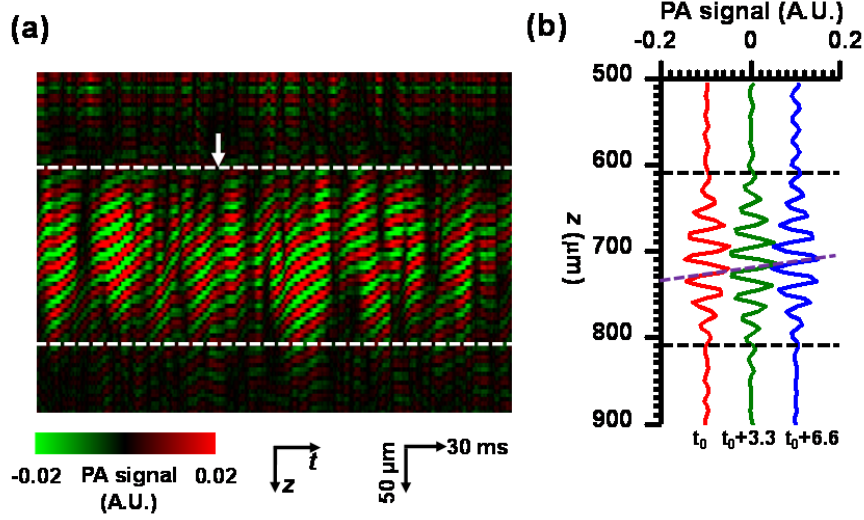


Figure 14. Total flow measurement on bovine blood. (a) An *M*-mode image of the tube with a Doppler angle of 30° and mean total flow speed of 1.25 mm/s after passing through a digital filter. The dashed lines indicate the top and bottom boundaries of the tube. (b) Three representative consecutive A-lines with a time interval of 3.3 ms, where t_0 is indicated by the arrow in (a). The horizontal dashed lines indicate the top and bottom boundaries of the tube. The oblique dashed line shows the phase shifts among these A-lines.

A laminar flow model was used to fit the flow speed profiles along the axial and transverse directions of the tube [86]:

$$v(x, z) = v_{\max} \left(1 - \frac{(x - x_0)^2 + (z - z_0)^2}{R^2} \right). \quad (9)$$

Here, x and z are the transverse and axial coordinates, respective, (x_0, z_0) are the tube center coordinates, R is the tube radius, and v_{\max} is the flow speed at the tube center. While (x_0, z_0) and R can be measured directly from the cross-sectional image of the tube, v_{\max} is the unknown parameter to be fitted for.

For the first phantom study, representative axial and transverse flow profiles calculated from Fig. 14a are shown in Fig. 15a. The measured mean axial and transverse speeds were 1.10 ± 0.09

mm/s and 0.65 ± 0.02 mm/s, respectively. The measured mean total flow speed is 1.28 ± 0.09 mm/s, and the measured Doppler angle is $30.6 \pm 3.0^\circ$, which agrees with the preset value of 30° . Fig. 15b shows the measured mean axial, transverse, and total flow speeds as well as the Doppler angle as a function of the preset speeds. The Doppler angle was not calculated at zero flow speed. From the results, the measured speeds agree well with the preset speeds, and the calculated Doppler angles average $31.0 \pm 2.7^\circ$. The speed measurement errors are less than 0.3 mm/s.

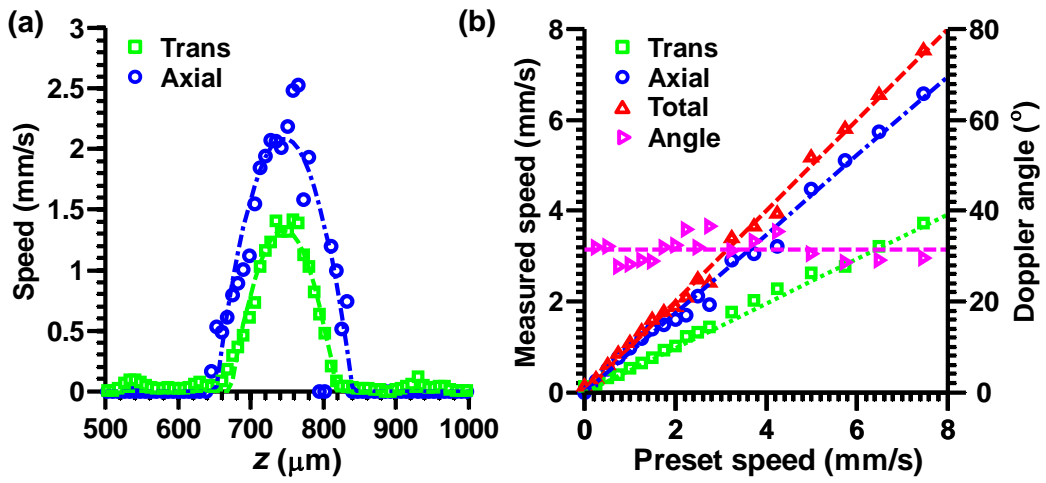


Figure 15. Quantification of total flow measurement with fixed Doppler angle. (a) Transverse and axial speed profiles from Figure 14(a). (b) Measured transverse, axial, total flow speeds as well as the Doppler angle versus the preset total flow speed.

For the second phantom study, Fig. 16a shows representative axial and transverse flow profiles with the same mean total flow speed of 1.0 mm/s but two different Doppler angles (60° and 70°). The weighted mean axial and transverse speeds at 60° measure 0.45 ± 0.03 mm/s and 0.80 ± 0.03 mm/s, respectively, yielding a total flow speed of 0.92 ± 0.03 mm/s and a Doppler angle of $60.6 \pm 1.9^\circ$. The weighted mean axial and transverse speeds at 70° measure 0.33 ± 0.02 mm/s and 0.92 ± 0.10 mm/s, respectively, yielding a total flow speed of 0.98 ± 0.09 mm/s and a Doppler angle of $70.3 \pm 2.3^\circ$. Furthermore, the measured Doppler angles as a function of preset angles are shown in Fig. 16b, which shows good agreement, within 15° .

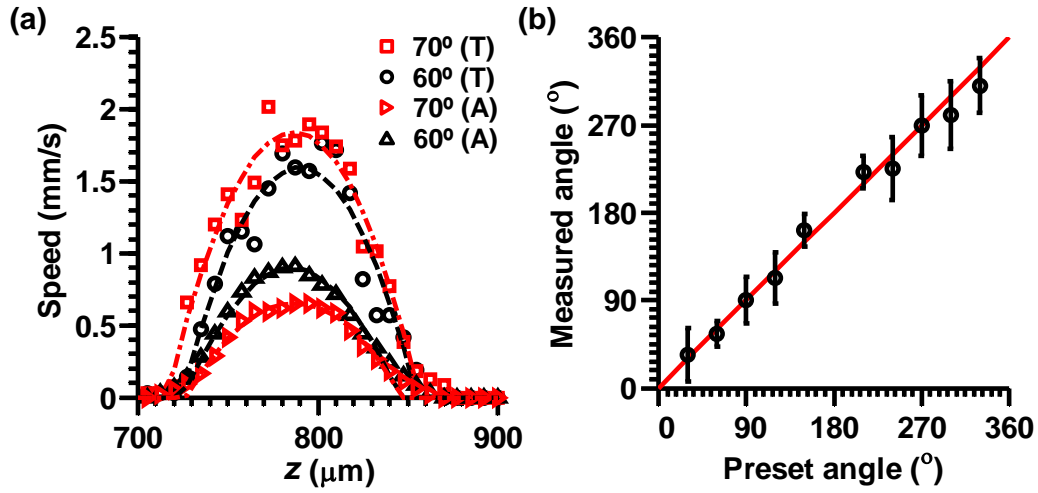


Figure 16. Doppler angle measurement on the bovine blood phantom. (a) Measured speed profiles of the axial and transverse flow along the depth direction, with the same total flow speed (mean: 1.0 mm/s) but different Doppler angles (60° and 70°). T: transverse; A: axial. (b) Measured Doppler angles as the function of preset values.

Animal experiment

The left ear of an adult, 8-week-old nude mouse (Hsd: Athymic Nude-Foxl^{NU}, Harlan Co.; body weight ~20 g) was imaged *in vivo*. During data acquisition, the animal was held steady with a dental/hard palate fixture, and kept still by using a breathing anesthesia system (E-Z Anesthesia, Euthanex). An area of $1.0 \times 0.5 \text{ mm}^2$ at the base of the ear was chosen for total flow measurement. A bi-directional scan was performed over this area to measure the transverse flow direction. Oxygen saturation was then imaged on the same area with 584 nm and 590 nm optical wavelengths. After the experiment, the animal recovered naturally and was returned to its cage. The flow processing for the *in vivo* experiment was the same as that for the phantom study, except that a $1.0 \times 0.5 \text{ mm}^2$ area instead of only a cross-section was imaged. The absolute C_{Hb} and $s\text{O}_2$ were computed using the previously published acoustic spectral method [87] and multi-wavelength method [88], respectively.

A typical artery-vein pair at the base of a nude mouse ear was imaged (Fig. 17a). The morphology indicates that the thicker vessel of the pair is the vein, which is confirmed by the sO₂ measurement (Fig. 18a). The volumetric rendering (Fig. 17b) shows that the Doppler angles of the artery and vein at the proximal ends were approximately 82.5° and 255.5°, respectively (Fig. 17c).

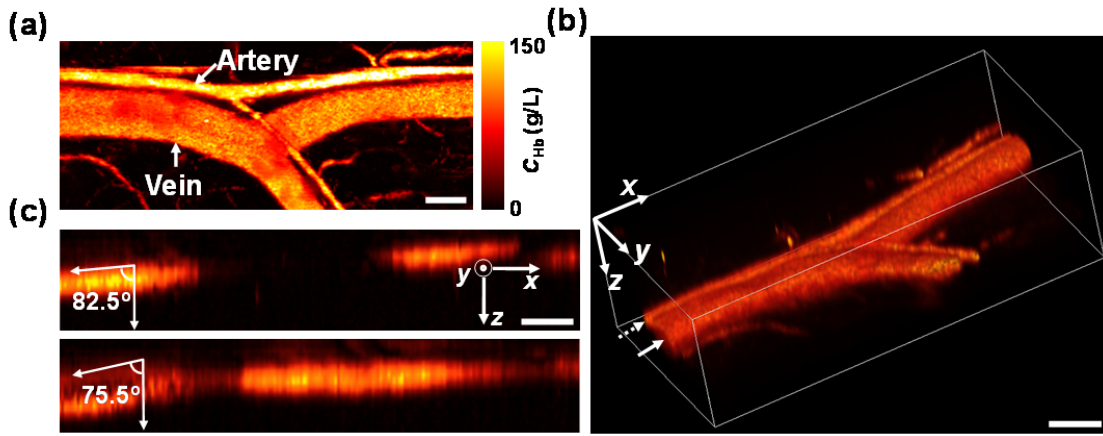


Figure 17. Three-dimensional PAM of a mouse ear. (a) Maximum amplitude projection of the total hemoglobin concentration image of an artery-vein pair of the mouse ear. Scale bar: 100 μ m. C_{Hb} : total hemoglobin concentration. (b) Volumetric rendering of the same area as (a). Scale bar: 100 μ m. (c) Sagittal cross-section images of the artery (top) and vein (bottom), indicated by the dashed and solid arrows in (b), respectively. The Doppler angles were estimated to be 82.5° and 78.5°, respectively. Scale bar: 100 μ m.

The maximum projection of total flow speed is shown in Fig. 18b, where the artery has faster flow than the vein. The transverse speeds at the centers of the artery and vein were 3.9 ± 0.25 mm/s and 1.1 ± 0.20 mm/s, respectively, as shown in Fig. 18c. The transverse flow directions show that the blood in the artery indeed flowed from the proximal end to the distal end, and flowed in the opposite direction in the vein. The axial speeds at the centers of the artery and vein were 0.9 ± 0.25 mm/s and 0.4 ± 0.02 mm/s, respectively, as shown in Fig. 18d. The axial flow directions show that the blood flowed towards the transducer in the artery, but away from the transducer in the vein. Based on the above information, the total flow speeds at the centers of the

artery and vein were 4.0 ± 0.25 mm/s and 1.2 ± 0.19 mm/s, respectively. The Doppler angles at the centers of the artery and vein were $77.0 \pm 3.6^\circ$ and $250.0 \pm 3.5^\circ$, respectively, which were consistent with the measurements from the volumetric image.

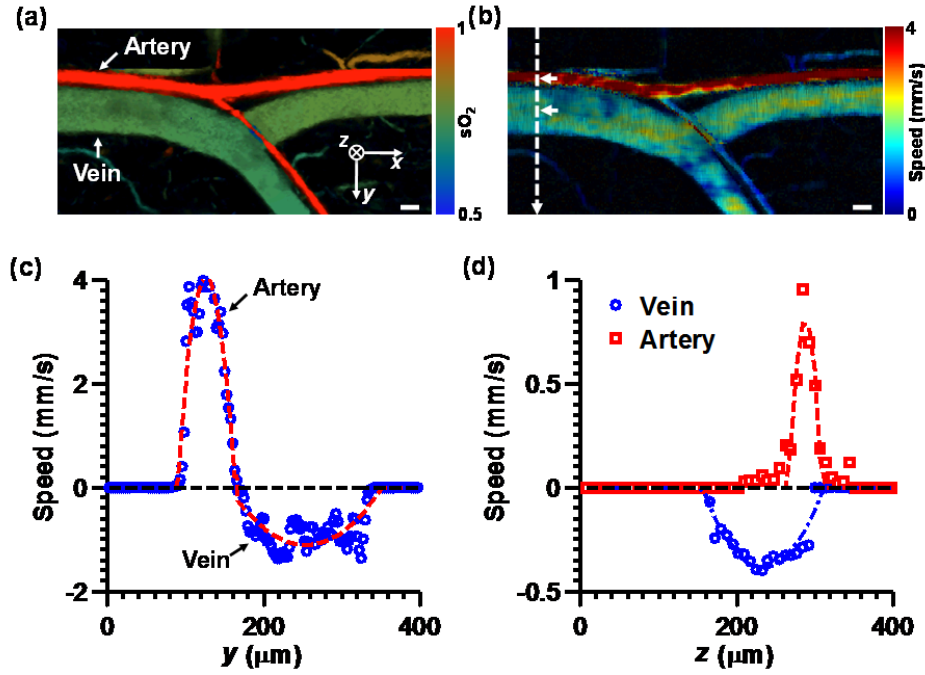


Figure 18. Total flow measurement in mouse ear. (a) sO₂ image of the same area as that in Fig. 17. (b) Total flow speed image of the same area. (c) Transverse speed profiles along the dashed line in (b). Positive transverse flow direction: from left to right. (d) Axial speed profiles along the depth direction at the centers of the artery and vein, indicated by the arrows in (b). Positive axial flow direction: towards the ultrasonic transducer.

3.3.3. Conclusions and discussion

We have demonstrated a method for measuring both total flow velocity and Doppler angle using PAM. By Combining blood flow information with other anatomical and functional parameters such as vessel cross-sections, C_{Hb} and sO₂, we can quantify the metabolic rate of oxygen (MRO₂) for cancer hypermetabolism studies [89]. The advantage of this method is simplicity: No system modification or additional data acquisition is required to use our existing PAM. Both the axial and transverse flow components are measured in *M*-mode. Collating the A-lines side by side

yields a 2D matrix. The axial direction of this matrix (column) is called the fast axis (depth), whereas the lateral direction (row) is called the slow axis (time). The columns are Hilbert transformed to compare the phases for the computation of the axial flow. The rows are Fourier transformed to quantify the bandwidth for the computation of the transverse flow.

In general, both axial and transverse flow directions should be measured to determine the total flow direction. Because blood can only flow along the blood vessels, only one of the two directions is required to be measured as long as the blood vessel can be resolved precisely. However, when there is no axial flow and the transverse flow direction is perpendicular to the bi-directional scanning, four-directional scanning is required.

In theory, the maximum measurable axial and transverse flow speeds are 60.0 mm/s and 21.2 mm/s, respectively, limited by the 3 kHz PRF [65, 78, 81]. The minimum measureable axial and transverse speeds are ~ 0.1 mm/s, determined by the PRF and SNR [78, 81, 90]. In our studies, since the PRF can be as slow as 1 Hz at the expense of imaging speed, it is the SNR that limits the minimum measureable speeds.

3.4. Photoacoustic microscopy in metabolic rate of oxygen measurement

The energy demand of mammals is met primarily by aerobic metabolism, producing 88% of ATP molecules [91]. Therefore, the metabolic rate of oxygen (MRO_2) is an important indicator of tissue viability and functionality. It is known that nearly all cancers after the early stage are starved for oxygen (hypoxia) due to hypermetabolism and/or limited blood supply, regardless of their cellular origins [92]. In the presence of low oxygen pressure, highly malignant cancer cells survive and proliferate via glycolysis (anaerobic respiration, the Warburg effect). The presence of a large number of hypoxic regions within a tumor usually correlates with a poor prognosis

[91]. This metabolic phenotype has become the basis for tumor imaging by positron emission tomography (PET) using radioactively labeled oxygen. Many other pathological and physiological functions are also closely related to alterations of oxygen metabolism: examples include Alzheimer's disease [93], diabetes [94], burns [95], obstructive pulmonary disease [96], congestive heart failure [97], aging [98], sleeping [99], and physiologic challenges [100]. Therefore, an accurate measurement of MRO_2 has the potential to provide a powerful tool for diagnosis and therapy of cancer and other diseases as well as for metabolism-related pathophysiological studies.

Compared with other oxygenation indexes of tissue, i.e., oxygen saturation of hemoglobin (sO_2) and partial oxygen pressure (pO_2), MRO_2 is superior because it directly reflects the rate of oxygen consumption instead of the static oxygen concentration [101]. If the region of interest has well-defined feeding and draining vessels, we have [5]

$$\text{MRO}_2 = \varepsilon \times C_{\text{Hb}} \times \left(\text{sO}_{2in} \times A_{in} \times \bar{v}_{in} - \text{sO}_{2out} \times A_{out} \times \bar{v}_{out} \right) / W. \quad (10)$$

Here, subscripts *in* and *out* denote feeding and draining vessels, respectively. ε is the oxygen binding capacity of hemoglobin and is usually taken as a constant (1.36 ml O_2 /gram hemoglobin) [102]. C_{Hb} is the total hemoglobin concentration (in grams of hemoglobin/ml blood). sO_2 is the average oxygen saturation (in %). A is the cross-sectional area (in mm^2). \bar{v} is the average blood flow speed (in mm/s). W is the weight of the region of interest (in grams). While C_{Hb} can be estimated anywhere in the trunk vasculature, the other parameters must be measured locally.

Presently, three primary imaging modalities are used to quantify MRO_2 [5]. Among them, PET is most widely used in clinical practice. However, the need for injection or inhalation of radioactively labeled exogenous tracers results in a complex procedure with exposure to ionizing

radiation, limiting its usage [103]. Functional magnetic resonance imaging (fMRI) has also been intensively used for MRO_2 study, especially in the brain. fMRI is limited to qualitative evaluation of only temporal changes in MRO_2 and has difficulty in measuring both C_{Hb} and sO_2 [104]. It also must switch between different imaging protocols to measure sO_2 and \bar{v} [105, 106]. Moreover, both PET and fMRI are expensive. Diffuse optical tomography (DOT) is also capable of measuring MRO_2 and is relatively inexpensive, but it relies on an approximate theoretical model or other techniques (e.g., Doppler ultrasound and laser Doppler) to provide blood flow information [107, 108]. Recently, DOT has been combined with diffuse correlation spectroscopy (DCS), which is capable of providing relative blood flow information [109]. Furthermore, due to their relatively poor spatial resolutions, PET, fMRI and DOT usually measure MRO_2 averaged over a large volume [21].

Here, we overcome these limitations by using photoacoustic microscopy. We demonstrated that all five anatomic, chemical and fluid-dynamic parameters for MRO_2 quantification can be obtained in absolute units by mPAM alone *in vivo*. Specifically, All the parameters for MRO_2 quantification in Eq. (10) can be simultaneously obtained by mPAM. Specifically, anatomic parameters W and A are quantified from the structural mPAM image [74]; functional parameters C_{Hb} and sO_2 are measured by laser excitation at two wavelengths [33, 74]; fluid-dynamic parameter \bar{v} is estimated on the basis of photoacoustic bandwidth broadening of the PA signal induced by circulating red blood cells [80, 110]. The structural image acquisition time is ~ 25 min for a $4 \text{ mm} \times 4 \text{ mm}$ region (~ 1 Hz frame rate) using single wavelength; the oxygenation image acquisition time is ~ 20 min for a $1 \text{ mm} \times 1 \text{ mm}$ region using two wavelengths (~ 0.3 Hz frame rate); the flow speed acquisition time is ~ 5 min for a 0.5 mm cross-sectional line using single wavelength.

To validate mPAM, first we studied the MRO_2 responses to hyperthermia and cryotherapy, two common therapeutic techniques. Furthermore, mPAM was used to image melanoma and glioblastoma longitudinally, demonstrating its capability of early cancer detection.

3.4.1. Methods

Animal model. The nude mouse ear is a good model for validating mPAM because of its similarity to human skin and lack of motion artifacts [111-113]. Each artery-vein pair (AVP) feeds a well-defined region while one pair at the base of the ear feeds the entire ear (Fig. 19) [114, 115]. Consequently, the MRO_2 based on each AVP approximates the MRO_2 of its supplied region.

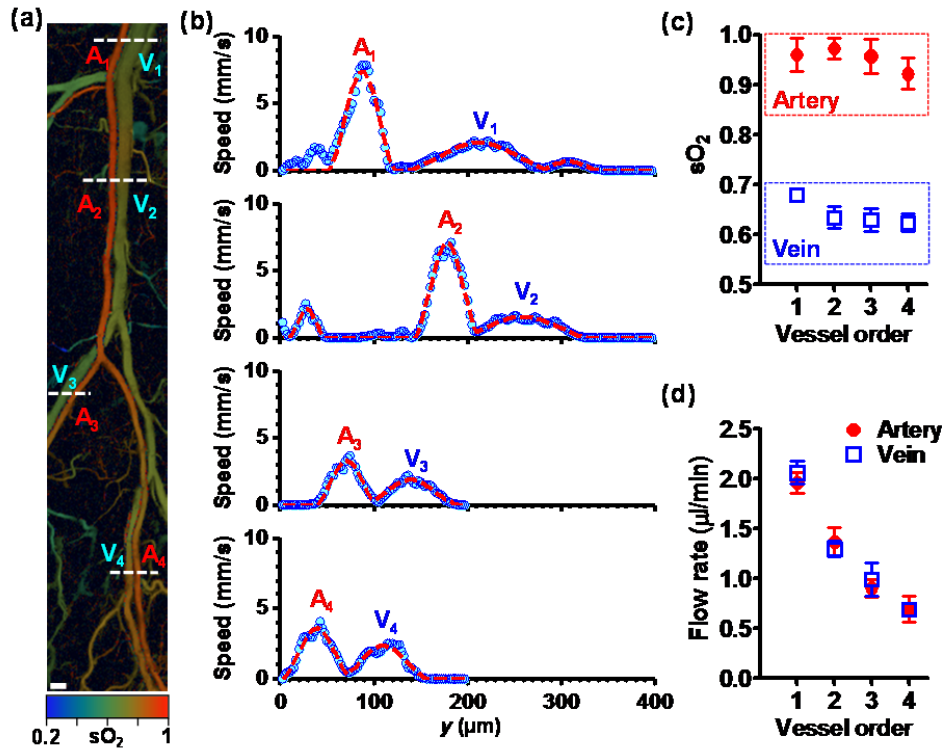


Figure 19. mPAM measurements of oxygen saturation ($s\text{O}_2$) and blood flow on four orders of artery-vein pairs in the mouse ear. (a) $s\text{O}_2$ mapping from two measurements at 584 nm and 590 nm. Four different orders of artery-vein pairs are labeled. Scale bar: 125 μm . (b) Profiles of blood flow speed across vessels of different

orders measured along the dashed lines in (a) on the basis of PA bandwidth broadening at 584 nm. Generally, the flow speed decreases from the proximal order to the distal order. However, it also depends on the vessel diameter as a result of the conservation of total flow. Solid circles: experimental data; red curves: fit. (c) Mean sO_2 versus the vessel order, quantified along the centerline of each vessel. The sO_2 values in both the arteries and veins change slightly with the vessel order, especially at distal branches. This is probably due to oxygen diffusion between the arteries and veins, and the inhomogeneous MRO_2 . (d) Blood flow rate (in $\mu\text{l}/\text{min}$) versus the vessel order, quantified from the flow speed profiles and vessel diameters. Blood flow in both arteries and veins decreases from the proximal order to the distal order, and is conserved between the artery and vein of the same order. The blood fed by the artery is mostly drained by the corresponding vein of the same order. V: vein; A: artery.

Hyperthermia experimental protocol

In the hyperthermia study, the animal's temperature was regulated by adjusting the water temperature in the heating pad placed underneath its abdomen. The water was circulated by a water-bath system (ISOTEMP 9100, Fisher Scientific). A cotton layer between the heating pad and the animal skin buffered and homogenized the temperature change and thus protected the animal from burns. The room temperature was kept at 23 °C. The animal's skin temperature (SKT) was monitored on the dorsal pelvis by an attached electronic thermometer (Radio Shack, Cat. No. 63-854). Before the experiment, the SKT was adjusted to 31 °C, which was used as the baseline. The experiment was divided into three periods. The animal was first monitored at baseline temperature for ~40 min (the resting period), then heated for ~30 min by increasing the heating pad to 50 °C (the heating period), and lastly allowed to cool to baseline for ~100 min (the recovery period). The hemodynamic parameters were simultaneously measured on the principal artery-vein pair (AVP) using mPAM. Each measurement took ~6 min, and the whole experiment lasted for ~3 hrs.

Tumor cell culture

B16 mouse melanoma cells were obtained from the Tissue Culture and Support Center at the Washington University School of Medicine. The cells were maintained in Dulbecco's modified Eagle medium (DMEM, Invitrogen, Carlsbad, CA) supplemented with 10% FBS and 1% P/S.

U87 MG human brain glioblastoma cells (HTB-14) were obtained from American Type Cell Culture (ATCC). The cells were maintained in Eagle's Minimum Essential Medium (EMEM, Invitrogen) supplemented with 10% heat-inactivated fetal bovine serum (FBS, ATCC) and 1% penicillin-streptavidin (P/S, Invitrogen). The cultures were performed at 37 °C and 5% CO₂, and the cells were passaged weekly.

Inoculation of tumor cells

In the tumor study, 0.01 ml of suspension containing ~0.5 million B16 melanoma cells or U87 human glioblastoma cells was inoculated into the top skin layer in the left ear of a nude mouse, using a 0.3 ml syringe with a 29-gauge needle. The injection was usually located near the second order branch of the principal AVP above the cartilage. The tumor was allowed to grow and monitored for one to three weeks. A control measurement was performed before the tumor cell injection (day 0).

Hemodynamics measured by mPAM

The hemodynamic parameters were monitored using mPAM on the principal AVP, which included vessel diameter, total hemoglobin concentration, oxygen saturation, blood flow direction, and flow speed.

1. Vessel diameter. The vessel diameter was measured along a cross-section perpendicular to the vessel centerline. A threshold of two times the noise level was empirically set to separate the background and vessel. The transverse dimension of the vessel cross-section was taken as the vessel diameter D , in case the excitation light could not penetrate the whole vessel in the axial direction. Then the vessel cross-section area was calculated as

$A = \pi(D/2)^2$. Five adjacent cross-sections were measured, and the mean value of the principal vein was used for MRO_2 calculation.

2. Total hemoglobin concentration. Since oxy-hemoglobin and deoxy-hemoglobin have the same absorption coefficient at 584 nm, the PA signal amplitude is proportional to the total hemoglobin concentration regardless of the oxygen saturation level [116]. On the basis of a previous study [117], the total hemoglobin concentration was set to be 146.0 g/l at baseline temperature (the hyperthermia study) and on day 0 (the tumor and cryotherapy studies). The sequential data sets were calibrated accordingly. The averaged PA signal amplitude along the centerline of the principal vein was used for calculation.
3. Oxygen saturation. The oxygen saturation (sO_2) was measured using laser excitations at 584 nm and 590 nm, respectively [33]. The relative change in molar extinction coefficient is ~58.4% for oxy-hemoglobin and 17.5% for deoxy-hemoglobin, respectively. Because the vessels studied here were big enough ($> 50 \mu\text{m}$) and the laser pulse energy was low (~100 nJ), the difference of penetration depth won't affect the results much. The PA signal at each wavelength was normalized with the laser pulse energy, as monitored by a wavelength-calibrated photodiode. The averaged sO_2 along the vessel centerline was used for MRO_2 calculation. The PA image acquired at 584 nm was used as a mask on the sO_2 image to remove the background noise.
4. Blood flow direction. The blood flow direction was measured on the basis of photoacoustic bandwidth broadening with bidirectional motor scanning at 584 nm [80]. The laser repetition rate was 3 KHz, and the scanning step size was $0.625 \mu\text{m}$. We used 64 sequential A-lines to calculate the bandwidth broadening. If the blood flow had a positive projection along the positive scanning direction, we defined it as a positive flow,

and vice versa. The mPAM image acquired at 584 nm was used as a mask on the flow image to remove the background noise.

5. Blood flow speed. To better estimate the flow speed, *M*-mode imaging at 584 nm was used to measure the bandwidth broadening across the vessel. The laser repetition rate was 3 KHz, and 3200 A-lines were acquired at each position. The flow speed at each position was calculated on the basis of the bandwidth broadening. The average amplitude of the PA signal at each position was used as a mask on the speed profile to remove the background noise. The mean flow speed of the principal vein was used for MRO_2 calculation.

Melanoma volume estimation using mPAM

After data acquisition, the PA signal amplitude acquired at each optical wavelength was extracted through the Hilbert transformation. The tumor region was then separated from the surrounding blood vessels according to the mPAM image acquired at 605 nm, where melanin has much stronger absorption than blood. A threshold of 20% of the maximum signal amplitude was set to segment the tumor. Since it was challenging to penetrate through the whole tumor due to the high absorption of melanin, a 3D envelope of the tumor region was obtained from the surface signal instead. The volume of the tumor was then calculated by integrating the corresponding voxels enclosed by the envelope. All the image processing was conducted using the MATLAB Image Processing Toolbox (R2008a, MathWorks).

Fitting for the profile of blood flow speed

A theoretical model was used to fit the profile of the blood flow speed across the vessel [86],

$$v(x) = v_{\max} \times \left[1 - \left(\frac{x - x_0}{R} \right)^n \right] \quad (11)$$

Here, x is the transverse location; x_0 is the vessel center; R is the vessel radius; v_{\max} is the flow speed at the vessel center; and n is the power index that characterizes the flow profile (e.g., $n = 2$ for laminar flow). While x_0 and R can be measured directly from the mPAM images of the vessel structure, v_{\max} and n are the unknown parameters to fit for.

Statistical analysis

Quantitative data was expressed as mean \pm s.e.m. The statistical test is a paired Student's t -test (two-tailed with unequal variance), compared with the baseline levels (hyperthermia and cryotherapy studies) or day 0 (tumor studies). We considered a p -value less than 0.05 to be statistically significant.

3.4.2. Results

MRO₂ quantification under normothermia

As an example, we measured the MRO₂ of a mouse ear under normothermia. The animal's temperature was regulated with a heating pad placed under its abdomen (skin temperature: 31 °C), a volumetric image was acquired using mPAM at 584 nm by scanning a 10 mm \times 8 mm area containing the principal AVP (Fig. 20a). Because 584 nm is an isosbestic wavelength for hemoglobin, this image maps the concentration of total hemoglobin regardless of the oxygen saturation level. In addition, it measures the diameters of the principal AVP (artery: ~ 65 μ m; vein: ~ 116 μ m). Two PAM images acquired at 584 nm and 590 nm were then used to calculate sO₂ (Fig. 20b) [74]. The vessels with high sO₂ values ($>90\%$) are classified as arteries, whereas

the vessels with low sO_2 values (60–80%) are veins. The blood flow velocity was measured at 584 nm using bi-directional scanning with a laser repetition rate of 3 KHz and a motor step size of 0.625 μm (Fig. 20c). The profile of flow speed across the principal AVP is shown in Fig. 20d. The artery and the vein have a mean flow speed of 5.5 mm/s and 1.8 mm/s, respectively, and the speed profiles are both approximately parabolic [86]. The weight of the mouse ear was computed by its volume in the 3D PA image, where the average specific weight was assumed to be 1.0 g/ml [118]. From these measurements, the MRO_2 of the mouse ear was estimated to be 0.23 ml/100 g/min, which agrees with the data previously measured in humans [92].

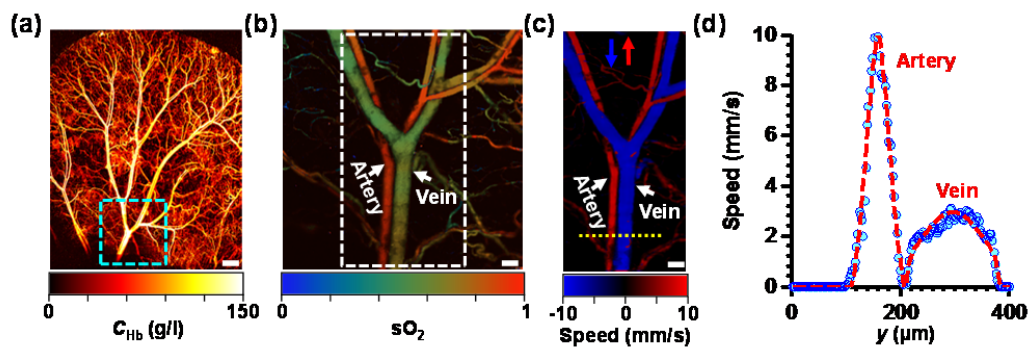


Figure 20. Label-free quantification of metabolic rate of oxygen (MRO_2) *in vivo*. (a) mPAM image of the total concentration of hemoglobin (C_{Hb}). Scale bar: 500 μm . (b) mPAM image of the oxygen saturation of hemoglobin (sO_2) in the area indicated by the dashed box in (a). Scale bar: 125 μm . (c) mPAM image of blood flow in the area indicated by the dashed box in (b). Red arrow: positive scanning direction; blue arrow: negative scanning direction. Positive velocity: upward flow. Scale bar: 125 μm . (d) Profile of blood flow speed across the dashed line in (c).

Change in MRO_2 induced by systemic hyperthermia

Hyperthermia has been clinically used for cancer treatment [119]. To measure MRO_2 during hyperthermia, the mouse's skin temperature was elevated to 42 $^{\circ}\text{C}$ (Fig. 21a). Hemodynamics were monitored on the principal AVP. The vessel diameter started increasing at the beginning of the heating period (Fig. 21b), and reached a maximum by the end of the heating period. The total hemoglobin concentration of the principal AVP kept increasing after the heating started, and

plateaued when the temperature returned to the baseline (Fig. 21c). This cumulative effect was due to a decrease in blood plasma volume resulting from water loss during hyperthermia [120]. From the change in sO_2 (Fig. 21d), we found that the oxygen extraction fraction (OEF, defined as $(sO_{2in} - sO_{2out}) / sO_{2in}$ and represents the fraction of O_2 molecules that cross the capillary wall) decreased by 12% over the heating period and eventually recovered to 99% of the resting level (Fig. 21f). The measurements of flow speed in the arteries during the heating were saturated because of the limited maximum measurable speed of the system (Fig. 21e). From the measurements on the principal veins, we found the volumetric flow rate of blood entering the ear increased by 45%. Increased cardiac output and redistribution of blood to the skin are two major reasons for vessel dilation and faster blood flow, which help accelerate heat exchange with the environment [119, 121]. Note that the vessel diameter, sO_2 , and blood flow speed reach the peaks approximately simultaneously.

The MRO_2 of the mouse ear, as computed from the hemodynamic changes, increased by 28% over the heating period (Fig. 21f), which indicated elevated oxygen metabolism during hyperthermia in response to an increased rate of enzymatic reactions [122]. This finding can potentially elucidate another possible mechanism for cell death induced by hyperthermia. When normal cells encounter such an increased metabolism, increased blood flow provides more nutrients. By contrast, cancer cells could be damaged owing to inadequate blood circulation. Therefore, hyperthermia may kill cancer cells by both protein denaturation and cell starvation due to heating.

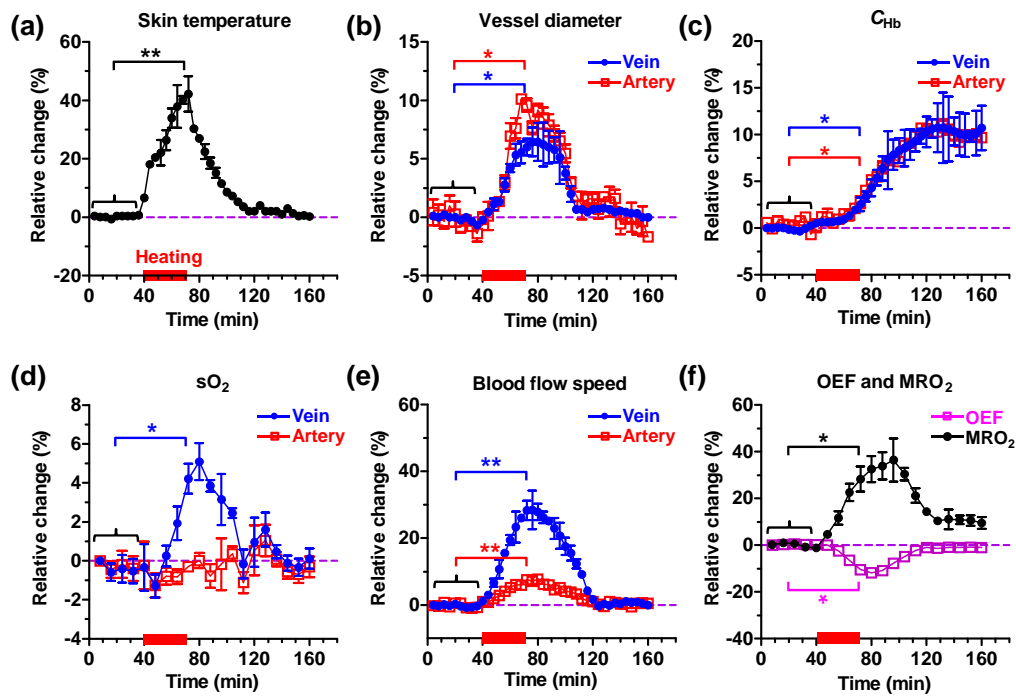


Figure 21. mPAM measurement of hemodynamic responses to a hyperthermic challenge (red bars). Relative changes of (a) the skin temperature, (b) vessel diameter, (c) total hemoglobin concentration, (d) oxygen saturation (sO_2), (e) blood flow speed, and (f) oxygen extraction fraction (OEF) and metabolic rate of oxygen (MRO_2). Statistics: paired Student's t -test. * $p < 0.05$, ** $p < 0.01$, $n = 3$. Data are presented as means \pm s.e.m. The baseline values are (a) temperature: 31.0 ± 0.4 °C, (b) vessel diameters: 92.5 ± 10.5 μ m (vein) and 47.5 ± 8.5 μ m (artery), (c) C_{Hb} : 146.3 ± 18.1 g/l (vein) and 148.5 ± 14.0 g/l (artery), (d) sO_2 : 0.70 ± 0.08 (vein) and 0.94 ± 0.04 (artery), (e) flow speeds: 1.3 ± 0.4 mm/s (vein) and 5.1 ± 0.8 mm/s (artery), (f) 0.26 ± 0.13 (OEF) and 0.30 ± 0.09 ml/100 g/min (MRO_2).

Change in MRO_2 induced by local cryotherapy

Cryotherapy has been found effective for treating cancer and other diseases by forming ice crystals inside cells [123, 124]. Here, we applied liquid nitrogen to the mouse ear surface for 10 seconds via a 1 mm diameter cryo-probe, and monitored the hemodynamics of the treated area (Figs. 22a-b). An untreated neighboring area of the same ear was also monitored as a control. Right after the treatment, a global reflective vasodilatation was observed on both the treated and control areas, which was accompanied by an increase in blood flow and a decrease in OEF. While the MRO_2 of the control area remained unchanged statistically, the MRO_2 of the treated

area decreased by 56% due to the induced cell death. Therefore, mPAM can be used to evaluate the efficacy of cryotherapy.

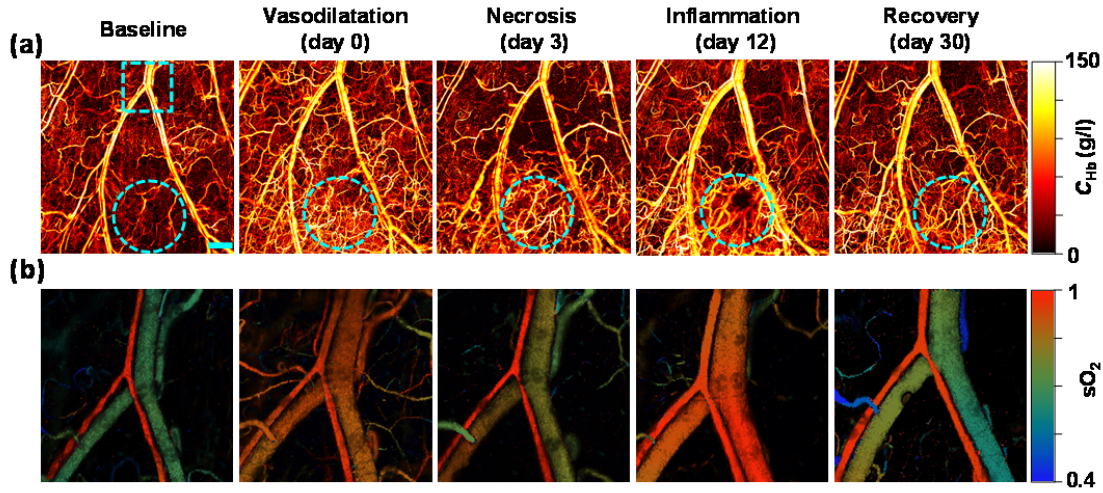


Figure 22. mPAM monitoring of hemodynamic responses after cryotherapy. (a) mPAM vasculature images acquired in different phases before and after the application of liquid nitrogen. The treated area is indicated by cyan dashed circles. Scale bar: 500 μ m. (b) mPAM images of oxygen saturation (sO_2) in the artery-vein pair [cyan dashed box in (a)] that supports the treated area. Scale bar: 125 μ m.

Within one month after the treatment, while all the parameters of the control area monotonically recovered to the baseline, the physiological progress of the treated area occurred in phases (Figs. 23a-c). Within three days following the reflective vasodilatation, blood flow and OEF trended toward the baseline, but MRO_2 remained at a low level due to cell necrosis. Starting from day 5, inflammation was clearly observed, which was triggered by the immune system and was helpful for both dead cell clearance and new cell growth. Although the OEF continued to decrease due to the increased flow speed [101], the MRO_2 of the treated area eventually returned to the baseline, reflecting improved tissue viability. One month later, the inflammation nearly ended, and all the parameters had recovered almost to the baseline.

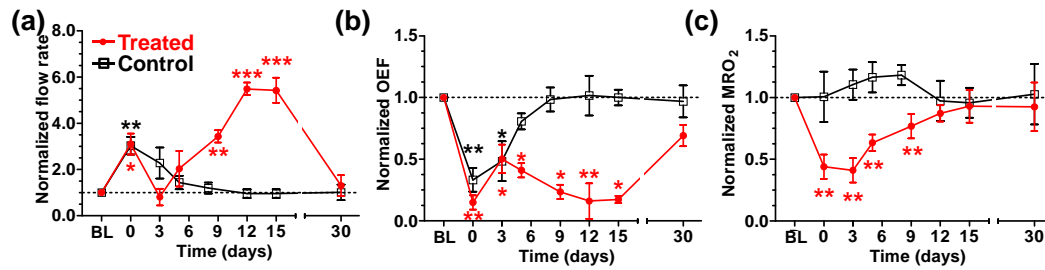


Figure 23. mPAM quantification of blood flow rate (a), oxygen extraction fraction (OEF) (b) and metabolic rate of oxygen (MRO₂) (c) within 30 days after the treatment. A neighboring area close to the treated region was monitored as a control. Statistics: paired Student's *t*-test. * *p* < 0.05, ** *p* < 0.01, *** *p* < 0.001, *n* = 4. Data are presented as means ± s.e.m. Baseline flow rates: 0.72 ± 0.12 µl/min (treated) and 0.44 ± 0.15 µl/min (control); baseline OEF: 0.35 ± 0.04 (treated) and 0.31 ± 0.05 (control); baseline MRO₂: 0.30 ± 0.06 ml/100 g/min (treated) and 0.25 ± 0.07 ml/100 g/min (control). BL: baseline.

This study shows that each physiological phase after cryotherapy imparts its signature on the local MRO₂. The common belief is that inflammation triggered by the immune response further helps kill tumor cells [125]. However, our results show that the increased blood flow rate during inflammation may assist the survival of residual tumor cells by providing more nutrients and thus recovering the MRO₂ level.

Early cancer detection by measuring tumor-induced change in MRO₂

The third demonstration of mPAM is early cancer detection by measuring MRO₂. The hemodynamics of the mouse ear were longitudinally monitored after the injection of B16 melanoma cells (Fig. 24a). On day 7, vessel dilation appeared around the tumor site as shown in Fig. 24b and Fig. 25b. The volumetric blood flow rate increased by 1.5 fold (Fig. 24c and Fig. 25e). These changes are important to ensure the supply of oxygen and nutrients to the rapidly growing tumor, and to provide routes for tumor cell metastasis [126]. The overall OEF of the tumor region decreased by 43% (Fig. 24c and Fig. 25f) due to the increased blood flow [101].

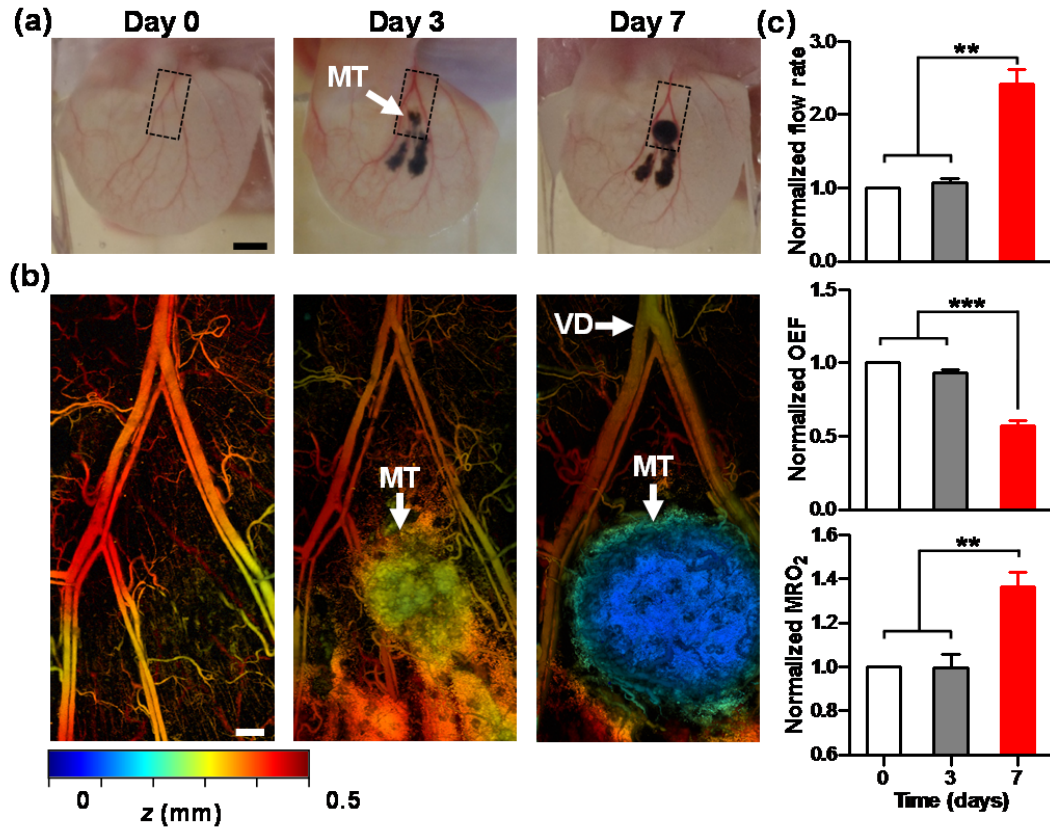


Figure 24. mPAM detection of early-stage melanoma by measuring metabolic rate of oxygen (MRO₂). (a) White-light photographs of a representative mouse ear before (day 0), 3 days and 7 days after the xenotransplantation of B16 melanoma tumor cells. Scale bar: 1 mm. (b) mPAM images of the tumor region [dashed boxes in (a)] at 584 nm. *z* is coded by colors: blue (superficial) to red (deep). Scale bar: 125 μ m. (c) mPAM quantification of blood flow rate, oxygen extraction fraction (OEF) and metabolic rate of oxygen (MRO₂) before (day 0), 3 days and 7 days after the tumor xenotransplantation, normalized by the values of day 0 (flow rate: 1.77 ± 0.50 μ l/min; OEF: 0.31 ± 0.04 ; MRO₂: 0.38 ± 0.03 ml/100 g/min). Statistics: paired Student's *t*-test. ** $p < 0.01$, *** $p < 0.001$, $n = 5$. Data are presented as means \pm s.e.m. MT: melanoma tumor; VD: vasodilatation.

The vasculature and melanoma were differentiated according to their different absorption spectra using dual-wavelength excitation at 584 nm and 605 nm, and thus the tumor volume could be estimated (Fig. 26).

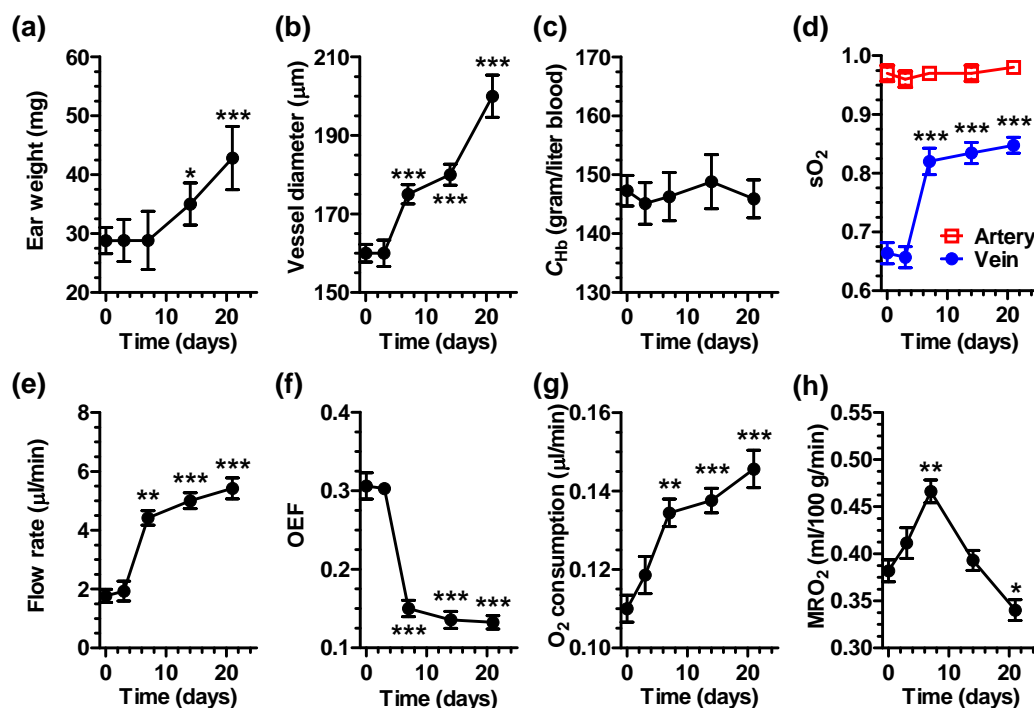


Figure 25. mPAM measurements in absolute units of (a) ear weight, (b) vessel diameter, (c) total hemoglobin concentration, (d) oxygen saturation of hemoglobin (sO_2), (e) volumetric blood flow rate, (f) oxygen extraction fraction (OEF), (g) rate of O_2 consumption in $\mu\text{L}/\text{min}$, and (h) metabolic rate of oxygen (MRO_2) in $\text{ml}/100 \text{ g}/\text{min}$ up to 21 days after tumor inoculation. Statistics: paired Student's t -test. * $p < 0.05$, ** $p < 0.01$, *** $p < 0.001$, $n = 3$. Data are presented as means \pm s.e.m.

The hypermetabolism of melanoma was reflected by 36% increase in MRO_2 (Fig. 24c), which proves the early cancer detection capability of mPAM. The presence of the melanoma was confirmed by histology (Fig. 27). However, the melanoma was hyperoxic instead of hypoxic in the early stage (Fig. 25d). On day 14, MRO_2 dropped to the baseline level and continued to decrease (Fig. 25h), even though the total oxygen consumption rate increased steadily (Fig. 25g). There are two possible reasons for the final decline in MRO_2 . On one hand, a tumor changes to anaerobic respiration instead of aerobic respiration when it grows too quickly to get sufficient oxygen [92]; on the other hand, when the tumor grows too large, the tumor core dies due to a

decrease in available nutrients (necrosis). The necrotic tumor core does not consume oxygen but increases tumor weight (Fig. 25a), which decreases the MRO_2 [127].

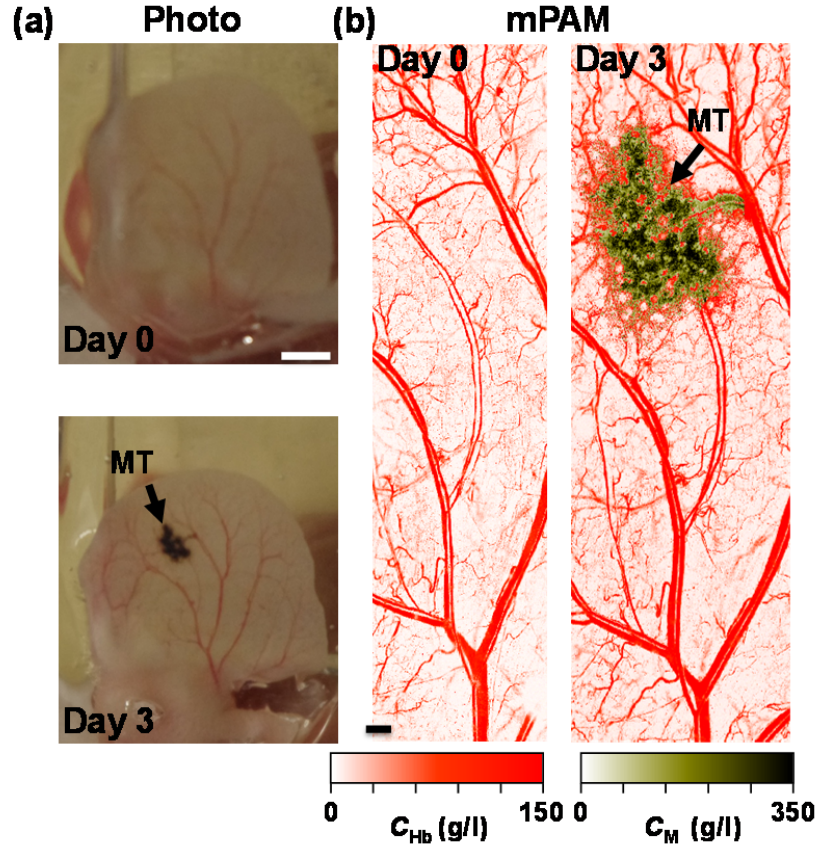


Figure 26. mPAM differentiation of blood vessels and melanoma. (a) White-light photographs of a representative mouse ear before and 3 days after the xenotransplantation of B16 melanoma cells. Scale bar: 1 mm. (b) Composite mPAM images of blood vessels (in red) and melanoma (in brown). The two are differentiated by using dual-wavelength excitation at 584 nm and 605 nm. C_{Hb} : total hemoglobin concentration. C_M : melanin concentration. Scale bar: 250 μ m. MT: melanoma tumor.

Besides melanoma, we also studied U87 human glioblastoma (Fig. 28a), which is more transparent; thus, its intratumoral vasculature can be better visualized. On day 7, angiogenesis was observed within the tumor region (Fig. 28b), and the sO_2 of the draining vein was found to be increased, indirectly indicating early-stage tumor hyperoxia (Fig. 28c). The presence of the glioblastoma was confirmed by histology (Fig. 29). While the increase in blood supply for the

glioblastoma was comparable with that for the melanoma, the OEF showed a decrease by 24% instead of 43% (Fig. 28d). We observed a 100% increase in MRO_2 instead of 36% for the melanoma, which indicated a stronger hypermetabolism at the early stage of glioblastoma. However, characteristic of early-stage cancer [128], such hypermetabolism did not lead to tumor hypoxia. In fact, the sO_2 in the intratumoral vasculature was even higher than that of the surrounding normal tissue, directly indicating early-stage tumor hyperoxia (Fig. 28e and Fig. 30). The increase in sO_2 actually caused the decrease in OEF in the tumor. This observation suggests that hypoxia-based diagnosis may not apply to early-stage cancer [129].

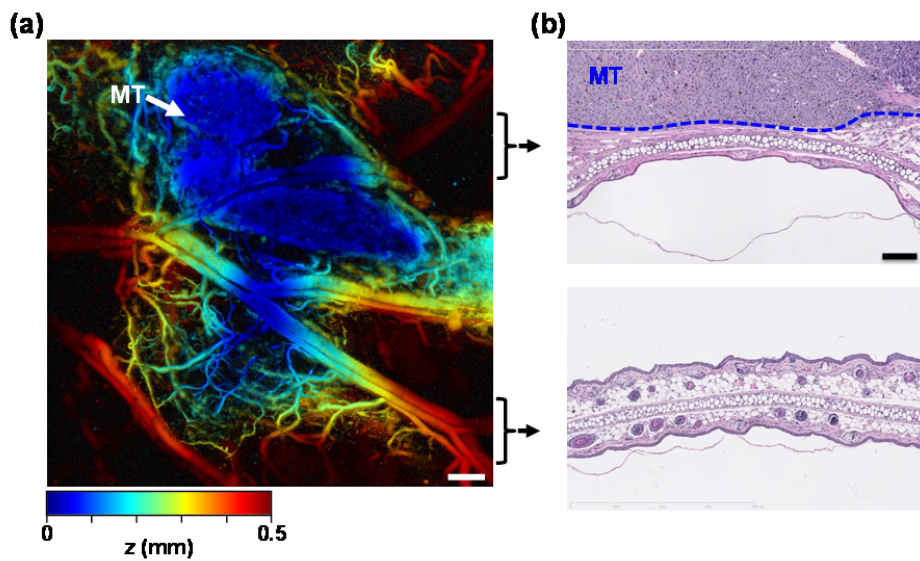


Figure 27. Histological validation of melanoma detection. (a) mPAM image of a mouse ear bearing a B16 melanoma tumor acquired on day 7. z is coded by colors: blue (superficial) to red (deep). Scale bar: 300 μm . (b) Images of H&E stained tissue slices cut approximately across the tumor area (top) and non-tumor area (bottom). Scale bar: 150 μm . MT: melanoma tumor.

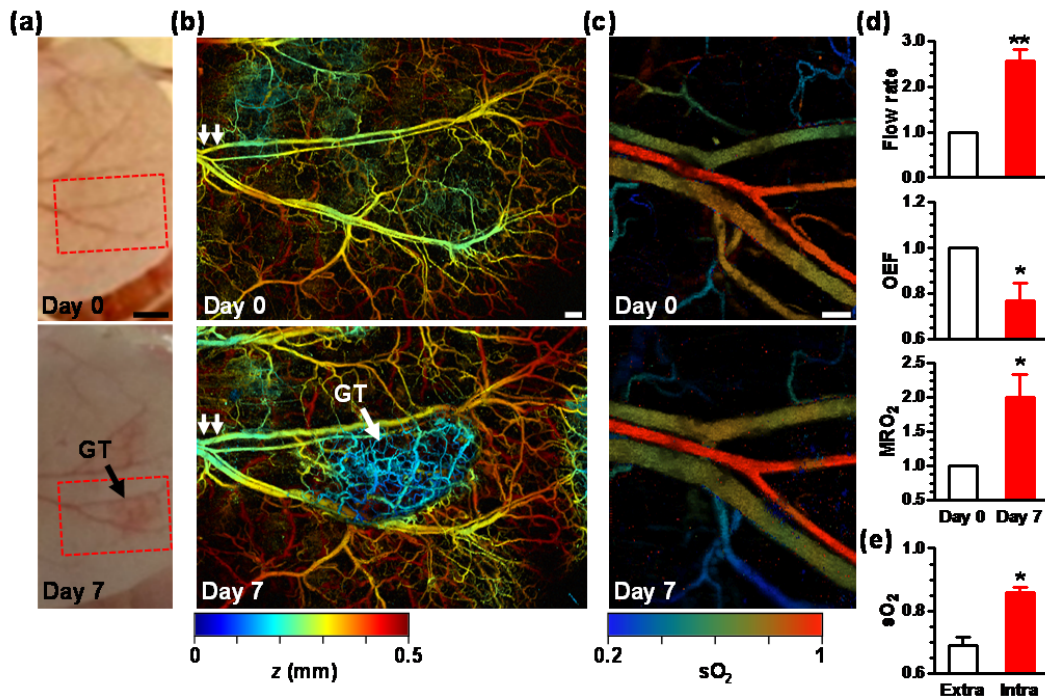


Figure 28. mPAM detection of early-stage glioblastoma by measuring metabolic rate of oxygen (MRO₂). (a) White-light photographs of a representative mouse ear before (day 0) and 7 days after the xenotransplantation of U87 glioblastoma tumor cells. Scale bar: 2 mm. (b) mPAM images of microvasculature in the tumor region [dashed boxes in (a)] at 584 nm. z is coded by colors: blue (superficial) to red (deep). Scale bar: 250 μ m. (c) mPAM images of oxygen saturation (sO₂) in the artery-vein pair [double arrows in (b)] that supports the tumor region acquired on day 0 and day 7. Scale bar: 100 μ m. (d) mPAM quantification of volumetric blood flow rate, oxygen extraction fraction (OEF) and MRO₂ 7 days after the tumor xenotransplantation, normalized by the values of day 0 (flow rate: 1.03 ± 0.41 μ l/min; OEF: 0.27 ± 0.03 ; MRO₂: 0.31 ± 0.09 ml/100 g/min). (e) Comparison of the averaged sO₂ values in the intra- and extra-tumoral vasculatures. Statistics: paired Student's t -test. * $p < 0.05$, ** $p < 0.01$, $n = 5$. Data are presented as means \pm s.e.m. GT: glioblastoma tumor.

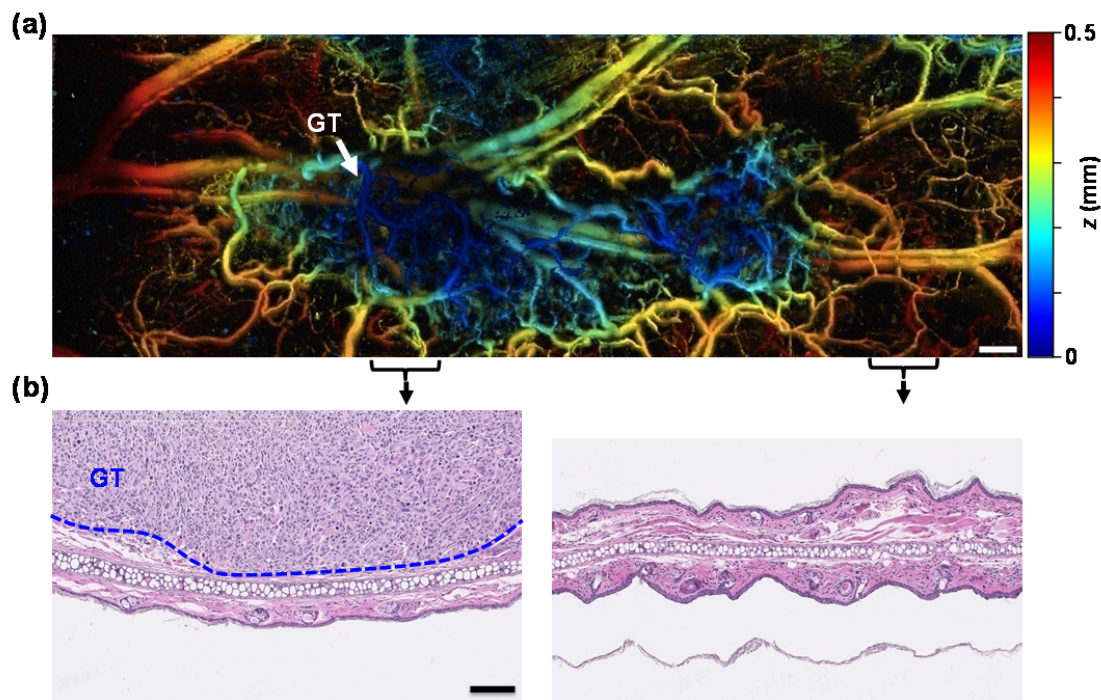


Figure 29. Histological validation of glioblastoma detection. (a) mPAM image of a mouse ear bearing a U87 glioblastoma tumor acquired on day 7. z is coded by colors: blue (superficial) to red (deep). Scale bar: 250 μm . (b) Images of H&E stained tissue slices cut approximately across the tumor area (left) and non-tumor area (right). Scale bar: 150 μm . GT: glioblastoma tumor.

3.4.3. Conclusions and discussion

The observations presented here demonstrate the power of mPAM as the only noninvasive label-free imaging modality that can measure all the parameters required for the quantification of MRO_2 in absolute units. Whereas MRO_2 is the ultimate measure of oxygen metabolism, OEF and sO_2 can be misleading partial measures. Unlike commonly believed, a decrease in OEF or an increase in sO_2 does not necessarily indicate a decrease in MRO_2 . Strikingly, we found early-stage cancer to be hyperoxic instead of hypoxic despite the hypermetabolism.

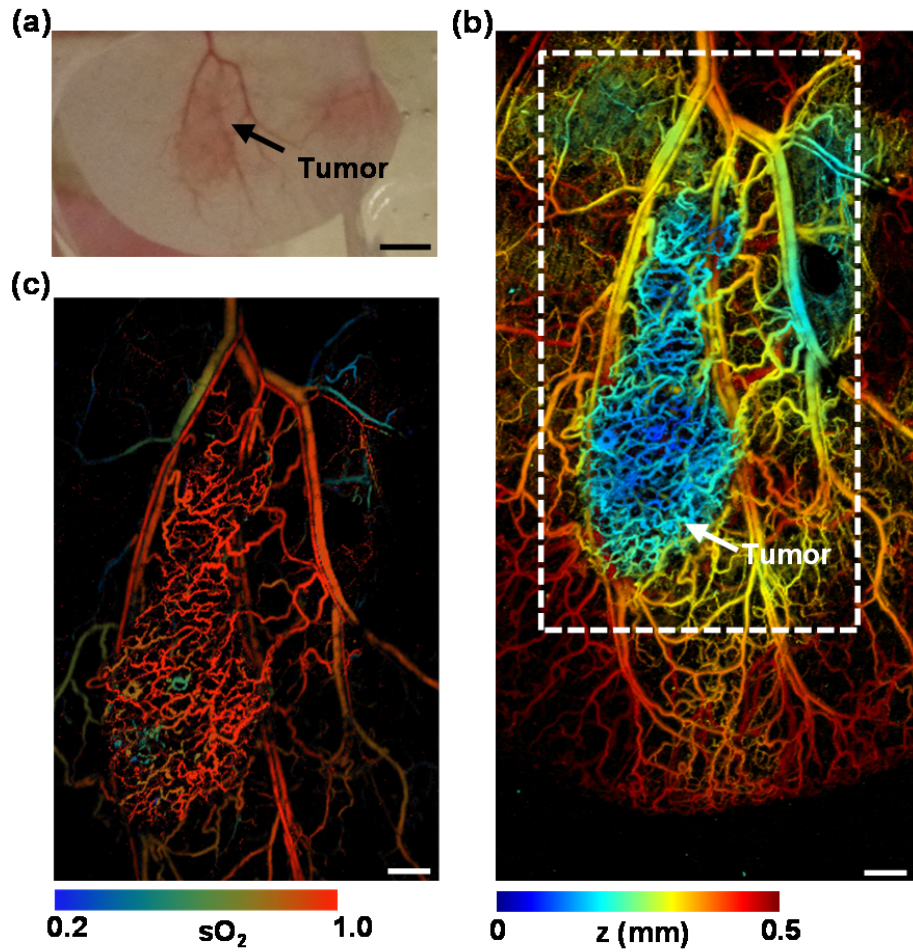


Figure 30. Label-free mPAM of hypermetabolism and hyperoxia of early stage cancer. (a) Photograph of a mouse ear bearing a xenografted glioblastoma on Day 7. Scale bar: 2 mm. (b) mPAM image of the vasculature of the mouse ear. The depth is color coded: blue (superficial) to red (deep). Scale bar: 200 μm . (c) mPAM image of the sO_2 of the tumor region in (b). It is clearly shown that the tumor region was hyperoxic. Scale bar: 200 μm .

mPAM can non-invasively measure anatomical, functional, and fluid-dynamic information at the resolution of small vessels, making it possible for MRO_2 quantification in microenvironments. MRO_2 -based early cancer detection and evaluation of its treatment are highly desirable. mPAM has also various other prospective applications related to MRO_2 . First, its high spatial resolution is essential for micro-hemodynamic studies, such as monitoring of local hemorrhage caused by mini-strokes. Second, its high sensitivity is critical for studies concerning small metabolic

changes, such as monitoring of neuro-vascular coupling in response to physiological challenges. Third, its potentially real-time imaging through fast optical scanning or ultrasonic-array detection is important for studies involving short transition times between physiological states, e.g., monitoring of epileptic seizures. Finally, its high spatial scalability enables us to correlate microscopic and macroscopic studies—e.g., monitoring of local neuron firing and overall brain activity—based on the same contrast. Overall, mPAM has strong potential for the study of metabolism in cancer and other metabolic diseases.

4. Improvements in photoacoustic microscopy

While AR-PAM has achieved so far tens of micrometers resolution with a penetration depth up to 3 mm in tissue [33], OR-PAM focuses on superficial imaging (up to ~1 mm in tissue) with at least capillary level resolution [7]. Recently, the imaging performance of OR-PAM has been significantly improved in terms of spatial resolution and imaging speed. By using a water-immersion optical objective with a 1.23 numerical aperture (NA), a 220 nm lateral resolution at 532 nm wavelength has been achieved [130]. Meanwhile, by using a fast voice-coil scanner, the sectional imaging speed of OR-PAM has been pushed to 40 Hz over a 1 mm scanning range [131]. To further expand the coverage of OR-PAM and push its commercialization, numerous efforts have been invested to improve its performances. Here, we are going to describe two aspects of the improvements of OR-PAM, including extending its imaging depth by double illumination and speeding up its imaging speed by using a fast scanning MEMS mirror.

4.1. Double illumination photoacoustic microscopy

So far, the penetration depth of OR-PAM is still restricted to one transport mean free path due to the strong optical scattering in tissue. Moreover, the strong absorption of hemoglobin in the

visible spectral range further reduces the $1/e$ penetration depth to less than 50 μm in blood vessels, which may cause shallower vessels to shadow deeper vessels. This penetration limitation applies to both reflection-mode and transmission-mode OR-PAM. Only a layer of tissue on the optical illumination can be imaged [32, 36, 130, 132]. By illuminating light from both the top and bottom sides of the sample, we have developed a double-illumination PAM (DI-PAM) to improve the penetration depth to ~ 2 mm in thin biological tissue. At the same time, the optical focal zone is expanded to ~ 260 μm .

4.1.1. Methods

In DI-PAM (Figure 1), a Nd:YVO₄ laser (Elforlight, SPOT) generates 1.5 ns pulses at a 532 nm wavelength. The pulses are reshaped by an iris (ID25SS, Thorlabs) and attenuated by a neutral density filter (NDC-50C-2M, Thorlabs). The attenuated beam is then split into two sub-beams (top and bottom) by a 50/50 beam splitter (BSW04, Thorlabs). The top beam is focused by a condenser lens (LA1131, Thorlabs) before passing through a 50 μm pinhole (P50C, Thorlabs) for further spatial filtering. The filtered beam is then focused by an optical objective (AC127-050-A, Thorlabs. NA: 0.1 in air) into the sample from the top. A beam combiner composed of a thin layer of silicone oil sandwiched by a right-angle prism (NT32-545, EdmundOptics) and a rhomboid prism (NT49-419, EdmundOptics) provides acoustic-optical coaxial alignment. The resultant photoacoustic waves are detected by an ultrasonic transducer (V214-BB-RM, Olympus-NDT) with a central frequency of 50 MHz. An acoustic lens with an NA of 0.5 is ground into the bottom of the rhomboid prism to provide an acoustic focal diameter of 30 μm . An optical correction lens is attached to the top of the beam combiner to correct the aberration. The acoustic lens is submerged in a water-tank for ultrasound coupling. The bottom beam duplicates the same

path as the top beam, except that it is directly focused into the sample from the bottom without going through the beam combiner and water tank.

As shown in the inset of Fig. 31, by carefully adjusting the positions of two objectives, we achieved a co-axial configuration of the two optical foci and the acoustic focus. To best expand the optical focal zone, the top and bottom optical foci are both approximately one Rayleigh range apart from the acoustic focus. Volumetric imaging is acquired by two-dimensional raster scanning of the sample. While the lateral resolution is defined by the optical focus, the depth resolution is determined by the temporal resolution of the acoustic detection. An eyepiece is added to the bottom beam path to view the imaging region through the reverse path of the illumination. A photodiode is also added to monitor the fluctuations of the laser pulse intensity.

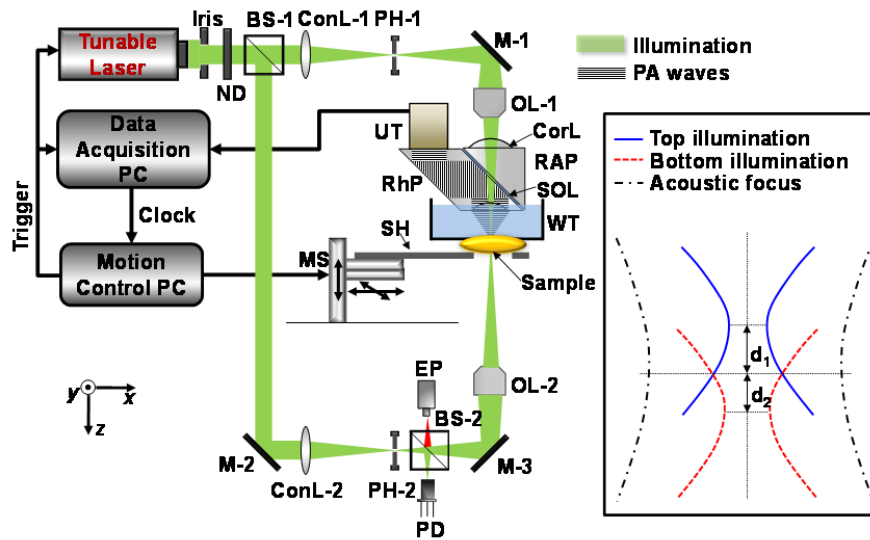


Figure 31. . Schematic of DI-PAM. $d_{1,2}$; Rayleigh range. ND, neutral density filter; BS, beam-splitter; ConL, condenser lens; PH, pinhole; M, mirror; OL, objective lens; CorL, correction lens; RAP, right-angle prism; SOL, silicone oil layer; RhP, rhomboid prism; UT, ultrasonic transducer; WT, water tank; SH, sample holder; MS, motor scanner; EP, eyepiece; PD, photodiode.

4.1.2. Results

Phantom study

To measure the lateral resolution of the DI-PAM system, a sharp ink edge was imaged in water at varied depths while the optical focus was fixed. From the edge spread function, the full width half maximum of the line spread function was computed to determine the lateral resolution. As a comparison, the lateral resolution under either top or bottom illumination was also quantified using the same protocol. The measured results were fitted using the theoretical model for a Gaussian beam $w(z) = \sqrt{w_0^2 + [\frac{\lambda(z-z_0)}{\pi w_0}]^2}$, where $w(z)$ is the lateral resolution at depth z , w_0 is the focal diameter, λ is the wavelength and z_0 is the focal depth. While λ is known, w_0 and z_0 are the unknown parameters to fit for. As shown in Fig. 32a, the top illumination gives a focal diameter of 2.3 μm with a focal zone of 100 μm . Here, focal zone is defined as the range of depths over which the system maintains a lateral resolution no worse than $\sqrt{2}w_0$. Similarly, the bottom illumination gives a focal diameter of 2.9 μm , with a focal zone of 170 μm . The two foci are 160 μm apart. The top illumination has a tighter focusing due to the addition of the correction lens which gives an effective NA of 0.133 in water, while the bottom illumination has an NA of 0.1 in air. As can be seen in Fig. 32b, under double illumination, the lateral resolution has a ‘W’ shape distribution along the depth, which is determined by the overall light intensity of the two beams. The two valleys of the ‘W’ distribution are 2.3 μm and 2.9 μm in lateral resolution, which equal to the top and bottom focal diameters, respectively. The effective focal zone is expanded to 260 μm , which is the sum of the focal zones of the two valleys (100 μm and 160 μm , respectively). Thus, by increasing the focal zone by 160 μm over the top illumination or 90 μm over the bottom illumination, DI-PAM maintains the lateral resolution over a longer depth range.

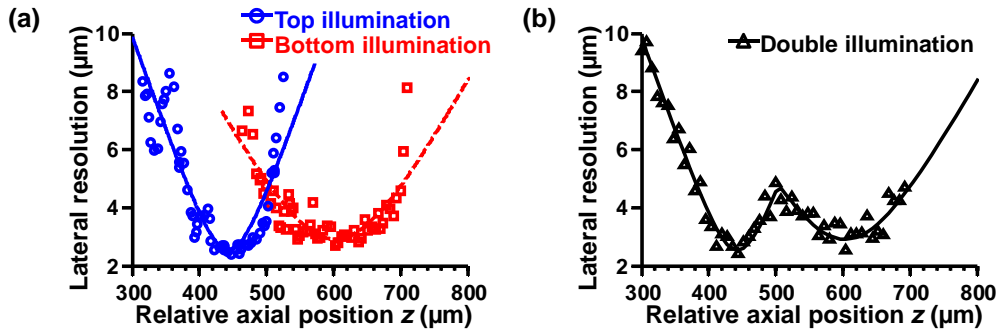


Figure 32. Lateral resolution as a function of the axial position relative to the starting depth of data-acquisition, under top, bottom and double illumination illuminations, respectively. Solid curves: theoretical fitting.

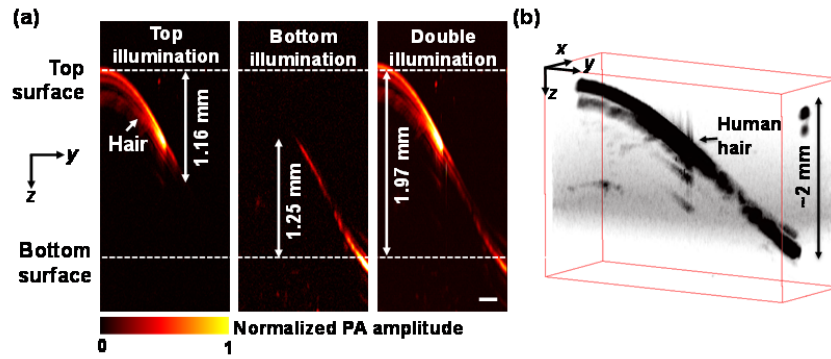


Figure 33. Penetration depth of double-illumination PAM. (a) Side-view DI-PAM images of the human hair inside the chicken tissue under three illuminations. Scale bar: 200 μm. (b) Volumetric rendering of the human hair imaged by DI-PAM.

To measure the penetration depth of the DI-PAM system, a black human hair was obliquely embedded in a 2-mm-thick piece of fresh chicken breast tissue. The two ends of the hair tightly pressed against the top and bottom surfaces of the tissue, and served as landmarks of the tissue boundaries. The top and bottom illuminations both had a pulse energy of 80 nJ. As shown in Fig. 33a, while either single illumination can image only the top (1.16 mm) or bottom (1.25 mm) part of the hair, DI-PAM can clearly image the whole hair Fig. 33b, demonstrating a penetration depth of at least ~2 mm in biological tissue.

Animal study

The improved system performance enables DI-PAM to image deeper vasculature while maintaining capillary level lateral resolution. The mouse ear was chosen for a first demonstration. The ear of a 12-week-old nude mouse (Hsd:Athymic Nude-Foxn1NU, Harlan) is composed of a layer of auricular cartilage sandwiched by two layers of skin tissue (Fig. 34d). The ear of our experimental mouse became much thicker seven days after the injection of $\sim 10^6$ U87 glioblastoma cells (Fig. 34c). A $10 \times 15 \text{ mm}^2$ area including the tumor region was sequentially imaged under top, bottom and double illuminations. In Fig. 34a, the depth-encoded maximum amplitude projection (MAP) images show that only the top layer vessels (shown in green) or bottom layer vessels (shown in red) can be well imaged under top or bottom illumination, respectively. Optical shadowing is the key reason. Although some big vessels from the other layer are discernable, they are very much blurred due to the degraded lateral resolution. In contrast, DI-PAM can clearly image both layers of vasculature without shadowing or blurring. The side-view MAP images in Fig. 34b further demonstrate the improvements of DI-PAM in penetration depth and focal zone, imaging through the whole ear with a thickness more than 1 mm.

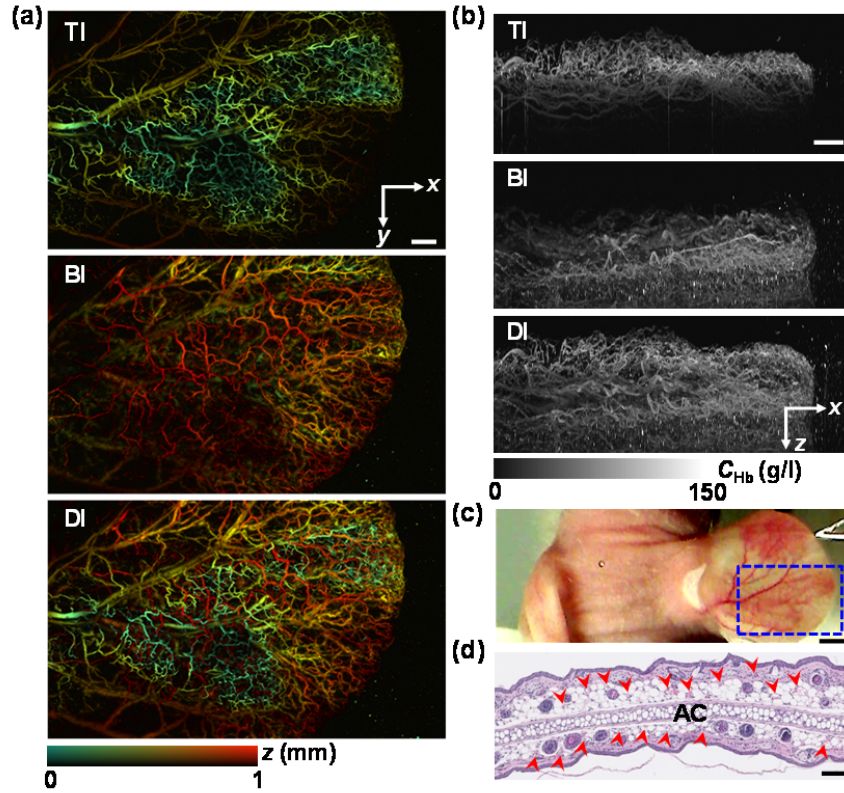


Figure 34. DI-PAM of mouse ear in vivo. (a) Top-view depth-encoded DI-PAM images of the right ear of a nude mouse bearing a U87 glioblastoma tumor, under top (TI), bottom (BI) and double (DI) illuminations, respectively. z is coded from green (superficial) to red (deep). Scale bar: 500 μm . (b) Side-view DI-PAM images under three illuminations. C_{Hb} , total hemoglobin concentration. Scale bar: 500 μm . (c) Photograph of the mouse ear. The imaged area is indicated by the blue dashed box. Scale bar: 2 mm. (d) Histology image of H&E stained tissue slice across the mouse ear. AC; auricular cartilage. Arrowheads; blood vessels. Scale bar: 100 μm .

In a second demonstration of DI-PAM, we imaged the vascular network surrounding the small intestine of a living black mouse (C57BL/6Hsd, Harlan), which is of interest in embryonic development and sepsis studies [133, 134]. After surgical exposure, part of the small intestine was gently pulled out and placed on the sample holder for DI-PAM imaging. The high vessel density on one side of the intestine would prevent imaging the other side by single-illumination PAM systems (Fig. 35e-f). In contrast, DI-PAM can obtain complete cross-sectional images of the intestine that is close to 2 mm in diameter (Fig. 35a-b). The depth-encoded MAP image shows a dense mesenteric vascular network, where the vessels from the top side were colored in

green and those from bottom side in red (Fig. 35a). The side-view MAP image of the section indicated by the dashed box in Fig. 35a appears to be a closed loop (Fig. 35b). The villi on the lumen of the intestine are also clearly resolved (Fig. 35c).

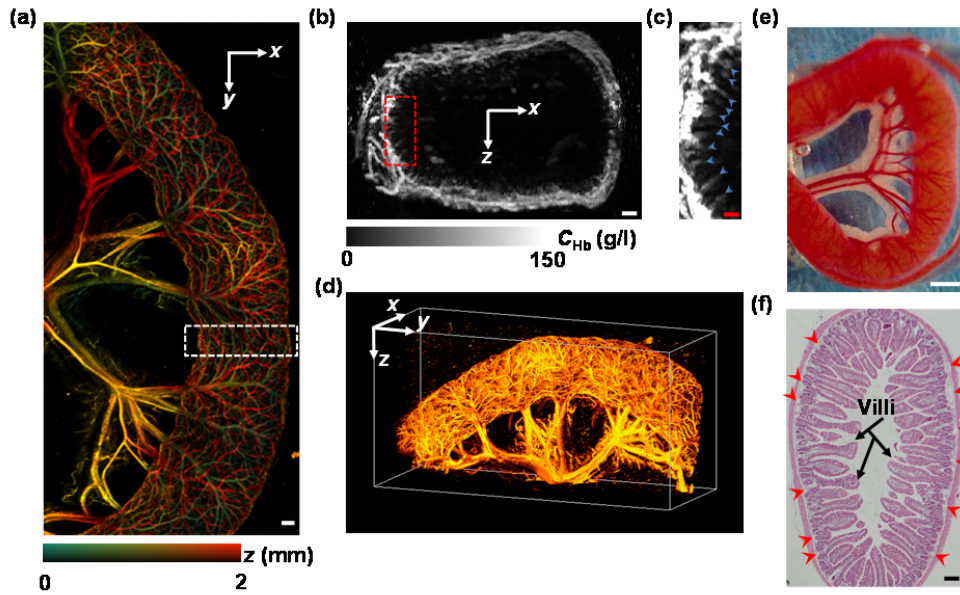


Figure 35. DI-PAM of the small intestine of a C57BL/6 mouse in vivo. (a) Top-view depth-encoded DI-PAM image of the small intestine under double illumination. Scale bar: 500 μm . (b) Side-view DI-PAM image of the region indicated by the dashed box in (a). C_{Hb} , total hemoglobin concentration. Scale bar: 250 μm . (c) Close-up of the small region indicated by the dashed box in (b). The intestinal villi are indicated by the arrowheads. Scale bar: 100 μm . (d) Volumetric rendering of the small intestine imaged by DI-PAM. (e) Photograph of the small intestine after surgical exposure. Scale bar: 1 mm. (f) Histology image of H&E stained cross-section of the small intestine. Arrowheads; blood vessels. Scale bar: 200 μm .

4.1.3. Conclusions and discussion

In conclusion, we have developed double-illumination PAM, which offers improved penetration depth and expanded focal zone. Compared with traditional reflection or transmission mode OR-PAM, the penetration depth has been improved to at least 2 mm in biological tissue. In addition, the focal zone has been improved to 260 μm , with a lateral resolution no worse than 4 μm . Deep microscopy of microvascular anatomy in a mouse ear and small intestine was performed. Although not demonstrated here, DI-PAM is intrinsically ready for label-free measurements of oxygen saturation, blood flow, and oxygen metabolism.

Simply doubling the incident light intensity for single illumination OR-PAM can also increase the penetration depth. However, the resultant improvement is not equivalent to that provided by DI-PAM. First, doubling incident light will not result in doubling of the penetration depth, since the attenuation of light by tissue is exponential rather than linear. Second, in DI-PAM, the light intensity on the tissue surface was 22 mJ/cm^2 for both top and bottom illuminations, which is still close to the American National Standards Institute (ANSI) safety limit (20 mJ/cm^2 in the visible spectral region). However, simply doubling the light intensity for single illumination (44 mJ/cm^2) will break the ANSI limit and thus increase the risk of damaging tissue.

The focal zone of single illumination OR-PAM can also be expanded by depth scanning and stacking the data sets together. However, this is not equivalent to the improvement due to DI-PAM. First, strong tissue scattering would degrade the lateral resolution as the focal position deepens. Second, the imaging time would be increased by depth scanning. In contrast, DI-PAM expands the focal zone without sacrificing lateral resolution and imaging speed.

4.2. MEMS scanning mirror based fast scanning photoacoustic microscopy

As all living biological systems are dynamic, it is also important to develop fast-scanning OR-PAM systems. Several scanning mechanisms have been reported to push the imaging speed of OR-PAM. The first type is to optically scan the laser beam within the focal spot of the ultrasonic transducer [135, 136]. This mechanism, however, suffers from a limited scanning range of $\sim 100 \mu\text{m}$ and inhomogeneous detection sensitivity within the field of view (FOV) [135, 136]. The second method is to optically scan the laser beam within the detection area of an unfocused ultrasonic transducer [132, 135]. This method increases the scanning range to a few millimeters, while reducing the overall detection sensitivity by more than 40 dB. The third form is to mechanically scan by mounting the whole imaging head on a voice-coil scanner [137]. This

design can maintain the confocal alignment and increase the scanning range to a few millimeters, but over which the scanning speed can reach only ~ 40 Hz, limited by the mass of the imaging head. Different fast-scanning methods for PAM imaging are summarized in Table 1.

Table 1: Comparison of fast-scanning methods

Scanning methods	B-scan rate (Hz/mm)	Scanning range (mm)	SNR ^a	Transducer focusing	Detection homogeneity ^b	Ref
Mechanical scanning	1	>10	+++	Spherical	+++	[32]
Multifocal scanning (transducer array)	4	~ 5	++	Cylindrical	++	[138]
Hybrid scanning	24	~ 4	++	Cylindrical	++	[139]
Voice-coil scanning	40	>5	+++	Spherical	+++	[140]
2D optical scanning (unfocused transducer)	100	~ 6	+	Unfocused	+++	[132]
2D optical scanning (focused transducer)	180	<0.1	++	Spherical	+	[135]

^a More plus signs indicate better SNR.

^b More plus signs indicate better homogeneity of the acoustic detection over the scanning range.

Here, we present a wide-field fast-scanning OR-PAM by using a lab-made water-immersible MEMS (i.e., microelectromechanical system) scanning mirror (MEMS-OR-PAM). A cross-sectional (B-scan) imaging rate of 400 Hz over a 3 mm range has been achieved. By scanning both the excitation laser beam and resultant acoustic beam, MEMS-OR-PAM maintains confocal alignment and high detection sensitivity over a large FOV.

4.2.1. Methods

Fig. 36 is a schematic of the MEMS-OR-PAM. The light source is an Nd:YVO₄ laser (AOT-YVO-100Q, AOT Inc.) which generates 2 ns pulses at 532 nm with a repetition rate of 100 kHz. The laser beam is focused by a condenser lens (LA1131, Thorlabs) then spatially filtered by a

50- μm -diameter pinhole (P50C, Thorlabs). The filtered beam is focused by an optical objective lens (AC127-050-A, Thorlabs. NA: 0.1 in air). A beam combiner composed of an aluminum-coated prism (NT32-331, Edmund) and an uncoated prism (NT32-330, Edmund) provides acoustic-optical coaxial alignment. The thin aluminum coating provides optical reflection but acoustic transmission. The focused laser beam is directed towards the sample surface by the aluminum coating of the combiner and a MEMS scanning mirror plate. An optical correction lens attached to the top surface of the combiner corrects the aberration due to the prism. The resultant photoacoustic waves are reflected by the MEMS scanning mirror and detected by an ultrasonic transducer (V214-BB-RM, Olympus-NDT), which has a central frequency of 50 MHz and a -6 dB bandwidth of 66%. An acoustic lens with an NA of 0.25 (NT45-010, Edmund) is attached to the right surface of the combiner and provides an acoustic focal spot size of $\sim 80\text{ }\mu\text{m}$ in water. The acoustic NA of this system is chosen to be $\sim 50\%$ less than that of previously reported OR-PAM systems because fitting the MEMS scanning mirror requires a longer working distance. The whole imaging head is submerged in a water tank for ultrasound coupling. Volumetric imaging is provided by fast angular scanning of the MEMS scanning mirror along the x -axis and step motor scanning of the sample along the y -axis.

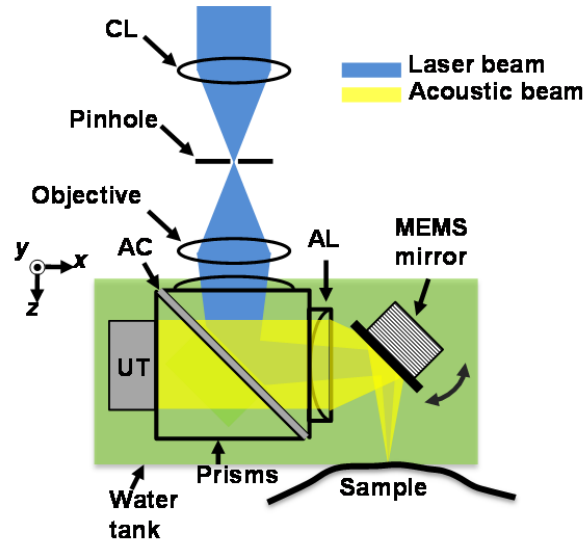


Figure 36. Schematic of MEMS-OR-PAM. CL, condenser lens; AC, aluminum coating; AL, acoustic lens; UT, ultrasonic transducer.

As shown in Fig. 37, the MEMS mirror plate is made of silicon with a gold coating, thus provides a good condition for reflecting both the optical and acoustic beams. The mirror plate is supported by two hinges made of high-strength flexible polymer materials, which can resist surface tension forces in liquids. To actuate the mirror, high efficient electromagnetic force is generated by a compact inductor coil and a pair of high-strength rare-earth permanent magnets on the back of the mirror plate. A sinusoidal current applied to the inductor coil generates a magnetic field with alternating polarity and strength, which drives the mirror plate to oscillate around the hinges. By controlling the frequency and amplitude of the driving voltage, the scanning speed and range can be adjusted appropriately.

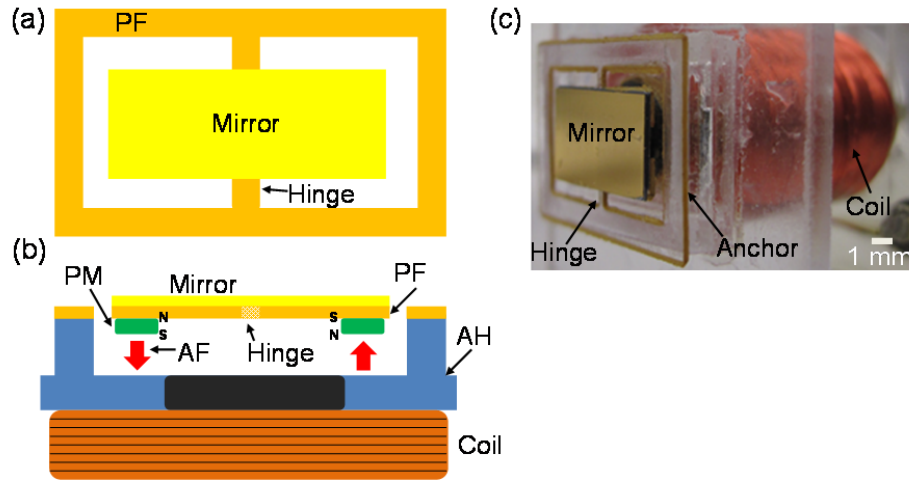


Figure 37. MEMS-scanning mirror. (a-b) Schematics of the top (a) and side (b) views of the water-immersible MEMS scanning mirror. (c) Photograph of a fabricated prototype device. The silicon mirror plate was coated with a thin gold layer. PF, polymer frame; PM, permanent magnet; AF, actuation force; AH, acrylic holder.

4.2.2. Results

Phantom study

To measure the lateral resolution of the MEMS-OR-PAM system, the edge of a sharp blade was imaged in water. From the edge spread function, the full width at half maximum of the line spread function is estimated to be $2.4\ \mu\text{m}$, which is close to the theoretical, diffraction-limited focal spot size of the laser beam ($2.1\ \mu\text{m}$) (Fig. 38). The optical focal zone is about $154\ \mu\text{m}$, in which the lateral resolution is within $5\ \mu\text{m}$. The axial resolution was estimated to be $\sim 40\ \mu\text{m}$ based on the transducer bandwidth and the speed of sound in tissue. Both the lateral and the axial resolutions decrease with imaging depth due to increasing optical scattering and frequency-dependent acoustic attenuation in tissue, respectively.

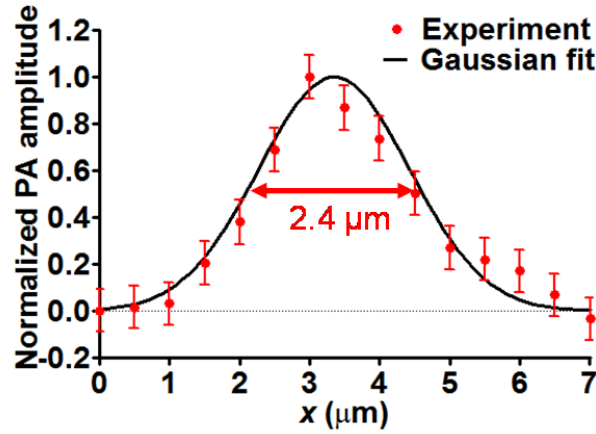


Figure 38. Line spread function used to measure the lateral resolution of the system (red circles, the averaged pixel values; blue line, the Gaussian fit).

The maximum penetration depth of the MEMS-OR-PAM was experimentally quantified by obliquely inserting a 250- μm -diameter black needle into the leg of an anesthetized nude mouse. As shown in Fig. 39, after time-gain compensation for the optical and acoustic attenuation, the system can clearly image the needle down to 1.1 mm beneath the skin surface, which is comparable to other OR-PAM systems.[36, 137]

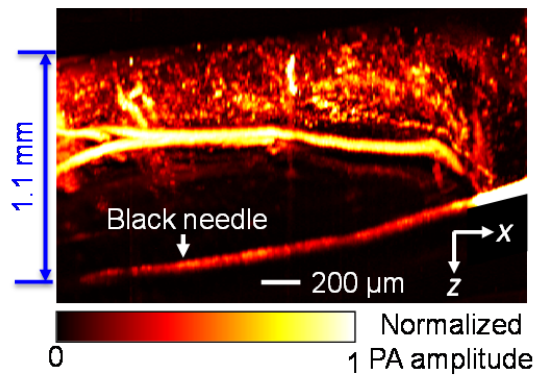


Figure 39. MEMS-OR-PAM image of a black needle inserted obliquely into the leg of a living mouse. A 1.1 mm *in vivo* imaging depth was achieved with time-gain compensation.

Different from the linear scanning of traditional OR-PAM systems [32, 36, 137], the angular scanning of MEMS-OR-PAM results in a curved focal plane with a radius of 7 mm. The maximum in-focus scanning range is ~ 3.0 mm along the x -axis. Since raw B-scan images are in the polar coordinates (Fig. 40a), we converted the data to Cartesian coordinates considering the scanning geometry and applying a 2D linear interpolation (Fig. 40b). For a uniform black-tape target, the averaged PA signal amplitude varies less than 5% along the x -axis (Fig. 40b). The result demonstrates that MEMS-OR-PAM maintains uniform detection sensitivity along the scanning direction, superior to other fast scanning methods where the confocality is compromised.

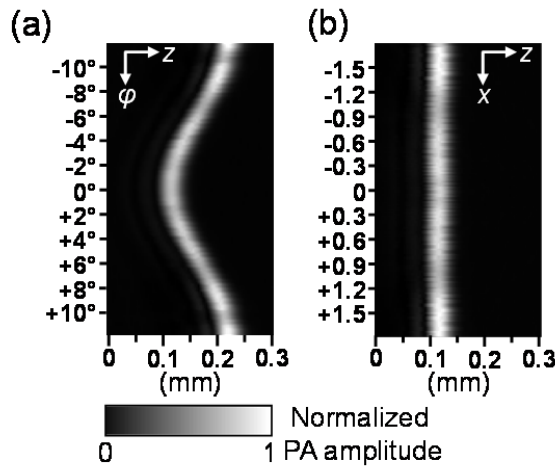


Figure 40. Scanning trace correction of MEMS-OR-PAM. (a) Raw B-scan image of a piece of flat black-tape in polar coordinates. The angular scanning of the MEMS mirror introduced the curvature of the imaged target surface. ϕ , scanning angle of the MEMS mirror. (b) B-scan image in Cartesian coordinates converted based on the scanning geometry and 2D linear interpolation.

Animal study

Red blood cell (RBC) flow in a nude mouse ear was imaged *in vivo* by MEMS-OR-PAM to demonstrate its high-speed imaging capability. All experimental animal procedures were carried

out in conformity with the laboratory animal protocol approved by the Animal Studies Committee at Washington University in St. Louis. As shown in Fig. 41, a $2 \times 5 \text{ mm}^2$ area of the mouse ear was repeatedly scanned with a volumetric imaging speed of 0.8 Hz (a 2D B-scan rate of 400 Hz), which is about 400 times faster than the second-generation OR-PAM system and 20 times faster than the most recent voice-coil based OR-PAM scanner for the same scanning range [36, 137]. The laser pulse energy on the skin surface was measured to be 100 nJ. Since 532 nm is close to the isosbestic wavelength, the PA signal amplitude reflects the total hemoglobin concentration regardless of the oxygenation of hemoglobin. The spatial resolution is sufficient for resolving the capillary beds (Fig. 41), and the imaging speed enables the mapping of the RBC movements in small vessels. The average signal to noise ratio (SNR) is 36.5 dB, which is about 6 dB less than that of the second-generation OR-PAM system, due to the smaller NA of the employed acoustic lens [36]. Nevertheless, this SNR is adequate for single RBC imaging [36, 137].

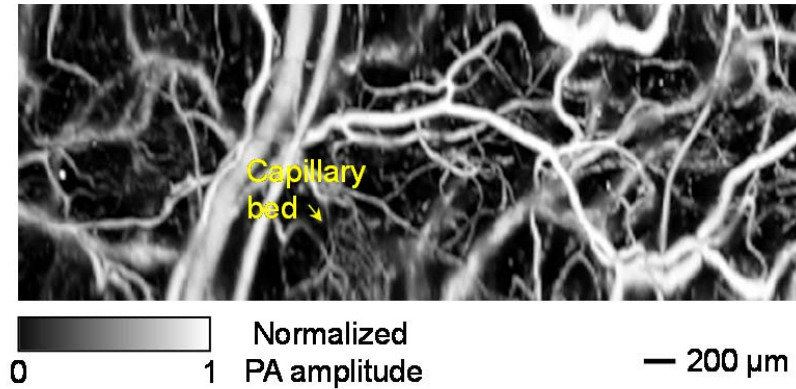


Figure 41. MEMS-OR-PAM of blood flow dynamics of the vasculature in a mouse ear. Capillaries were clearly resolved, and the flow dynamics over a $2 \times 5 \text{ mm}^2$ area were imaged with a 0.8 Hz volumetric frame rate and 400 Hz B-scan rate.

In addition to the RBC flow imaging based on endogenous contrast, intravascular transport of an exogenous contrast agent was also explored using the system. First, we imaged a $0.6 \times 2 \text{ mm}^2$ area of a nude mouse ear as a control with laser pulse energy of 100 nJ (Fig. 42a). Then, we injected carbon particles with $\sim 6 \text{ }\mu\text{m}$ diameters (2.5% w/v, carbon glassy spherical powder, Sigma-Aldrich) into the blood stream of the nude mouse via its tail vein. A $0.3 \times 1 \text{ mm}^2$ area which contained a 40- μm -diameter vein was chosen as the region of interest (ROI) for dynamic imaging. The ROI was repeatedly imaged with a volumetric frame rate of 4 Hz. Lower pulse energy of 10 nJ was used to image only the particles, which are much more absorbing than hemoglobin. As shown in Fig. 42b, the average flow speed of the particles in the vein was much slower than the RBC flow [80]. This is likely due to the larger mass density of the particles (1.46 g/cm^3).

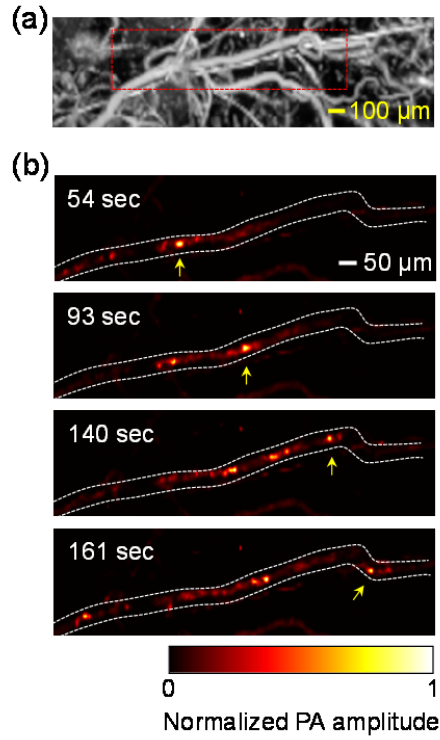


Figure 42. MEMS-OR-PAM of flow dynamics of carbon particles. (a) MEMS-OR-PAM image of a mouse ear with a pulse energy of 100 nJ, where the blood vessels were imaged. (b) After the injection of carbon particles via the tail vein, a smaller region indicated by the dashed box in (a) was monitored with a 4 Hz volumetric frame rate. The pulse energy was reduced to 10 nJ to image only the particles. The dashed lines are the boundaries of the vessel containing the flowing particles. A representative particle is indicated by the arrows.

4.2.3. Conclusions and discussion

In summary, we have developed MEMS-OR-PAM that can dramatically improve the imaging speed while maintaining the confocal alignment of the optical and acoustic beams over a wide FOV. Conserving the high spatial resolution and imaging sensitivity of traditional OR-PAM systems, we achieved a B-scan imaging speed of 400 Hz over a 3 mm scanning range, currently limited by the repetition rate of the employed laser system. The scanning range can be traded off for imaging speed. A laser system with higher repetition rate or an intensity-modulated continuous wave laser can further improve the imaging speed. By employing a dual-wavelength

laser source, MEMS-OR-PAM is intrinsically capable of label-free measurements of oxygen saturation and oxygen metabolism [39].

PAM can also improve its imaging speed through parallel acoustic detection by ultrasound transducer arrays. In a multi-focal OR-PAM system, twenty diffraction-limited focal spots are simultaneously excited, and the resultant PA signals are detected by a 48-element ultrasound linear array [138]. Limited by the 6:1 multiplexing in data acquisition, the imaging speed is eventually improved by three to four times, compared with that in conventional single-focus and single-detector OR-PAM. However, this method needs twentyfold more laser energy than conventional OR-PAM. Besides, because of the inverse reconstruction of PA images, reconstruction artifacts due to the limited detection aperture may degrade the image quality.

Currently, it is the laser repetition rate that limits the imaging speed in PAM. Theoretically, real-time (≥ 30 Hz) volumetric imaging over a $1 \times 1 \text{ mm}^2$ surface area needs a 5 MHz laser with a pulse energy of 100 nJ for OR-PAM, or a 50 kHz laser with a pulse energy of 100 μJ for AR-PAM. To avoid interference between PA waves excited by consecutive pulses, it is the acoustic flight time that limits the ultimate imaging speed. For example, to image a sample with a thickness of 1 mm, the minimum time interval between consecutive pulses should be 0.67 μs , which corresponds to a maximum laser repetition rate of 1.5 MHz.

5. Biomedical applications of multi-contrast photoacoustic microscopy (tomography)

By offering high-resolution images with unique optical contrast, PAM has so far been applied to numerous preclinical and human studies, including vascular biology [141-143], oncology [82, 100, 144-149], neurology [74, 150-152], ophthalmology [132, 153-156], dermatology [157-161], gastroenterology [162-166], and cardiology [35, 167-169]. Here, we are going to introduce several representative applications. Although photoacoustic computed tomography (PACT) is not the major topic of this dissertation study, its imaging speed is typically faster than PAM due

to the parallel acoustic detection by transducer array. Dynamic metabolism of mouse brain was imaged by PACT in combination with PAM and fluorescence study.

5.1. Immediate alterations in intestinal oxygen saturation and blood flow following massive small bowel resection as measured by photoacoustic microscopy

Short gut syndrome is a condition of high morbidity and mortality within the pediatric population and results primarily from massive intestinal loss. After a massive small bowel resection (SBR) in both animal models and humans, a critical adaptation response occurs within the remnant bowel and is characterized by significant increases in villus height and crypt depth, resulting in increased absorptive mucosal surface area to compensate for the attenuated bowel length [170-172]. Angiogenesis has long been recognized as important in states of cellular proliferation [173, 174]. The contribution of villus angiogenesis to intestinal adaptation has recently been demonstrated. Proangiogenic growth factor supplementation has been shown to enhance intestinal mucosal growth [175], and inhibition of vascular endothelial growth factor has resulted in a decreased adaptive response after intestinal loss [176]. Previous study has established an increased villus capillary density on postoperative day 7 in mice that have undergone massive SBR [177]. This is preceded on postoperative day 3 by an increase in the gene expression of proangiogenic chemokine ligand 5 [178]. The exact stimulus for these proangiogenic changes as well as the acute alterations in intestinal hemodynamics following SBR are presently unknown.

Previous ex vivo studies of intestinal blood flow at late time points after SBR are conflicting. Studies using intravascular injections of radioactive particles and measurement of radioactivity from harvested tissue as surrogate markers for blood flow have demonstrated increased blood

flow following SBR distal to the site of intestinal anastomosis as soon as twenty-four hours following resection, however, the duration of this hyperemic response has been variable [179-181]. In addition, these studies did not measure other parameters of hemodynamics, including oxygen saturation of hemoglobin (sO₂). No prior studies have measured hemodynamic parameters within the remnant gut immediately after bowel resection using an in vivo, real time imaging system with endogenous contrast.

To overcome the limitations of the imaging tools used in prior studies, we sought to determine the effect of SBR on intestinal hemodynamics using photoacoustic microscopy (PAM), a non-invasive, label-free, high-resolution hybrid imaging modality. With the help of PAM, a better understanding of the acute hemodynamic changes following SBR may further elucidate a mechanism for villus angiogenesis and the pathogenesis of intestinal adaptation.

5.1.1. Materials and methods

Experimental design

A protocol for this study was approved by the Washington University Animal Studies Committee (no 20090275) in accordance with the National Institute of Health laboratory animal care and use guidelines. Mice underwent either 50% proximal SBR (n=7) or sham (enterotomy alone) (n=7) procedure as previously described [170]. Photoacoustic microscopy measurements of the terminal mesenteric arteriole and accompanying vein vessel diameter, blood flow, and oxygen saturation were obtained at 6 cm proximal to the ileal-cecal junction (ICJ) and at 12 cm proximal to the ICJ on the serosal surface of the intestine both prior to and immediately following the procedure.

Male mice (C57BL/6; Harlan Laboratories, Inc.; Indianapolis, IN) age 8 to 15 weeks were used in this study. Mice were kept on a 12-hour light-dark cycle and housed in a standard facility. The mice were given free access to standard rodent food pellets and water up until the time of the procedure.

Operative technique

Mice underwent 50% proximal SBR or sham (enterotomy alone) as previously reported [170] with the exception that no reanastomosis was performed. Briefly, a midline laparotomy was made and the bowel was exposed for photoacoustic measurements. Mice that underwent SBR had transection of the bowel at 12 cm proximal to the ICJ and at 1 to 2 cm distal to the ligament of Treitz. The mesentery of the intervening bowel was ligated with a silk tie and the intervening bowel was removed. In mice that underwent the sham procedure, the bowel was transected only at 12 cm proximal to the ICJ.

Intestinal sO₂ and blood flow measured by photoacoustic microscopy

During the experiment, mice were anesthetized with isoflurane (E-Z Anesthesia, Euthanex) and placed in a supine position on a heating pad (37 °C). A midline laparotomy was performed and the entirety of the small bowel was exposed. The terminal mesenteric artery and accompanying vein at a point approximately 6 cm and 12 cm proximal to the ICJ were identified. Baseline sO₂ was measured at both locations on a $1 \times 4 \text{ mm}^2$ area containing such vessel pairs at two optical wavelengths of 532 nm and 560 nm using a previous published method [88]. Baseline blood flow speed measurement was then performed at both locations across the proximal end of the vessel in *M*-mode using a bandwidth broadening based method [80, 81]. The laser repetition rate was 10 kHz, and 4000 A-lines were acquired at each position. The area of the bowel not being measured was kept moistened with a normal saline soaked gauze pad. The animal then underwent SBR or

sham procedure. Following the procedure, the same artery and vein pairs at 6 cm and 12 cm proximal to the ICJ were imaged with sO₂ and blood flow measurements recorded. Following all measurements the animal was sacrificed via cervical dislocation.

Statistical analysis

All the photoacoustic data processing was conducted using MATLAB (R2008a, MathWorks). Quantitative values are presented as mean \pm SEM. An unpaired Student's *t*-test was used for comparisons between all measurements. A *p* value less than 0.05 was considered to be statistically significant. The Sigma Stat statistical package (SPSS, Chicago, IL) was used for all statistical analyses.

5.1.2. Results

A total of 7 mice underwent the SBR procedure with post-SBR measurements and 7 mice underwent the sham procedure with post-sham measurements. The presented pre-operative data (n=7) represents that of the SBR group only as variability in the pre-operative measurements amongst all animals was minimal. Only data from the measurements recorded at 6 cm proximal to the ICJ is presented as this mid-remnant bowel location best represents the hemodynamic changes throughout the entire remnant small bowel. In all cases the 6 cm measurement agreed with the trend from measurement at the 12 cm proximal to the ICJ location.

Arterial and venous oxygen saturation

Prior to SBR, arterial and venous oxygen saturations (%) were similar (0.98 ± 0.01 arterial pre vs 0.98 ± 0.02 venous pre at 6 cm, *p* value: 0.70). Immediately following SBR, the arterial oxygen saturation decreased (0.98 ± 0.01 pre vs 0.84 ± 0.06 post-SBR at 6 cm, *p* value: <0.05). This

trend towards decrease in arterial oxygen saturation was also observed following sham (0.98 ± 0.01 pre vs. 0.95 ± 0.01 post-sham at 6 cm, p value: 0.06; Fig. 43a).

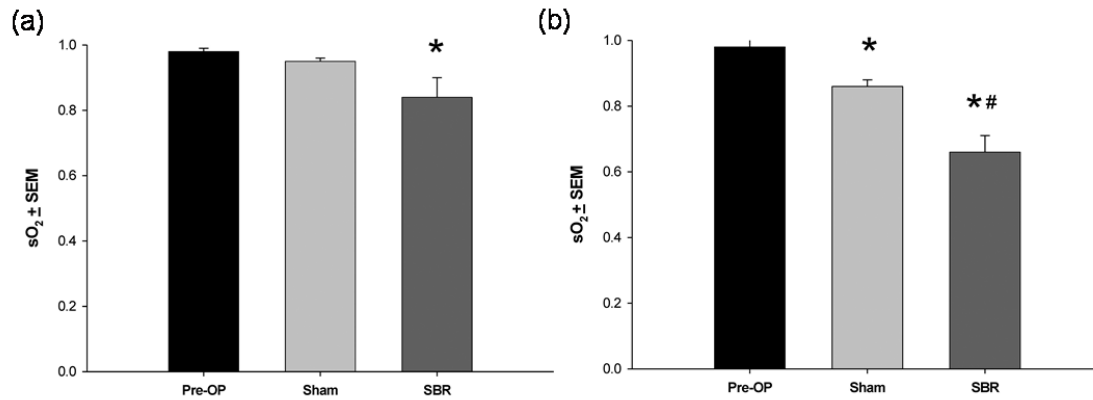


Figure 43. Oxygen saturation (sO_2) of the terminal mesenteric arteriole (a) and accompanying vein (b) pre-operatively, post-sham (bowel transection alone), and post-SBR at a location 6 cm from the ileal-cecal junction. Asterisk indicates $p < 0.05$ as compared to pre-op (pre-op vs sham and pre-op vs SBR). Number sign indicates $p < 0.05$ sham vs SBR.

Venous oxygen saturation dramatically decreased immediately following SBR (0.98 ± 0.02 pre vs 0.66 ± 0.05 post-SBR at 6 cm, p value: <0.001). This decrease in venous oxygen saturation was also observed to a lesser degree following sham (0.98 ± 0.02 pre vs 0.86 ± 0.02 post-sham at 6 cm, p value: < 0.001 , Fig. 43b). The difference between arterial and venous oxygen saturation post-SBR and post-sham was statistically significant, with the venous oxygen saturation decreasing to a greater extent than the arterial (p value: <0.05). The pronounced difference in arterial and venous oxygen saturation pre-op and post-SBR are demonstrated in Fig. 44.

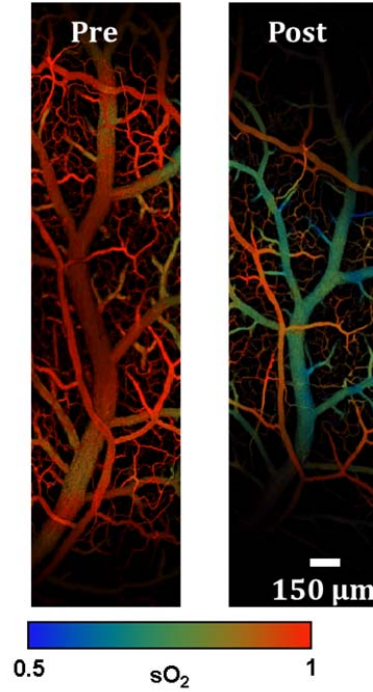


Figure 44. Photoacoustic microscopy images of intestinal microvascular structure and arterial and venous oxygen saturation (sO₂) pre-operatively and post-SBR.

Tissue oxygen extraction

Tissue oxygen extraction fraction (OEF) is defined as $(sO_2^{artery} - sO_2^{vein}) / sO_2^{artery}$ and represents the fraction of O₂ molecules that cross the capillary wall. We found that OEF dramatically increased post-SBR (0.01 ± 0.01 pre vs 0.21 ± 0.04 post-SBR at 6 cm, p value: < 0.001). OEF also increased post-sham (0.01 ± 0.01 pre vs 0.09 ± 0.02 post-sham at 6 cm, p value: < 0.05); however, the increase in OEF post-SBR was significantly greater than post-sham (0.21 ± 0.04 post-SBR vs 0.09 ± 0.02 post-sham, p value: < 0.05 , Fig. 45).

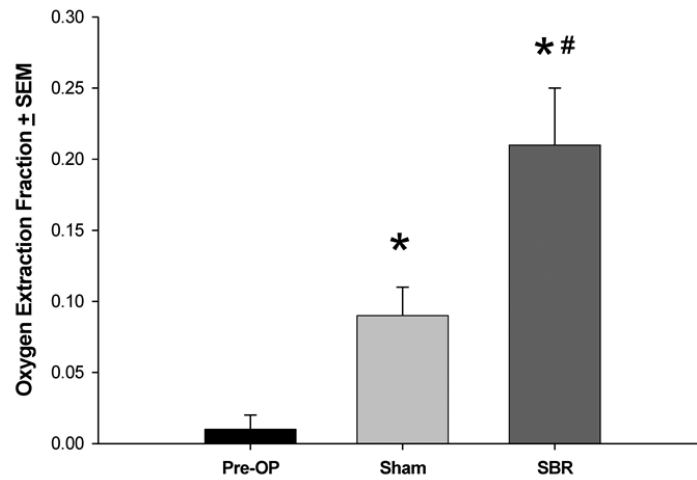


Figure 45. Tissue oxygen utilization pre-operatively, post-sham, and post-SBR at a location 6 cm from the ileal-cecal junction as calculated by the oxygen extraction fraction. Asterisk indicates $p < 0.05$ as compared to pre-op (pre-op vs sham and pre-op vs SBR). Number sign indicates $p < 0.05$ sham vs SBR.

Arterial and venous blood flow

Following SBR, the arterial blood flow decreased (7.6 ± 1.5 mm/s arterial pre vs 2.6 ± 0.55 mm/s post-SBR at 6 cm, p value: < 0.05). No change in arterial blood flow was observed in the sham group (7.6 ± 1.5 mm/s arterial pre vs 7.7 ± 0.6 mm/s post-sham, p value: 0.93) (Fig. 46a).

Venous blood flow also decreased following SBR (4.0 ± 0.7 mm/s venous pre vs 1.6 ± 0.5 mm/s venous post-SBR at 6 cm, p value: < 0.05). No change in venous blood flow was observed in the sham group (4.0 ± 0.7 mm/s venous pre vs 4.0 ± 0.5 mm/s venous post-sham, p value: 0.98) (Fig. 46b).

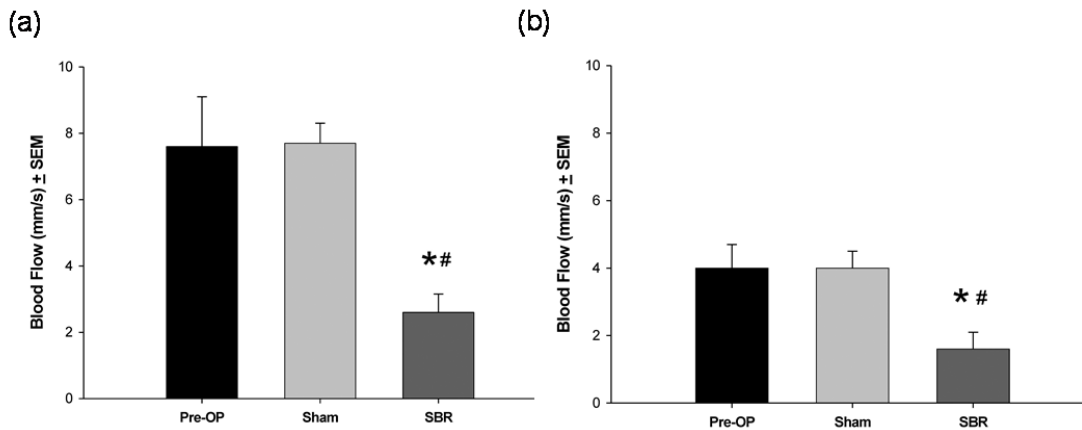


Figure 46. Blood flow (mm/second) of the terminal mesenteric arteriole (a) and accompanying vein (b) pre-operatively, post-sham, and post-SBR at a location 6 cm from the ileal-cecal junction. Asterisk indicates $p < 0.05$ as compared to pre-op (pre-op vs sham and pre-op vs SBR). Number sign indicates $p < 0.05$ sham vs SBR.

5.1.3. Conclusions and discussion

SBR results in villus angiogenesis and intestinal adaptation [177]. While previous studies have attempted to measure changes in blood flow following SBR using *ex vivo* methodologies and surrogate markers of blood flow, this is the first study to examine the effects of intestinal resection on hemodynamics using an *in vivo* imaging modality.

The present study demonstrates that PAM is a useful tool for measuring intestinal hemodynamics. The use of hemoglobin as endogenous contrast eliminates the potential disturbance to the intestinal system induced by exogenous contrast. High spatial resolution enables microenvironmental studies down to the level of the capillaries. The spatial resolutions of PAM can also be scaled for deeper tissue imaging [8]. Real-time imaging ability provides for acute response monitoring. In addition, the minimum invasiveness of PAM enables longitudinal studies on the same animal.

The results of the present study demonstrate that at baseline, prior to intervention, arterial and venous sO₂ of the terminal mesenteric artery and accompanying vein are similar. This may indicate minimal to no tissue oxygen utilization of the supplied intestine. Previous *ex vivo* studies of intestinal sO₂ using radioactive microspheres have demonstrated a significant difference between arterial and venous sO₂ in both the fasting and the fed state of other animal models. Stevenson and Weiss record in rats a 93.7% fasted arterial sO₂ in comparison to a 35.8% fasted venous sO₂; fed arterial and venous sO₂ were respectively similar. Other studies have demonstrated increased tissue oxygen uptake in piglets following oral feeds. In the present study, animals were not fasted prior to measurement, but given free access to standard rodent chow, making the timing of the animal's last meal a variable factor. However, given the minimal variability in the pre-operative measurements of both blood flow and oxygen saturation, this appears to have had minimal effect. While this contradicts previous *ex vivo* studies in other animal models, our *in vivo* results suggest either a high physiologic reserve in mice, and/or left-to-right shunting within the intestinal wall even with a metabolically active state.

Immediately following SBR, hemodynamic changes occur consistent with a reduced oxygen delivery. Venous sO₂ drops dramatically post-SBR. A less dramatic decrease in venous sO₂ also occurs post-sham, likely related to the metabolic effects of transection alone. It is unclear at this point in time the significance of the drop in arterial sO₂ post-SBR and post-sham. However, the overall oxygen extraction fraction post-SBR increases significantly, representing increased tissue oxygen utilization within the remnant bowel. Further, both arterial and venous blood flow decreased post-SBR. Such decrease in blood flow was not seen post-sham and likely represents an immediate reaction to ligation of 50% of the small bowel mesentery and vasculature, and not

a reaction to the acute blood loss from the transected marginal artery of the intestine that occurs both post-SBR and post-sham from the associated enterotomy.

Hypoxia is a well-recognized trigger of angiogenesis, resulting in the activation of hypoxia-inducible factors (HIF), responsible for transcriptional activation of genes [182]. In states of intestinal mucosal inflammation, HIFs have been shown to have a protective role. In a study by Karhausen et al, transgenic intestinal epithelial overexpression of HIF-1 protected against trinitrobenzene sulfuric acid-induced colitis, while loss of epithelial HIF-1 resulted in increased colitis severity, weight loss, intestinal permeability, and mortality [183]. It is plausible that cellular changes in response to hypoxia post-SBR may act in a similar manner, having a pro-angiogenic and protective role in the intestinal epithelium.

Previous studies of hemodynamic alterations following SBR have demonstrated a hyperemic response to SBR [179-181], however the earliest time point studied in those experiments was 24 hours after resection. In contrast, the data from this study represents changes of the intestinal microvasculature within the first hour post-SBR. It is unclear at this point in time the duration of the hypoxic changes that occur immediately after resection, but further investigation is underway to determine the changes in hemodynamics that occur as the bowel undergoes adaptation. Our laboratory's previous work has demonstrated an increased villus capillary blood vessel density within the remnant bowel on post-operative day 7 [177]. Such new blood vessel growth may be supported by increased blood flow as adaptation occurs.

Intestinal adaptation in response to massive SBR is a multifactorial process involving angiogenesis, cellular proliferation, and apoptosis. Through the use of photoacoustic microscopy, the immediate intestinal hemodynamic changes that occur after SBR, and resultant hypoxia, are

novel findings that provide possible mechanistic insight into the changes that occur within the remnant bowel within minutes of resection. The duration of intestinal hypoxia, cellular effects of such hypoxic changes, and impact on villus angiogenesis remain to be studied. A better understanding of hypoxia following SBR and the role of angiogenesis in intestinal adaptation may help in the development of future therapeutic treatments for patients with short gut syndrome.

5.2. Non-invasive photoacoustic tomography and microscopy of mouse brain metabolism *in vivo*

In mammals, the brain coherently controls the overall action of the body [184]. Performing numerous computation-intensive tasks such as information processing, perception, motor control and learning, brain tissue consumes a large amount of energy in proportion to its volume [185]. For example, humans devote 20-25% of their metabolism to the brain, where the energy is mostly used for sustaining the electric charge (membrane potential) of neurons [185, 186]. In humans and many other species, the brain gets most of its energy from oxygen-dependent metabolism of glucose [185]. An abnormal metabolic rate of glucose and/or oxygen usually reflects a diseased status of brain, such as cancer or Alzheimer's disease [187, 188]. In addition, physiologically active regions of the cerebral cortex consume more energy than inactive regions [189]. These phenomena have formed the basis for functional brain imaging methods, including positron emission tomography (PET) and functional magnetic resonance imaging (fMRI) [190, 191].

However, PET depends on the administration of radioactively-labeled tracers (e.g., 2-deoxy-2-fluoro-D-glucose, FDG), a complex procedure with exposure to ionizing radiation. fMRI is primarily sensitive to deoxy-hemoglobin and suffers from slow imaging speed. Moreover, both

PET and fMRI are expensive techniques with poor spatial resolutions. Therefore, a fast, noninvasive and non-ionizing imaging modality with good spatial resolutions is needed to advance metabolism-associated studies of brain physiology and pathology.

On the basis of the photoacoustic effect, photoacoustic tomography (PAT) solves the resolution drawback of pure optical imaging and the contrast drawback of pure ultrasonic imaging [5-7, 192]. In PAT, photon energy absorbed by molecules is partially or completely converted into heat, which thermoelastically induces pressure waves. The induced pressure waves are detected by ultrasonic detectors to form an image [192]. PAT is capable of anatomical, functional, molecular and metabolic imaging of small animals, with highly scalable spatial resolution and penetration depth [6, 7, 193, 194]. Photoacoustic computed tomography (PACT) is a major implementation of PAT, which aims at fast data acquisition, sub-millimeter resolution and deep penetration depth beyond the optical diffusion limit [26, 195-197]. Noninvasive, label-free and functional PACT of the rat brain was demonstrated by accurately mapping brain lesions and cerebral hemodynamics [26]. Molecular imaging of a mouse brain tumor *in vivo* was also performed with PACT, using IRI-800-c as the contrast agent [195].

Here, for the first time, we have demonstrated that PACT is able to image glucose uptake in the mouse brain, using a newly developed glucose analog 2-deoxy-2-[N-(7-nitrobenz-2-oxa-1,3-diazol-4-yl)amino]-D-glucopyranose (2-NBDG). To demonstrate the metabolic imaging capability of PACT, we studied *in vivo* forepaw stimulation responses. Our phantom and animal studies showed that PACT could spectrally separate 2-NBDG and blood using two-wavelength measurements, thus decouple the glucose and hemodynamic responses to the stimulations. Open-scalp photoacoustic microscopy and fluorescence imaging were used to validate the results from PACT.

5.2.1. Materials and methods

2-NBDG

2-NBDG is a newly developed fluorescent 2-deoxyglucose (2-DG) analog [192, 198-205]. Like the FDG (molecular weight: 181) used in PET studies, 2-NBDG is transported into cells via the same GLUT as glucose [204]. Once taken up by cells, 2-NBDG is phosphatized to 2-NBDG-6-P, which prevents it from being released again from the cells. However, because of the lack of the 2-hydroxyl group needed for glycolysis, 2-NBDG-6-P cannot be further metabolized. Therefore, the distribution of trapped 2-NBDG is a good reflection of glucose metabolism [203]. Because 2-NBDG is a relatively small molecule (molecular weight: 342) (Fig. 1a), it crosses the blood-brain-barrier much more easily than other near-infrared fluorophore-labeled 2-DG analogs, such as IRDye800-DG (molecular weight: 1330) [192, 199]. Moreover, 2-NBDG has its peak absorption at 478 nm, where hemoglobin has a much lower absorption [Figure 1b]. By carefully controlling the laser fluence, the signal contribution from hemoglobin can be neglected at this wavelength. These features have made 2-NBDG particularly suitable for brain studies.

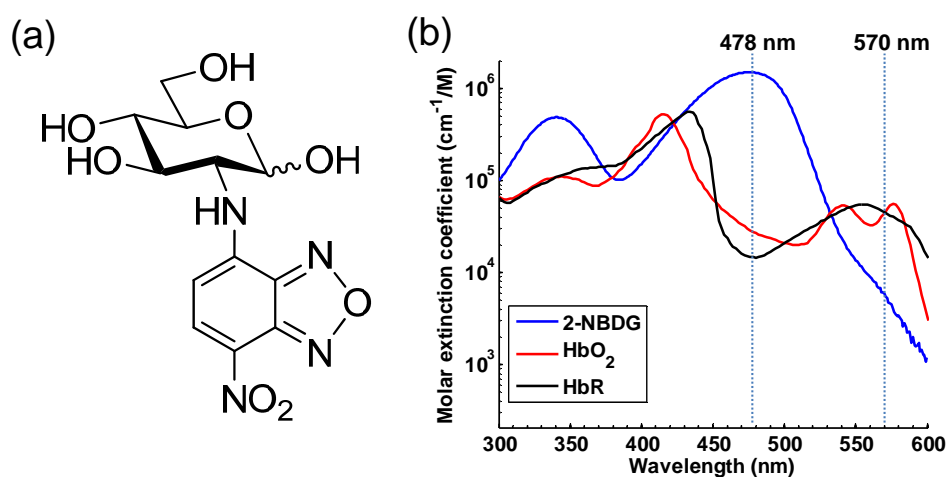


Figure 47. 2-NBDG (C₁₂H₁₄N₄O₈). (a) Chemical structure. (b) Molar extinction spectra of 2-NBDG, deoxy- and oxy-hemoglobin.

Noninvasive photoacoustic computed tomography (PACT)

Fig. 48a is the schematic of the PACT setup. An OPO laser (BasiScan 120, Spectra-Physics) is pumped by a Nd:YAG laser (Brilliant B, Quatel) with a third harmonic generator (355 nm) to provide pulses with wavelengths tunable from 420 nm to 680 nm. The pulse duration is 6 ns, and the pulse repetition rate is 10 Hz. The laser beam is homogenized by an optical diffuser (EDC-5, RPC Photonics) to provide uniform illumination over the mouse brain. The maximum light intensity at the tissue surface is approximately 10 mJ/cm^2 , below the ANSI limit at the chosen wavelengths. The photoacoustic signals are detected by a 5 cm diameter full-ring ultrasonic transducer array with 512 elements (Imasonic, Inc.). The central frequency of the ultrasonic transducer array is 5 MHz, and the 6-dB bandwidth is more than 80%. Each element in the array is directly shaped into an arc to produce an axial focal depth of 19 mm. The combined foci of all elements form a relatively uniform imaging region of 20 mm diameter and 1 mm thickness. Within this region, the axial (radial) resolution is 0.10 mm, and the transverse (tangential) resolution is 0.25 mm [206]. As show in Fig. 48b, after a complete data acquisition from all 512 elements, the raw data is reconstructed to form a photoacoustic image of the brain based on the universal back-projection algorithm [207]. The imaging speed of the current system is 1.6 sec per frame.

Optical-resolution photoacoustic microscopy (OR-PAM)

OR-PAM, another implementation of PAT, aims at capillary-level resolution within the optical diffusion limit [7, 32, 36, 39, 80, 81, 208]. As shown in Fig. 48c, by focusing the laser pulses to a diffraction-limit spot using an objective with an NA of 0.1 (AC127-050-A, Thorlabs), OR-PAM achieves a transverse resolution of 5 μm . By using a single-element ultrasonic transducer with a central frequency of 50 MHz and a 6-dB bandwidth of 100% (V214-BB-RM, Olympus-NDT),

OR-PAM achieves an axial resolution of 15 μm . Due to scattering by the tissue, the penetration depth of OR-PAM is limited to ~ 1 mm, which is sufficient for transcranial imaging of the cerebral cortex but not transdermal imaging. The arrival time of the PA signal provides depth information, and volumetric imaging is acquired by two-dimensional raster scanning of the sample. In this study, to validate the cortical vascular image obtained by PACT, the same mouse was imaged by OR-PAM at 570 nm after the PACT imaging. The scalp was surgically removed, while the skull was left intact. It took about 30 min to acquire an OR-PAM image over a 5×10 mm² area.

Fluorescence imaging

To confirm the stimulation induced changes in 2-NBDG uptake in brain, open-scalp fluorescence imaging using the same experimental protocol was performed on a different mouse. The fluorescence imaging system shown in Fig. 48d has been reported previously [205]. Briefly, the light source is a 120-watt xenon arc lamp (Oriel Inc.) with an excitation filter (450 ± 20 nm, FB450-40, Thorlabs). Fluorescence images are captured by a low-noise CCD camera (Meade Inc.). An emission filter (550 ± 20 nm, FB550-40, Thorlabs) and an achromatic doublet (NT45-265, Edmund) comprise the camera lens. In this study, the fluorescence images were acquired with a CCD exposure time of 0.5 sec. White-light images were acquired with a CCD exposure time of 0.05 sec after removing the emission filter and turning on the room light. Because blood vessels appeared darker than the background in the white-light images, the image intensity was reversed for better clarity.

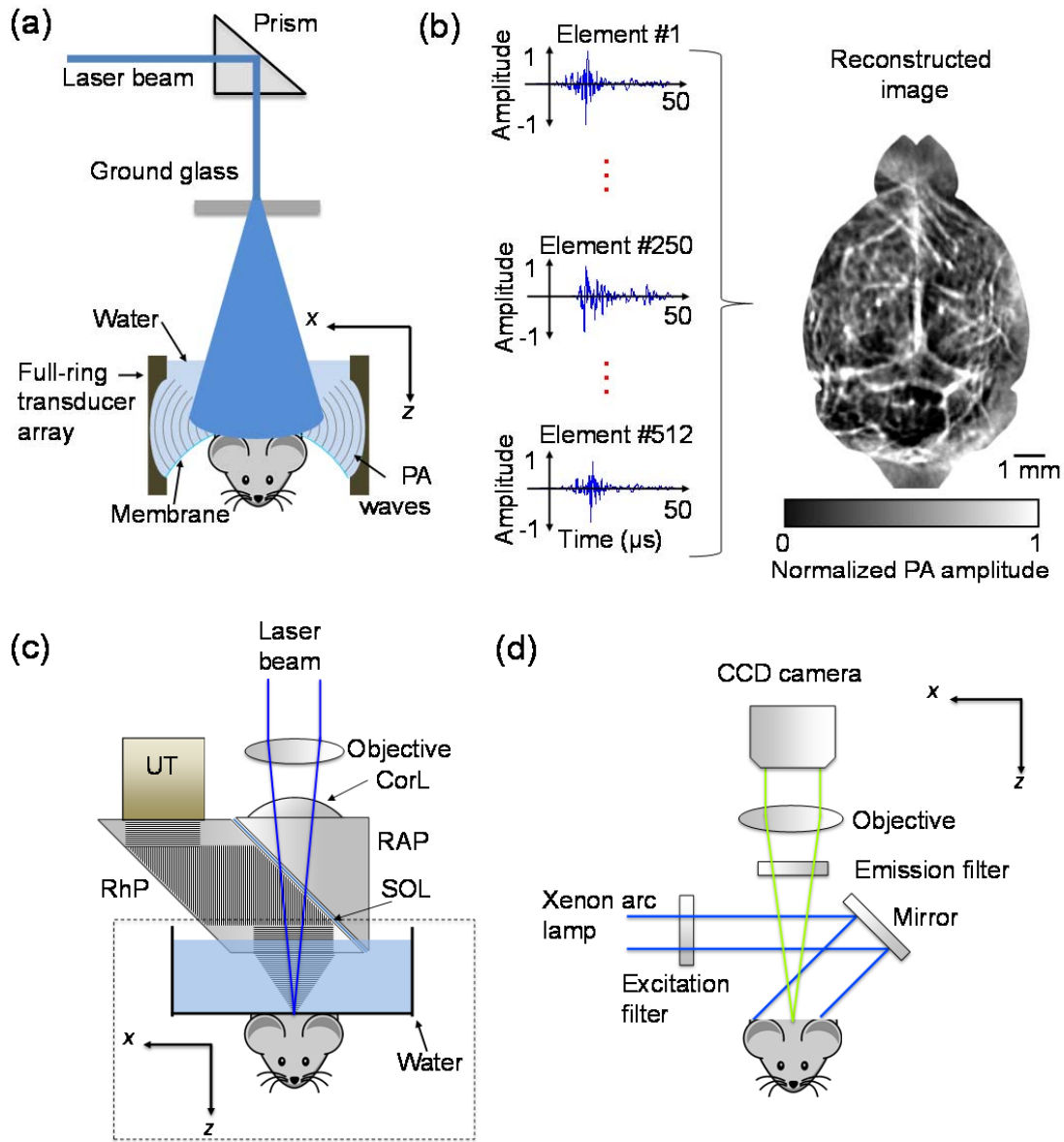


Figure 48. Photoacoustic and fluorescence imaging systems. (a) Schematic of the PACT system. (b) In PACT, upon laser excitation, the time-domain PA signals recorded by each transducer element are back-projected into the 2D imaging space based on the delay times, and then summed to form an image of the mouse cortex. (c) Schematic of the OR-PAM system, where the capillary-level lateral resolution is provided by the tight optical focusing. UT, ultrasonic transducer; CorL, correction lens; RAP, right-angled prism; RhP, rhomboid prism; SOL, silicone oil layer. (d) Schematic of the fluorescence imaging system.

Animal preparation

Female ND4 Swiss Webster mice (Harlan Laboratory, 16 to 20g) were used for the current study.

The laboratory animal protocols for this work were approved by the Animal Studies Committee

of Washington University in St. Louis. To enhance 2-NBDG uptake, the mice were fast for 24 h before the experiment [204]. Before imaging, the hair on each mouse's head was removed with a depilatory. An intraperitoneal dose of 90 mg/kg ketamine plus 10 mg/kg xylazine was used for anesthesia. The mouse was then taped to a lab-made animal holder, which was then mounted to the PACT system. Instead of being fully immersed in water, the animal was supported from below, with the head being covered by a flexible membrane. The entire experiment took less than one hour, therefore additional injection of the anesthetic mixture was not needed. The animal preparation for OR-PAM and fluorescence imaging were similar, except that there was no water coupling for fluorescence imaging. Three mice were used for PACT and subsequent OR-PAM imaging, and one mouse was used for fluorescence imaging.

Forepaw stimulation

Thirty minutes after the injection of 0.3 mL 3 mM 2-NBDG via the tail vein, stimulations were introduced by two pairs of needle electrodes inserted under the skin of the right and left forepaws, respectively. The electrodes were connected to a function generator (DS345, Stanford Research Systems) through a manual switch. The whole procedure consisted of four periods, each lasting for 3 min (Fig. 49a). The first and third periods (P_1 and P_3) were resting states, while the second period (P_2) was right paw stimulation (RPS) and the fourth period (P_4) was left paw stimulation (LPS). Each stimulation period consisted of a train of electrical pulses with an amplitude of 2 mA, a pulse width of 0.25 sec and a repetition rate of 2 Hz (Fig. 49b). PACT acquired images continuously through the four periods. The procedure was first performed for 12 minutes at 478 nm and then repeated for 12 minutes at 570 nm after a delay of 10 min. We assumed that brain responses were repeatable within the time window of the experiment.

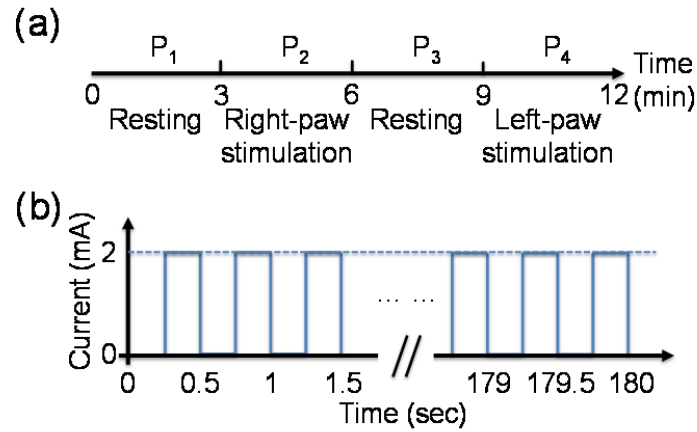


Figure 49. Time course of forepaw stimulation. (a) At each wavelength, the procedure consisted of four periods: two resting periods (P1 and P3) and two stimulation periods (P2 and P4). Each period lasted for 3 min. (b) Each stimulation period consisted of a train of electrical pulses with an amplitude of 2 mA, a pulse width of 0.25 sec and a repetition rate of 2 Hz.

Image co-registration

Before quantitative analysis, the PA images at 570 nm from OR-PAM and PACT were co-registered by using a MATLAB Image Processing Toolbox (R2010b, Mathworks, Boston, MA). Here, a 2D rigid registration was performed, which included linear translation, scaling, and rotation. The first step was to manually select 10-20 control points in the two images. The spatial translation, scaling and rotation matrix was computed based on the coordinates of these control points. The entire OR-PAM image was then transformed and registered to the PACT image using this matrix. To show the co-registration performance, the co-registered OR-PAM image was superimposed on top of the PACT image, with the overly transparency proportional to the OR-PAM image pixel values.

Signal processing

In PACT, for both phantom and *in vivo* studies, the images acquired at 478 nm and 570 nm were used to reconstruct the distribution of 2-NBDG and hemoglobin, respectively. Since deoxy- and

oxy-hemoglobin have the same absorption coefficients at 570 nm, the PA signal amplitude was proportional to the total hemoglobin concentration C_{Hb} , an index for blood perfusion.

For open-scalp OR-PAM, because the mouse skull is translucent, the attenuation of light due to the skull was neglected. The laser fluence measured at the skull surface is a good approximation of the actual fluence at the blood vessels. Therefore, C_{Hb} can be estimated as [209]

$$C_{Hb} = \frac{V_{OR}^{570}}{k_{OR} \varepsilon_{Hb}^{570} F_{OR}^{570}}. \quad (12)$$

Here, the subscript OR denotes the OR-PAM system and the superscript 570 denotes the wavelength. k_{OR} is a calibration factor measured from blood in a clear medium, which incorporates the system detection efficiency and Grueneisen coefficient. ε_{Hb}^{570} is the molar extinction coefficient of hemoglobin at 570 nm, F_{OR}^{570} is the laser fluence at the skull surface, and V_{OR}^{570} is the OR-PAM signal amplitude.

Because PACT shares the same absorption contrast as OR-PAM, the calibrated C_{Hb} from OR-PAM can be directly transferred to PACT once the images from the two systems are co-registered. We estimate the calibration factor k_{CT} for PACT by

$$k_{CT} = \frac{V_{CT}^{570}}{C_{Hb} \varepsilon_{Hb}^{570} F_{CT}^{570}}. \quad (13)$$

Here, the subscript CT denotes the PACT system. F_{CT}^{570} is the laser fluence measured at the scalp surface and V_{CT}^{570} is the PACT signal amplitude. In addition to the system detection efficiency

and Grueneisen coefficient, k_{CT} also incorporates an attenuation factor of the laser fluence at 570 nm, which cannot be neglected in PACT owing to the scalp.

The fluence attenuation of the scalp is wavelength dependent. However, the effective attenuation coefficients of the nude mouse scalp at 478 nm (7.1 cm^{-1}) and 570 nm (6.5 cm^{-1}) are approximately the same [210], and the mouse scalp is relatively thin (less than 1.5 mm) [211]. Therefore, the fluence attenuations at the two wavelengths were treated as the same. We also assumed that the heterogeneity of the scalp was negligible. Accordingly, we can estimate the 2-NBDG concentration C_{2-NBDG} as

$$C_{2-NBDG} = \frac{V_{CT}^{478}}{k_{CT} \epsilon_{2-NBDG}^{478} \eta_{2-NBDG} F_{CT}^{478}} \quad (14)$$

Here, ϵ_{2-NBDG}^{478} is the molar extinction coefficient of 2-NBDG at 478 nm. η_{2-NBDG} is the conversion efficiency from absorbed optical energy to heat, which is 45% for 2-NBDG [212]. The conversion efficiency for hemoglobin is absent in Eq. 13 because it is 100%.

Eqs. (12-14) can be used to estimate the absolute concentrations of hemoglobin and 2-NBDG in the brain. Because the absolute baseline signals vary across the brain, relative changes are more robust for quantifying the responses induced by stimulations. However, it is also important to demonstrate the absolute imaging capability of PACT, which is useful for the baseline mapping. In addition, the future quantification of the metabolic rates of oxygen and glucose requires the absolute concentrations.

In forepaw stimulations, PACT images acquired during each period (P_{1-4}) were averaged at each wavelength to increase the signal-to-noise ratio. The relative changes were computed as $(P_2 - P_1)$

/ P_1 for RPS, and as $(P_4 - P_3) / P_3$ for LPS. Only pixels with amplitude above 1.5 times the noise level were used for calculation. In response quantifications, only pixels with response magnitude above 10% of the maximum magnitude were averaged. The same procedure was also applied to the fluorescence imaging results.

Response areas at the two wavelengths were also quantified. Here, the response area was defined by the pixels with a response magnitude above 10% of the maximum response magnitude. The cortical area covered by the responding vessels was estimated as well. An ellipse equation was used to fit the outline of the responding vessels, with the center, major axis, minor axis and orientation as the fitting variables. The area of the best fit ellipse was approximated as the covered area.

5.2.2 Results

PACT of 2-NBDG and blood phantom

A phantom study was first performed to validate the spectral separation of 2-NBDG and blood. As shown in Fig. 50a, whole bovine blood (hemoglobin concentration: 2.5 mM) and 0.4 mM 2-NBDG solution were embedded in gelatin and imaged by PACT at 478 nm and 570 nm. This 2-NBDG concentration was close to the estimated 2-NBDG concentration in animal studies to be performed later. The ratios between the averaged PA signal amplitudes of 2-NBDG and blood at 478 nm and 570 nm were 9:1 and 0.06:1, respectively (Fig. 50b). Blood was almost invisible at 478 nm, so was 2-NBDG at 570 nm. The PA amplitude of the 2-NBDG sample happened to be nearly identical to (0.98 times) that of the blood sample at 570 nm. Therefore, 2-NBDG and blood could be separated as shown in Fig. 50c. In addition, we found that 2-NBDG was more

diffusive than hemoglobin (molecular weight: 64,458) in gelatin, due to the much smaller size of 2-NBDG molecules.

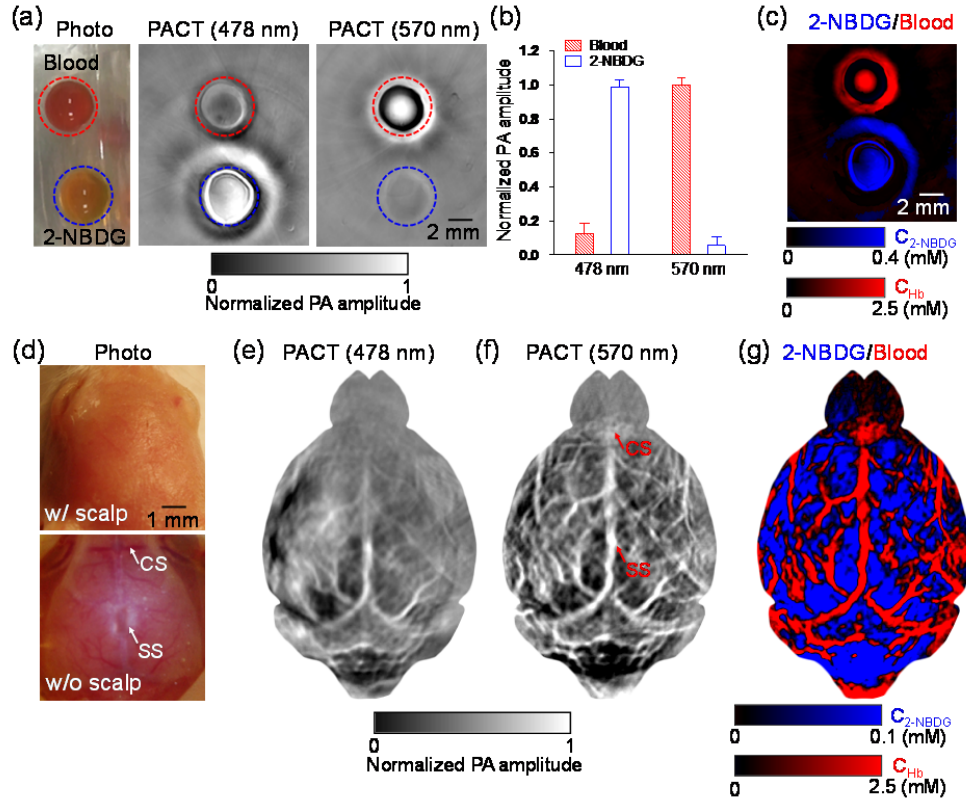


Figure 50. Multi-wavelength PACT *in vitro* and *in vivo*. (a) Photograph (left) and PACT images (middle and right) of whole bovine blood and 0.4 mM 2-NBDG in a gelatin phantom. (b) Averaged PA amplitudes from blood and 2-NBDG, normalized by the PA amplitude of blood at 570 nm. (c) Spectral separation of blood (shown in red) and 2-NBDG (shown in blue). CHb: total hemoglobin concentration; C_{2-NBDG}: 2-NBDG concentration. (d) Photograph of a mouse brain with its scalp intact (top) and removed (bottom). SS: sagittal sinus; CS coronal suture. (e-f) PACT images of the mouse brain at (e) 2-NBDG-dominant 478 nm and (f) hemoglobin-dominant 570 nm, respectively. (g) Spectral separation of blood (shown in red) and 2-NBDG (shown in blue) in the brain.

PACT of mouse brain

Figs. 50e-f are noninvasive PACT images of a mouse brain, acquired 30 min after 2-NBDG administration. At 478 nm, the PA signal amplitudes reflected the 2-NBDG concentration in the brain tissue (Fig. 50e). At 570 nm, the PA signal amplitudes reflected the total hemoglobin concentration in blood vessels (Fig. 50f). Cortical vascular landmarks including the sagittal sinus

(SS) and coronal suture (CS) were clearly imaged by PACT and confirmed by open-scalp photography. A merged image of C_{Hb} and C_{2-NBDG} is shown in Fig. 50g, where 2-NBDG signals from blood vessels were excluded. The hemoglobin distribution was superimposed on top of the 2-NBDG distribution, with the transparency of the hemoglobin layer proportional to its pixel values. Capillary-level OR-PAM images of the same mouse are shown in Figs. 51a-b. The co-registration results show that the transdermal and transcranial PACT image agreed well with the open-scalp OR-PAM image, as shown in Fig. 51c-d.

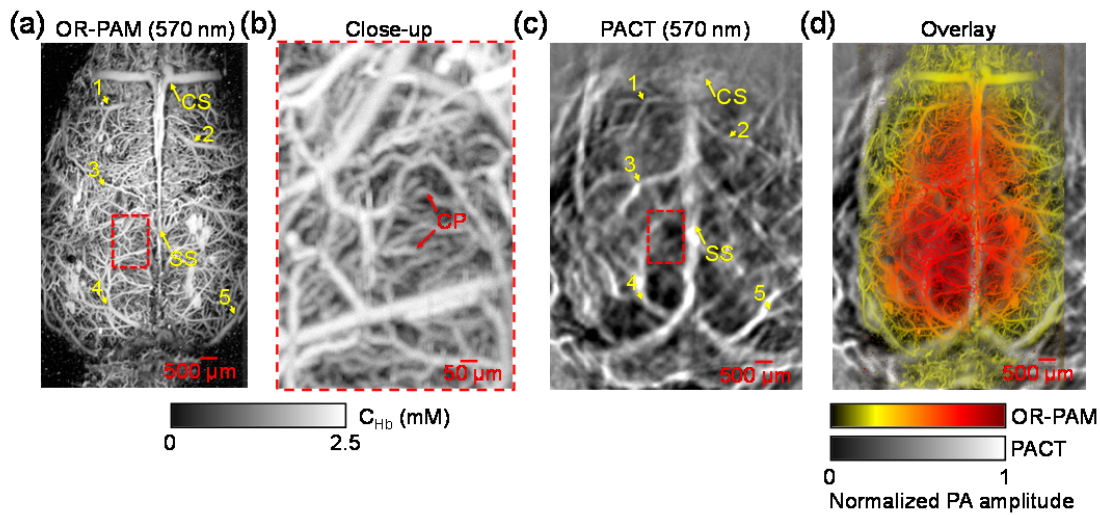


Figure 51. High-resolution OR-PAM imaging of the mouse brain after PACT imaging. (a) OR-PAM image of the mouse brain, acquired at 570 nm with the scalp removed and the skull left intact. C_{Hb} : total hemoglobin concentration; SS: sagittal sinus; CS: coronal suture. The numbers denote representative control points selected for image co-registration. (b) Close-up of region inside the dashed box in (a) showing the dense capillaries in the brain cortex. CP: capillary. (c) PACT image of the same mouse brain with intact scalp and skull. The numbers denote the control points corresponding to those in (a). (d) Co-registered OR-PAM image (shown in color) superimposed on the PACT image (shown in gray).

PACT of cortical responses to forepaw stimulations

Fig. 52a-b are the relative changes of PA signals induced by forepaw stimulations. At 478 nm (Fig. 52a), the RPS and LPS caused PA signal amplitudes to increase by $3.6\% \pm 2.2\%$ and $2.0\% \pm 1.1\%$ in the somatosensory region (SR) of the contralateral hemisphere, respectively. Such

increases indicate elevated glucose uptake rates, and thus reflect increased neuron activity. Under the two stimulations, the response areas were $5.7 \pm 1.3 \text{ mm}^2$ and $7.4 \pm 2.5 \text{ mm}^2$, respectively.

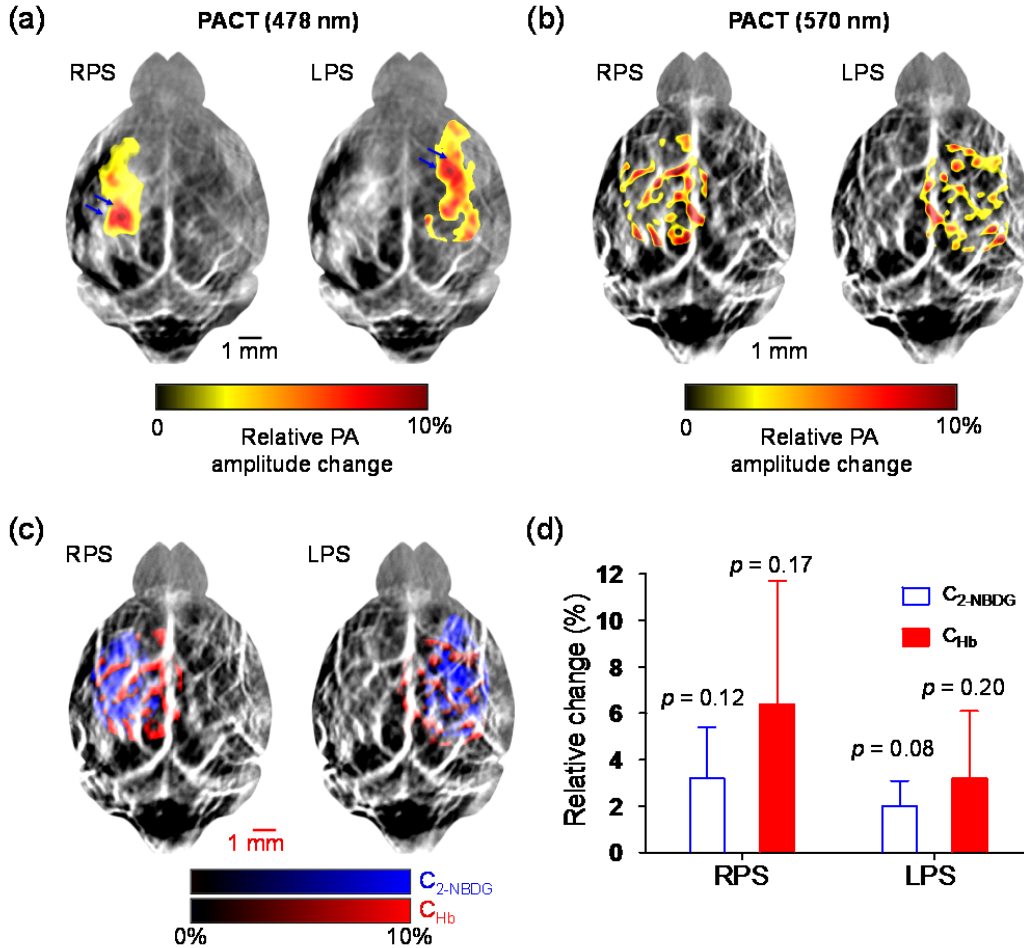


Figure 52. PACT of the cortical responses to forepaw stimulations. (a-b) Relative changes of the PA amplitudes (shown in color) acquired at (a) 2-NBDG-dominant 478 nm and (b) hemoglobin-dominant 570 nm under the right paw stimulation (RPS) and left paw stimulation (LPS), superimposed on the resting-state image (shown in gray). The threshold for the overlay transparency was set to be 10% of the maximum response. (c) Overlaid images showing the relative changes of 2-NBDG concentration (C₂-NBDG, shown in blue) and total hemoglobin concentration (CHb, shown in red), superimposed on the resting-state image at 570 nm (shown in gray). (d) Relative changes of C₂-NBDG and CHb averaged over three mice. Error bars: standard deviation. The p values were calculated from paired Student's t-test between stimulated states P2 or P4 and resting states P1 or P3.

Similarly, at 570 nm (Fig. 52b], the RPS and LPS caused PA signal amplitudes to increase by $6.4\% \pm 5.3\%$ and $3.2\% \pm 2.9\%$ in the contralateral hemisphere, respectively. Such changes indicate an

increase in total hemoglobin concentration arising from elevated inflows of fresh blood, and thus reflect increased neuron activity as well. Under the two stimulations, the response areas were $4.7 \pm 1.5 \text{ mm}^2$ and $4.5 \pm 1.2 \text{ mm}^2$, respectively. Furthermore, the responding vessels covered much larger cortical regions of $16.5 \pm 3.3 \text{ mm}^2$ and $15.1 \pm 2.5 \text{ mm}^2$, respectively, as shown in Fig. 53a. The areas covered by the responding vessels were significantly wider than the 2-NBDG response areas for both RPS and LPS, with p values less than 0.05 (Fig. 53b).

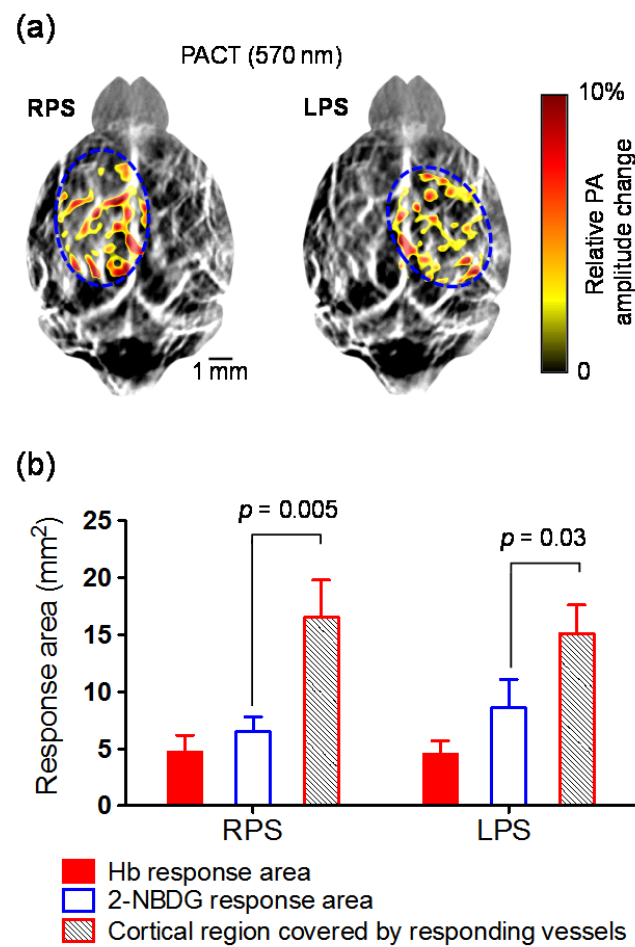


Figure 53. Quantification of the cortical region covered by responding vessels. (a) An ellipse was used to fit the outline of the responding vessels, with the center, major axis, minor axis and orientation as the fitting variables. (b) Quantification of hemoglobin response area, 2-NBDG response area and cortical region covered by responding vessels, averaged over three mice. Error bars: standard deviation. The p values were calculated from paired Student's t -test between the 2-NBDG response area and the cortical region covered by responding vessels.

In addition, the linear regression shows that the 2-NBDG response amplitude was approximately proportional to that of the hemoglobin response for both RPS and LPS, with ratios of ~ 0.48 and ~ 0.52 , respectively (Fig. 54a). Similarly, the ratios between the 2-NBDG response area and the area covered by the responding vessels were ~ 0.41 and ~ 0.57 for RPS and LPS, respectively (Fig. 54b). The high correlation of the two responses may reflect the close coupling between oxygen metabolism and glucose metabolism in the brain.

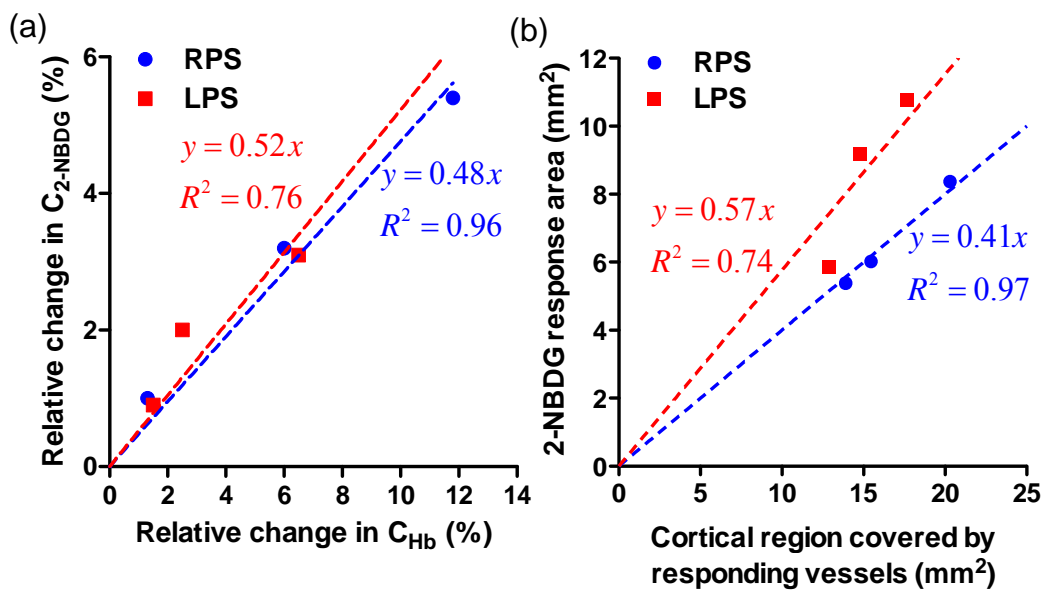


Figure 54. Correlation of the hemodynamic response and glucose response. (a) Linear regression of the 2-NBDG response amplitude and the hemoglobin response amplitude for RPS and LPS on three mice. (b) Linear regression of the 2-NBDG response area and cortical area covered by responding vessels for RPS and LPS on three mice.

Fluorescence imaging of cortical responses to forepaw stimulations

First, whole bovine blood and 2-NBDG (0.4 mM) were enclosed in 1 mm diameter glass tubes and imaged by our fluorescence setup (Fig. 55a). The fluorescence image shows that blood did not generate fluorescence while 2-NBDG did profusely.

Second, using the same experimental protocol as in PACT, we imaged the cortical responses to forepaw stimulations on a different mouse using the fluorescence setup. The results are shown in Fig. 55b. While the white light image shows the detailed cortical vasculature, the fluorescence image shows the 2-NBDG distribution and thus the glucose metabolism. The RPS and LPS induced fluorescence intensity to increase by 5.1% and 6.2% in the SR of the contralateral hemisphere, respectively. Such increases indicate elevated glucose uptakes in the SR, which qualitatively agree with the glucose responses assessed by PACT.

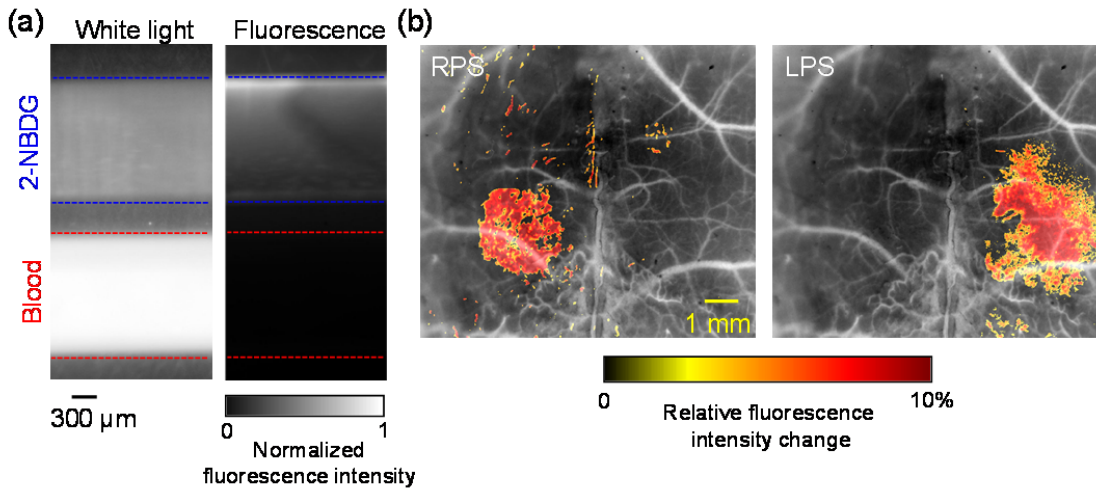


Figure 55. Fluorescence imaging of mouse brain responses to forepaw stimulations. (a) Left: intensity-reversed white-light image of two glass tubes filled with 2-NBDG (0.4 mM) and whole bovine blood. Right: fluorescence image of the two tubes. (b) Relative changes of the fluorescence intensity under RPS and LPS (shown in color), superimposed on the intensity-reversed white-light image of the brain cortex (shown in gray), with the scalp removed and skull left intact. The threshold for the overlay transparency was set to be 10% of the maximum response.

5.2.3. Conclusions and discussion

The pathways of oxygen metabolism and glucose metabolism are closely coupled in neuron activity. One of the recent uses of PACT is the label-free measurement of metabolic rate of oxygen (MRO_2) [5, 39]. Currently, except for blood flow speed, PACT can measure all the other parameters required for quantifying MRO_2 , namely vessel cross-section, oxygen saturation and

total concentration of hemoglobin, and tissue volume. Recently, a few PA methods have been proposed for blood flow measurement in deep tissue, which may be applicable to PACT [76-78, 213]. Therefore, PACT has the potential to simultaneously image the two metabolic pathways: oxygen metabolism as described by others, and glucose metabolism as shown in this paper.

Previous studies by PET and fMRI have shown that forepaw stimulations can increase the cerebral metabolic rate of oxygen (CMRO₂) [214-216]. Because the blood oxygenation change is much smaller than the blood flow change, such increase in CMRO₂ is mainly attributed to the elevated blood perfusion [214-216]. In our results, the intensified photoacoustic signal at 570 nm provided a direct evidence of the increase in blood perfusion. For absolute CMRO₂ quantification, our future work will incorporate the oxygenation measurement by using multiwavelength measurements.

In addition, we found that the glucose response area was confined within the SR, while the hemodynamic response area was much larger than that. Glucose response was a focal activity restricted to neurons responsible for the stimulated site. In contrast, hemodynamic response was less spatially restricted since fresh blood must be delivered from the major feeding arteries, through the capillaries of the SR, to the major draining veins. Moreover, the hemodynamic response may spread into neighboring vessels of the same vascular network.

Except for the dimensional discrepancy, the glucose response area was more homogenous than the hemodynamic response area. The latter was characterized by a strong vascular pattern. Moreover, there was a clear core for the glucose response, which is indicated by the double arrows in Fig. 52a. Such a core was not seen in the hemodynamic response. This again suggests

that glucose response was a focal activity. The core region contained the neurons most sensitive to the stimulated site.

In summary, using 2-NBDG as the exogenous contrast and hemoglobin as the endogenous contrast, we have demonstrated that PACT is capable of imaging the metabolic response of a mouse brain to forepaw stimulations. As a quantitative imaging modality, PACT can spectrally separate 2-NBDG and hemoglobin by virtue of its optical absorption contrast. As a fast imaging modality, PACT can acquire a volumetric image in less than two seconds with a laser repetition rate of 10 Hz. This imaging speed can be further improved by a laser system with higher repetition rate and automatic wavelength switch. As a deep imaging modality, PACT can transdermally and transcranially localize the spatial patterns of the brain responses by virtue of its high ultrasonic resolution. With all these merits, we expect PACT to be applied to more brain metabolism studies in the future.

6. Future work

PAM has the following notable features: (1) PAM has highly scalable spatial resolution and maximum imaging depth in both the optical and acoustic domains. (2) PAM images optical absorption contrast with 100% sensitivity, and provides images without speckle artifacts. (3) PAM can essentially image all molecules at their absorbing wavelengths. (4) PAM is capable of functional and metabolic imaging in absolute units using endogenous contrast agents.

As in modern optical microscopy, it is possible to combine multiple optical objectives with different magnification powers to a single OR-PAM system for fast resolution switching. However, the confocal alignment of the optical illumination and acoustic detection needs to be maintained. Typically, a microscope objective with a higher NA comes with a shorter focal

length. To keep the imaged object in focus, one solution is to use a specially designed parafocal lens, which is capable of varying the effective NA without changing the optical focal length. Similarly, it is also possible to integrate multiple ultrasonic transducers with different central frequencies into a single AR-PAM system, while keeping the same illumination. Furthermore, OR-PAM can be combined with AR-PAM as a single device to cover a wider scale range. Since OR-PAM and AR-PAM can share the same detection, only the optical illumination needs to be integrated.

Integration between PAM and other imaging modalities can provide complementary contrasts, thus is a direction for future PAM development. So far, PAM has been integrated with back-scattered optical microscopy (scattering contrast) [217], fluorescence microscopy (fluorescence contrast) [132, 158, 218], optical coherence tomography (scattering contrast) [132, 219], two-photon microscopy (fluorescence contrast) [220] and pulse-echo ultrasound imaging (mechanical and elastic contrast) [221, 222]. In these integrated systems, the two sub-systems share either the same illumination or detection. Therefore, their images are inherently co-registered. In addition to providing complementary contrast, PAM has been combined with a high intensity focused ultrasound (HIFU) system for therapeutics, where PAM is used to outline the location and shape of tumors and guide the subsequent HIFU therapy or drug release [145, 223]. In addition to the integration of instrumentations, new exogenous contrast agents have also been integrated for multi-modal systems. For example, perfluorocarbon nanoparticles loaded with near-infrared dyes have been used as a dual contrast agent for fluorescence imaging and PAM imaging [224].

Another direction is to miniaturize the PAM system for internal organ and intravascular imaging [168, 225-231]. The first sideways looking photoacoustic endoscope (PAE) with a 4.2-mm-diameter probe has been demonstrated in acoustic-resolution mode for functional esophagus and

colon imaging on small animal models [225, 227]. The bottleneck for further miniaturization of the PAE probe involves integrating the light delivery fiber with a conventional piezoelectric transducer. Despite the complex fabrication procedures for miniature piezoelectric detector, its detection sensitivity decreases with its size. By contrast, optical detection of ultrasound pressure using a transparent Fabry-Perot sensor may be an alternative solution [232]. Theoretically, PAE should enjoy the same scalability as PAM. Since most cancers start from the epithelial layer, PAE can be implemented in optical-resolution mode for high-resolution epithelial imaging of early-stage cancer [225-227]. Delivery of coupling medium for acoustic propagation remains another challenge for PAE imaging of internal lumens such as the trachea and gastrointestinal (GI) tract. It has been suggested that water and ultrasound gel can be introduced to the GI tract [226, 227]. However, it is challenging to apply water to the respiratory system. An inflatable balloon with a water filling channel could be a solution [233]. By contrast, it is less problematic for intravascular PAE imaging since blood is a natural acoustic coupling medium. However, the strong absorption of blood in the visible spectral range requires the use of near-infrared wavelengths. Alternatively, blood can be flushed with saline.

As a maturing imaging technique, PAM is expected to find new applications in both fundamental life science and clinical practice, which include but are not limited to tumor angiogenesis, lymphatic dynamics, neural activity, brain metabolism, cancer detection, drug delivery and intraoperative monitoring. While PAM has been commercialized for pre-clinical applications, future commercialization for clinical applications will greatly accelerate the translation of PAM from a lab technology to a mainstream imaging modality.

References

1. Amos, B., *Lessons from the history of light microscopy*. Nature Cell Biology, 2000. **2**(8): p. E151-E152.
2. Wang, L.V. and H.-i. Wu, *Biomedical optics : principles and imaging*. 2007, Hoboken, N.J.: Wiley-Interscience. xiv, 362.
3. Wang, L.H.V. and S. Hu, *Photoacoustic Tomography: In Vivo Imaging from Organelles to Organs*. Science, 2012. **335**(6075): p. 1458-1462.
4. Wang, L.V., *Tutorial on photoacoustic microscopy and computed tomography*. Ieee Journal of Selected Topics in Quantum Electronics, 2008. **14**(1): p. 171-179.
5. Wang, L.V., *Prospects of photoacoustic tomography*. Medical Physics, 2008. **35**(12): p. 5758-5767.
6. Wang, L.V., *Multiscale photoacoustic microscopy and computed tomography*. Nature Photonics, 2009. **3**(9): p. 503-509.
7. Yao, J. and L.V. Wang, *Photoacoustic tomography: fundamentals, advances and prospects*. Contrast Media Mol Imaging, 2011. **6**(5): p. 332-345.
8. Kim, C., C. Favazza, and L.H.V. Wang, *In Vivo Photoacoustic Tomography of Chemicals: High-Resolution Functional and Molecular Optical Imaging at New Depths*. Chemical Reviews, 2010. **110**(5): p. 2756-2782.
9. Li, C.H. and L.H.V. Wang, *Photoacoustic tomography and sensing in biomedicine*. Physics in Medicine and Biology, 2009. **54**(19): p. R59-R97.
10. Oraevsky, A.A., S.L. Jacques, and F.K. Tittel, *Measurement of tissue optical properties by time-resolved detection of laser-induced transient stress*. Applied Optics, 1997. **36**(1): p. 402-415.
11. Esenaliev, R.O., A.A. Karabutov, and A.A. Oraevsky, *Sensitivity of laser opto-acoustic imaging in detection of small deeply embedded tumors*. Ieee Journal of Selected Topics in Quantum Electronics, 1999. **5**(4): p. 981-988.
12. Kruger, R.A., P.Y. Liu, Y.R. Fang, and C.R. Appledorn, *Photoacoustic Ultrasound (Paus) - Reconstruction Tomography*. Medical Physics, 1995. **22**(10): p. 1605-1609.
13. Kruger, R.A., D.R. Reinecke, and G.A. Kruger, *Thermoacoustic computed tomography-technical considerations*. Medical Physics, 1999. **26**(9): p. 1832-1837.
14. Viator, J.A., S.L. Jacques, and S.A. Prahl, *Depth profiling of absorbing soft materials using photoacoustic methods*. Ieee Journal of Selected Topics in Quantum Electronics, 1999. **5**(4): p. 989-996.
15. Calasso, I.G., W. Craig, and G.J. Diebold, *Photoacoustic point source*. Physical Review Letters, 2001. **86**(16): p. 3550-3553.
16. Grashin, P.S., A.A. Karabutov, A.A. Oraevsky, I.M. Pelivanov, N.B. Podymova, E.V. Savateeva, and V.S. Solomatin, *Distribution of the laser radiation intensity in turbid media: Monte Carlo simulations, theoretical analysis, and results of optoacoustic measurements*. Quantum Electronics, 2002. **32**(10): p. 868-874.
17. Andreev, V.G., A.A. Karabutov, and A.A. Oraevsky, *Detection of ultrawide-band ultrasound pulses in optoacoustic tomography*. Ieee Transactions on Ultrasonics Ferroelectrics and Frequency Control, 2003. **50**(10): p. 1383-1390.
18. Sehgal, C.M. and J.F. Greenleaf, *Scattering of Ultrasound by Tissues*. Ultrasonic Imaging, 1984. **6**(1): p. 60-80.

19. Luke, G.P., D. Yeager, and S.Y. Emelianov, *Biomedical applications of photoacoustic imaging with exogenous contrast agents*. Annals of biomedical engineering, 2012. **40**(2): p. 422-437.
20. Hu, S. and L.V. Wang, *Neurovascular photoacoustic tomography*. Front Neuroenergetics, 2010. **2**: p. 10.
21. Hu, S. and L.V. Wang, *Photoacoustic imaging and characterization of the microvasculature*. Journal of Biomedical Optics, 2010. **15**(1): p. 011101.
22. Emelianov, S.Y., P.C. Li, and M. O'donnell, *Photoacoustics for molecular imaging and therapy*. Physics Today, 2009. **62**(5): p. 34-39.
23. Karabutov, A.A., E.V. Savateeva, and A.A. Oraevsky, *Optoacoustic tomography: New modality of laser diagnostic systems*. Laser Physics, 2003. **13**(5): p. 711-723.
24. Brecht, H.P., R. Su, M. Fronheiser, S.A. Ermilov, A. Conjusteau, and A.A. Oraevsky, *Whole-body three-dimensional optoacoustic tomography system for small animals*. Journal of Biomedical Optics, 2009. **14**(6): p. 064007.
25. Ermilov, S.A., T. Khamapirad, A. Conjusteau, M.H. Leonard, R. Lacewell, K. Mehta, T. Miller, and A.A. Oraevsky, *Laser optoacoustic imaging system for detection of breast cancer*. Journal of Biomedical Optics, 2009. **14**(2): p. 024007.
26. Wang, X.D., Y.J. Pang, G. Ku, X.Y. Xie, G. Stoica, and L.H.V. Wang, *Noninvasive laser-induced photoacoustic tomography for structural and functional in vivo imaging of the brain*. Nature Biotechnology, 2003. **21**(7): p. 803-806.
27. Xu, M.H. and L.H.V. Wang, *Universal back-projection algorithm for photoacoustic computed tomography*. Physical Review E, 2005. **71**(1): p. 016706.
28. Kruger, R.A., R.B. Lam, D.R. Reinecke, S.P. Del Rio, and R.P. Doyle, *Photoacoustic angiography of the breast*. Medical Physics, 2010. **37**(11): p. 6096-6100.
29. Burgholzer, P., G.J. Matt, M. Haltmeier, and G. Paltauf, *Exact and approximative imaging methods for photoacoustic tomography using an arbitrary detection surface*. Physical Review E, 2007. **75**(4): p. 046706.
30. Manohar, S., A. Kharine, J.C.G. van Hespén, W. Steenbergen, and T.G. van Leeuwen, *The Twente Photoacoustic Mammoscope: system overview and performance*. Physics in Medicine and Biology, 2005. **50**(11): p. 2543-2557.
31. Gamelin, J., A. Aguirre, A. Maurudis, F. Huang, D. Castillo, L.V. Wang, and Q. Zhu, *Curved array photoacoustic tomographic system for small animal imaging*. Journal of Biomedical Optics, 2008. **13**(2): p. 024007.
32. Maslov, K., H.F. Zhang, S. Hu, and L.V. Wang, *Optical-resolution photoacoustic microscopy for in vivo imaging of single capillaries*. Optics Letters, 2008. **33**(9): p. 929-931.
33. Zhang, H.F., K. Maslov, G. Stoica, and L.H.V. Wang, *Functional photoacoustic microscopy for high-resolution and noninvasive in vivo imaging*. Nature Biotechnology, 2006. **24**(7): p. 848-851.
34. Maslov, K., G. Stoica, and L.H.V. Wang, *In vivo dark-field reflection-mode photoacoustic microscopy*. Optics Letters, 2005. **30**(6): p. 625-627.
35. Zhang, C., K. Maslov, and L.H.V. Wang, *Subwavelength-resolution label-free photoacoustic microscopy of optical absorption in vivo*. Optics Letters, 2010. **35**(19): p. 3195-3197.

36. Hu, S., K. Maslov, and L.V. Wang, *Second-generation optical-resolution photoacoustic microscopy with improved sensitivity and speed*. Optics Letters, 2011. **36**(7): p. 1134-1136.
37. Zhang, C., K. Maslov, J. Yao, and L.V. Wang, *In vivo photoacoustic microscopy with 7.6- μ m axial resolution using a commercial 125-MHz ultrasonic transducer*. Journal of Biomedical Optics, 2012. **17**(11): p. 116016.
38. Matcher, S.J., M. Cope, and D.T. Delpy, *In vivo measurements of the wavelength dependence of tissue-scattering coefficients between 760 and 900 nm measured with time-resolved spectroscopy*. Applied Optics, 1997. **36**(1): p. 386-396.
39. Yao, J., K.I. Maslov, Y. Zhang, Y. Xia, and L.V. Wang, *Label-free oxygen-metabolic photoacoustic microscopy in vivo*. Journal of Biomedical Optics, 2011. **16**(7): p. 076003.
40. Abounader, R., J. Vogel, and W. Kuschinsky, *Patterns of capillary plasma perfusion in brains of conscious rats during normocapnia and hypercapnia*. Circulation Research, 1995. **76**(1): p. 120-126.
41. Chaigneau, E., M. Oheim, E. Audinat, and S. Charpak, *Two-photon imaging of capillary blood flow in olfactory bulb glomeruli*. Proceedings of the National Academy of Sciences of the United States of America, 2003. **100**(22): p. 13081-13086.
42. Villringer, A., A. Them, U. Lindauer, K. Einhaupl, and U. Dirnagl, *Capillary Perfusion of the Rat-Brain Cortex - an in-Vivo Confocal Microscopy Study*. Circulation Research, 1994. **75**(1): p. 55-62.
43. Carmeliet, P. and R.K. Jain, *Angiogenesis in cancer and other diseases*. Nature, 2000. **407**(6801): p. 249-257.
44. Poulsen, T.D., T. Klausen, J.P. Richalet, I.L. Kanstrup, N. Fogh-Andersen, and N.V. Olsen, *Plasma volume in acute hypoxia: comparison of a carbon monoxide rebreathing method and dye dilution with Evans' blue*. European Journal of Applied Physiology, 1998. **77**(5): p. 457-461.
45. Harrell, M.I., B.M. Iritani, and A. Ruddell, *Lymph node mapping in the mouse*. Journal of Immunological Methods, 2008. **332**(1-2): p. 170-174.
46. Roberts, W.G. and G.E. Palade, *Increased microvascular permeability and endothelial fenestration induced by vascular endothelial growth-factor*. Journal of Cell Science, 1995. **108**(6): p. 2369-2379.
47. Patterson, C.E., R.A. Rhoades, and J.G.N. Garcia, *Evans Blue-dye as a marker of albumin clearance in cultured endothelial monolayer and isolated lung*. Journal of Applied Physiology, 1992. **72**(3): p. 865-873.
48. Xu, Q.W., T. Qaum, and A.P. Adamis, *Sensitive blood-retinal barrier breakdown quantitation using Evans blue*. Investigative Ophthalmology & Visual Science, 2001. **42**(3): p. 789-794.
49. Gregersen, M.I. and R.A. Rawson, *The disappearance of T-1824 and structurally related dyes from the blood stream*. Am J Physiol, 1943. **138**(5): p. 698-707.
50. Rawson, R.A., *The binding of T-1824 and structurally related diazo dyes by the plasma proteins*. Am J Physiol, 1943. **138**(5): p. 708-717.
51. Klotz, I.M., F.M. Walker, and R.B. Pivan, *The binding of organic Ions by proteins I*. Journal of the American Chemical Society, 1946. **68**(8): p. 1486-1490.
52. LeVeen, H.H. and W.H. Fishman, *Combination of Evans blue with plasma protein: its significance in capillary permeability studies, blood dye disappearance curves, and its use as a protein tag*. Am J Physiol, 1947. **151**(1): p. 26-33.

53. Basu, S., J.A. Nagy, S. Pal, E. Vasile, I.A. Eckelhoefer, V.S. Bliss, E.J. Manseau, P.S. Dasgupta, H.F. Dvorak, and D. Mukhopadhyay, *The neurotransmitter dopamine inhibits angiogenesis induced by vascular permeability factor/vascular endothelial growth factor*. Nature Medicine, 2001. **7**(5): p. 569-574.
54. Sluiter, W., L.W.M. Oomens, A. Brand, and R. Vanfurth, *Determination of blood-volume in the mouse with chromium-51-labeled erythrocytes*. Journal of Immunological Methods, 1984. **73**(1): p. 221-225.
55. Pilatou, M.C.M., E; Mul, F.F.M. de; Steenbergen, W, *Photoacoustic imaging of brain perfusion on albino rats by using Evans Blue as contrast agent*. Archives of Physiology and Biochemistry, 2003. **111**(4): p. 389-397.
56. Sear, H., T.H. Allen, and M.I. Gregersen, *Simultaneous measurement in dogs of plasma volume with I131 human albumin and T-1824 with comparisons of their long term disappearance from the plasma*. Am J Physiol, 1953. **175**(2): p. 240-242.
57. Wade, M.H., J.E. Trosko, and M. Schindler, *A fluorescence photobleaching assay of gap junction-mediated communication between human cells*. Science, 1986. **232**(4749): p. 525-528.
58. Hamer, P.W., J.M. McGeachie, M.J. Davies, and M.D. Grounds, *Evans Blue Dye as an in vivo marker of myofibre damage: optimising parameters for detecting initial myofibre membrane permeability*. Journal of Anatomy, 2002. **200**(1): p. 69-79.
59. Thurston, G., C. Suri, K. Smith, J. McClain, T.N. Sato, G.D. Yancopoulos, and D.M. McDonald, *Leakage-resistant blood vessels in mice transgenically overexpressing angiopoietin-I*. Science, 1999. **286**(5449): p. 2511-2514.
60. Thody, A.J. and S. Shuster, *Control and function of sebaceous glands*. Physiological Reviews, 1989. **69**(2): p. 383-416.
61. Xu, M.H. and L.H.V. Wang, *Photoacoustic imaging in biomedicine*. Review of Scientific Instruments, 2006. **77**(4): p. 041101.
62. Fang, H., K. Maslov, and L.V. Wang, *Photoacoustic Doppler effect from flowing small light-absorbing particles*. Physical Review Letters, 2007. **99**(18): p. 184501.
63. Fang, H., K. Maslov, and L.V. Wang, *Photoacoustic Doppler flow measurement in optically scattering media*. Applied Physics Letters, 2007. **91**(26): p. 264103.
64. Fang, H. and L.H.V. Wang, *M-mode photoacoustic particle flow imaging*. Optics Letters, 2009. **34**(5): p. 671-673.
65. Zhao, Y.H., Z.P. Chen, C. Saxer, S.H. Xiang, J.F. de Boer, and J.S. Nelson, *Phase-resolved optical coherence tomography and optical Doppler tomography for imaging blood flow in human skin with fast scanning speed and high velocity sensitivity*. Optics Letters, 2000. **25**(2): p. 114-116.
66. Ren, H.W., K.M. Brecke, Z.H. Ding, Y.H. Zhao, J.S. Nelson, and Z.P. Chen, *Imaging and quantifying transverse flow velocity with the Doppler bandwidth in a phase-resolved functional optical coherence tomography*. Optics Letters, 2002. **27**(6): p. 409-411.
67. Newhouse, V.L., D. Censor, T. Vontz, J.A. Cisneros, and B.B. Goldberg, *Ultrasound Doppler Probing of Flows Transverse with Respect to Beam Axis*. Ieee Transactions on Biomedical Engineering, 1987. **34**(10): p. 779-789.
68. Yeung, K.W.W., *Angle-insensitive flow measurement using Doppler bandwidth*. Ieee Transactions on Ultrasonics Ferroelectrics and Frequency Control, 1998. **45**(3): p. 574-580.

69. Kogan, S., *Electronic noise and fluctuations in solids*. 2008, Cambridge: Cambridge University Press. 376p.
70. Jones, S.A., *Fundamental Sources of Error and Spectral Broadening in Doppler Ultrasound Signals*. Critical Reviews in Biomedical Engineering, 1993. **21**(5): p. 399-483.
71. Newhouse, V.L., E.S. Furgason, G.F. Johnson, and D.A. Wolf, *The Dependence of Ultrasound Doppler Bandwidth on Beam Geometry*. Ieee Transactions on Sonics and Ultrasonics, 1980. **27**(2): p. 50-59.
72. Zhao, Y.H., Z.P. Chen, C. Saxer, Q.M. Shen, S.H. Xiang, J.F. de Boer, and J.S. Nelson, *Doppler standard deviation imaging for clinical monitoring of in vivo human skin blood flow*. Optics Letters, 2000. **25**(18): p. 1358-1360.
73. Kasai, C., *Real-Time Two-Dimensional Blood-Flow Imaging Using an Autocorrelation Technique*. Ieee Transactions on Ultrasonics Ferroelectrics and Frequency Control, 1986. **33**(1): p. 94-94.
74. Hu, S., K. Maslov, V. Tsytarev, and L.V. Wang, *Functional transcranial brain imaging by optical-resolution photoacoustic microscopy*. Journal of Biomedical Optics, 2009. **14**(4): p. 040503.
75. Hu, N. and E.B. Clark, *Hemodynamics of the Stage-12 to Stage-29 Chick-Embryo*. Circulation Research, 1989. **65**(6): p. 1665-1670.
76. Sheinfeld, A., S. Gilead, and A. Eyal, *Photoacoustic Doppler measurement of flow using tone burst excitation*. Optics Express, 2010. **18**(5): p. 4212-4221.
77. Fang, H., K. Maslov, and L.V. Wang, *Photoacoustic Doppler effect from flowing small light-absorbing particles*. Phys Rev Lett, 2007. **99**(18): p. 184501.
78. Brunner, J. and P. Beard. *Pulsed photoacoustic Doppler flowmetry using a cross correlation method*. 2010. San Francisco, California, USA: SPIE.
79. Sheinfeld, A., S. Gilead, and A. Eyal. *Time-resolved photoacoustic Doppler characterization of flow using pulsed excitation*. 2010. San Francisco, California, USA: SPIE.
80. Yao, J., K.I. Maslov, Y. Shi, L.A. Taber, and L.V. Wang, *In vivo photoacoustic imaging of transverse blood flow by using Doppler broadening of bandwidth*. Opt. Lett., 2010. **35**(9): p. 1419-1421.
81. Yao, J. and L.V. Wang, *Transverse flow imaging based on photoacoustic Doppler bandwidth broadening*. Journal of Biomedical Optics, 2010. **15**(2): p. 021304.
82. Chen, S.L., T. Ling, S.W. Huang, H. Won Baac, and L.J. Guo, *Photoacoustic correlation spectroscopy and its application to low-speed flow measurement*. Optics Letters, 2010. **35**(8): p. 1200-1202.
83. Wei, C., S.W. Huang, C.R.C. Wang, and P.C. Li, *Photoacoustic flow measurements based on wash-in analysis of gold nanorods*. Ieee Transactions on Ultrasonics Ferroelectrics and Frequency Control, 2007. **54**(6): p. 1131-1141.
84. Bonnefous, O. and P. Pesque, *Time Domain Formulation of Pulse-Doppler Ultrasound and Blood Velocity Estimation by Cross-Correlation*. Ultrasonic Imaging, 1986. **8**(2): p. 73-85.
85. Rogers, D.F., *Laminar flow analysis*. 1992, Cambridge ; New York: Cambridge University Press. xiv, 422 p.
86. Cobbold, R.S.C., *Foundations of biomedical ultrasound*. Biomedical engineering series. 2007, New York: Oxford University Press. xix, 802 p.

87. Guo, Z.J., S. Hu, and L.H.V. Wang, *Calibration-free absolute quantification of optical absorption coefficients using acoustic spectra in 3D photoacoustic microscopy of biological tissue*. Optics Letters, 2010. **35**(12): p. 2067-2069.
88. Zhang, H.F., K. Maslov, M. Sivaramakrishnan, G. Stoica, and L.H.V. Wang, *Imaging of hemoglobin oxygen saturation variations in single vessels in vivo using photoacoustic microscopy*. Applied Physics Letters, 2007. **90**(5): p. 053901.
89. Yao, J., K.I. Maslov, and L.V. Wang. *Noninvasive quantification of metabolic rate of oxygen (MRO₂) by photoacoustic microscopy*. 2011. San Francisco, California, USA: SPIE.
90. Wang, Y. and R.K. Wang, *Autocorrelation optical coherence tomography for mapping transverse particle-flow velocity*. Optics Letters, 2010. **35**(21): p. 3538-3540.
91. Seyfried, T.N. and L.M. Shelton, *Cancer as a metabolic disease*. Nutrition & Metabolism, 2010. **7**(7): p. 1-22.
92. Vaupel, P., F. Kallinowski, and P. Okunieff, *Blood-Flow, Oxygen and Nutrient Supply, and Metabolic Microenvironment of Human-Tumors - a Review*. Cancer Research, 1989. **49**(23): p. 6449-6465.
93. Zhang, X. and W.D. Le, *Pathological role of hypoxia in Alzheimer's disease*. Experimental Neurology, 2010. **223**(2): p. 299-303.
94. Cheng, K., K. Ho, R. Stokes, C. Scott, S.M. Lau, W.J. Hawthorne, P.J. O'Connell, T. Loudovaris, T.W. Kay, R.N. Kulkarni, T. Okada, X.H.L. Wang, S.H. Yim, Y. Shah, S.T. Grey, A.V. Biankin, J.G. Kench, D.R. Laybutt, F.J. Gonzalez, C.R. Kahn, and J.E. Gunton, *Hypoxia-inducible factor-1 alpha regulates beta cell function in mouse and human islets*. Journal of Clinical Investigation, 2010. **120**(6): p. 2171-2183.
95. Tadros, T., D.L. Traber, and D.N. Herndon, *Hepatic blood flow and oxygen consumption after burn and sepsis*. Journal of Trauma-Injury Infection and Critical Care, 2000. **49**(1): p. 101-108.
96. Donahoe, M., R.M. Rogers, D.O. Wilson, and B.E. Pennock, *Oxygen-Consumption of the Respiratory Muscles in Normal and in Malnourished Patients with Chronic Obstructive Pulmonary-Disease*. American Review of Respiratory Disease, 1989. **140**(2): p. 385-391.
97. Bersin, R.M., C. Wolfe, M. Kwasman, D. Lau, C. Klinski, K. Tanaka, P. Khorrami, G.N. Henderson, T. Demarco, and K. Chatterjee, *Improved Hemodynamic Function and Mechanical Efficiency in Congestive-Heart-Failure with Sodium Dichloroacetate*. Journal of the American College of Cardiology, 1994. **23**(7): p. 1617-1624.
98. Marchal, G., P. Rioux, M.C. Petittaboue, G. Sette, J.M. Traverre, C. Lepoec, P. Courtheoux, J.M. Derlon, and J.C. Baron, *Regional Cerebral Oxygen-Consumption, Blood-Flow, and Blood-Volume in Healthy-Human Aging*. Archives of Neurology, 1992. **49**(10): p. 1013-1020.
99. Maquet, P., *Sleep Function(S) and Cerebral Metabolism*. Behavioural Brain Research, 1995. **69**(1-2): p. 75-83.
100. de la Zerda, A., Z.A. Liu, S. Bodapati, R. Teed, S. Vaithilingam, B.T. Khuri-Yakub, X.Y. Chen, H.J. Dai, and S.S. Gambhir, *Ultrahigh Sensitivity Carbon Nanotube Agents for Photoacoustic Molecular Imaging in Living Mice*. Nano Letters, 2010. **10**(6): p. 2168-2172.
101. Buxton, R.B. and L.R. Frank, *A model for the coupling between cerebral blood flow and oxygen metabolism during neural stimulation*. Journal of Cerebral Blood Flow and Metabolism, 1997. **17**(1): p. 64-72.

102. Guyton, A.C. and J.E. Hall, *Textbook of medical physiology*. 11th ed. 2006, Edinburgh, Oxford: Elsevier Saunders; Elsevier Science distributor. xxxv, 1116 p.
103. Frackowiak, R.S.J., G.L. Lenzi, T. Jones, and J.D. Heather, *Quantitative Measurement of Regional Cerebral Blood-Flow and Oxygen-Metabolism in Man Using O-15 and Positron Emission Tomography - Theory, Procedure, and Normal Values*. Journal of Computer Assisted Tomography, 1980. **4**(6): p. 727-736.
104. Hoge, R.D., J. Atkinson, B. Gill, G.R. Crelier, S. Marrett, and G.B. Pike, *Investigation of BOLD signal dependence on cerebral blood flow and oxygen consumption: The deoxyhemoglobin dilution model*. Magnetic Resonance in Medicine, 1999. **42**(5): p. 849-863.
105. Xu, F., Y.L. Ge, and H.Z. Lu, *Noninvasive Quantification of Whole-Brain Cerebral Metabolic Rate of Oxygen (CMRO₂) by MRI*. Magnetic Resonance in Medicine, 2009. **62**(1): p. 141-148.
106. Jain, V., M.C. Langham, and F.W. Wehrli, *MRI estimation of global brain oxygen consumption rate*. J Cereb Blood Flow Metab, 2010. **30**(9): p. 1598-607.
107. Brown, D.W., J. Hadway, and T.Y. Lee, *Near-infrared spectroscopy measurement of oxygen extraction fraction and cerebral metabolic rate of oxygen in newborn piglets*. Pediatric Research, 2003. **54**(6): p. 861-867.
108. Boas, D.A., G. Strangman, J.P. Culver, R.D. Hoge, G. Jaszewski, R.A. Poldrack, B.R. Rosen, and J.B. Mandeville, *Can the cerebral metabolic rate of oxygen be estimated with near-infrared spectroscopy?* Physics in Medicine and Biology, 2003. **48**(15): p. 2405-2418.
109. Zhou, C., R. Choe, N. Shah, T. Durduran, G. Yu, A. Durkin, D. Hsiang, R. Mehta, J. Butler, A. Cerussi, B.J. Tromberg, and A.G. Yodh, *Diffuse optical monitoring of blood flow and oxygenation in human breast cancer during early stages of neoadjuvant chemotherapy*. J Biomed Opt, 2007. **12**(5): p. 051903.
110. Yao, J.J. and L.H.V. Wang, *Transverse flow imaging based on photoacoustic Doppler bandwidth broadening*. Journal of Biomedical Optics, 2010. **15**(2): p. 021304.
111. Rebar, E.J., Y. Huang, R. Hickey, A.K. Nath, D. Meoli, S. Nath, B.L. Chen, L. Xu, Y.X. Liang, A.C. Jamieson, L. Zhang, S.K. Spratt, C.C. Case, A. Wolffe, and F.J. Giordano, *Induction of angiogenesis in a mouse model using engineered transcription factors*. Nature Medicine, 2002. **8**(12): p. 1427-1432.
112. Jain, R.K., K. Schlenger, M. Hockel, and F. Yuan, *Quantitative angiogenesis assays: Progress and problems*. Nature Medicine, 1997. **3**(11): p. 1203-1208.
113. Tammela, T., G. Zarkada, E. Wallgard, A. Murtomaki, S. Suchting, M. Wirzenius, M. Waltari, M. Hellstrom, T. Schomber, R. Peltonen, C. Freitas, A. Duarte, H. Isoniemi, P. Laakkonen, G. Christofori, S. Yla-Herttuala, M. Shibuya, B. Pytowski, A. Eichmann, C. Betsholtz, and K. Alitalo, *Blocking VEGFR-3 suppresses angiogenic sprouting and vascular network formation*. Nature, 2008. **454**(7204): p. 656-U68.
114. Eriksson, E., J.V. Boykin, and R.N. Pittman, *Method for in vivo microscopy of the cutaneous microcirculation of the hairless mouse ear*. Microvascular Research, 1980. **19**(3): p. 374-379.
115. Barker, J.H., F. Hammersen, I. Bondar, E. Uhl, T.J. Galla, M.D. Menger, and K. Messmer, *The Hairless Mouse Ear for in Vivo Studies of Skin Microcirculation*. Plastic and Reconstructive Surgery, 1989. **83**(6): p. 948-959.

116. Sivaramakrishnan, M., K. Maslov, H.F. Zhang, G. Stoica, and L.V. Wang, *Limitations of quantitative photoacoustic measurements of blood oxygenation in small vessels*. Physics in Medicine and Biology, 2007. **52**(5): p. 1349-1361.
117. Russell, E.S., E.F. Neufeld, and C.T. Higgins, *Comparison of normal blood picture of young adults from 18 inbred strains of mice*. Proceedings of the Society for Experimental Biology and Medicine, 1951. **78**(3): p. 761-766.
118. Rins, M., I. Diez, A.C. Calpena, and R. Obach, *Skin density in the hairless rat. Evidence of regional differences*. Eur J Drug Metab Pharmacokinet, 1991. **Spec No 3**: p. 456-7.
119. Dudar, T.E. and R.K. Jain, *Differential Response of Normal and Tumor Microcirculation to Hyperthermia*. Cancer Research, 1984. **44**(2): p. 605-612.
120. Rhind, S.G., G.A. Gannon, P.N. Shek, I.K.M. Brenner, Y. Severs, J. Zamecnik, A. Buguet, V.M. Natale, R.J. Shephard, and M.W. Radomski, *Contribution of exertional hyperthermia to sympathoadrenal-mediated lymphocyte subset redistribution*. Journal of Applied Physiology, 1999. **87**(3): p. 1178-1185.
121. Charkoudian, N., *Skin blood flow in adult human thermoregulation: How it works, when it does not, and why*. Mayo Clinic Proceedings, 2003. **78**(5): p. 603-612.
122. Pettigre.Rt, J.M. Galt, C.M. Ludgate, D.B. Horn, and A.N. Smith, *Circulatory and Biochemical Effects of Whole-Body Hyperthermia*. British Journal of Surgery, 1974. **61**(9): p. 727-730.
123. Perrotte, P., J. Tran, E.J. McGuire, and L.L. Pisters, *Effect of prior therapy on survival after salvage cryotherapy for recurrent prostate cancer*. Prostate Cancer and Prostatic Diseases, 1999. **2**(S3): p. S25-S25.
124. Holt, P.J.A., *Cryotherapy for Skin-Cancer - Results over a 5-Year Period Using Liquid-Nitrogen Spray Cryosurgery*. British Journal of Dermatology, 1988. **119**(2): p. 231-240.
125. Joosten, J.J.A., G.N.P. van Muijen, T. Wobbes, and T.J.M. Ruers, *In vivo destruction of tumor tissue by cryoablation can induce inhibition of secondary tumor growth: An experimental study*. Cryobiology, 2001. **42**(1): p. 49-58.
126. Mahabeleshwar, G.H. and T.V. Byzova, *Angiogenesis in melanoma*. Semin Oncol, 2007. **34**(6): p. 555-65.
127. Sutherland, R.M., *Cell and Environment Interactions in Tumor Microregions - the Multicell Spheroid Model*. Science, 1988. **240**(4849): p. 177-184.
128. Harris, A.L., *Hypoxia - A key regulatory factor in tumour growth*. Nature Reviews Cancer, 2002. **2**(1): p. 38-47.
129. Pouyssegur, J., F. Dayan, and N.M. Mazure, *Hypoxia signalling in cancer and approaches to enforce tumour regression*. Nature, 2006. **441**(7092): p. 437-443.
130. Zhang, C., K. Maslov, and L.V. Wang, *Subwavelength-resolution label-free photoacoustic microscopy of optical absorption in vivo*. Opt Lett, 2010. **35**(19): p. 3195-7.
131. Wang, L., K. Maslov, J. Yao, B. Rao, and L.V. Wang, *Fast voice-coil scanning optical-resolution photoacoustic microscopy*. Opt Lett, 2011. **36**(2): p. 139-41.
132. Xie, Z.X., S.L. Jiao, H.F. Zhang, and C.A. Puliafito, *Laser-scanning optical-resolution photoacoustic microscopy*. Optics Letters, 2009. **34**(12): p. 1771-1773.
133. Abtahian, F., A. Guerriero, E. Sebzda, M.M. Lu, R. Zhou, A. Mocsa, E.E. Myers, B. Huang, D.G. Jackson, V.A. Ferrari, V. Tybulewicz, C.A. Lowell, J.J. Lepore, G.A. Koretzky, and M.L. Kahn, *Regulation of blood and lymphatic vascular separation by signaling proteins SLP-76 and Syk*. Science, 2003. **299**(5604): p. 247-251.

134. Whitworth, P.W., H.M. Cryer, R.N. Garrison, T.E. Baumgarten, and P.D. Harris, *Hypoperfusion of the Intestinal Microcirculation without Decreased Cardiac-Output during Live Escherichia-Coli Sepsis in Rats*. Circulatory Shock, 1989. **27**(2): p. 111-122.
135. Rao, B., K. Maslov, A. Danielli, R.M. Chen, K.K. Shung, Q.F. Zhou, and L.V. Wang, *Real-time four-dimensional optical-resolution photoacoustic microscopy with Au nanoparticle-assisted subdiffraction-limit resolution*. Optics Letters, 2011. **36**(7): p. 1137-1139.
136. Hajireza, P., W. Shi, and R.J. Zemp, *Label-free in vivo fiber-based optical-resolution photoacoustic microscopy*. Optics Letters, 2011. **36**(20): p. 4107-4109.
137. Wang, L.D., K. Maslov, J. Yao, B. Rao, and L.H.V. Wang, *Fast voice-coil scanning optical-resolution photoacoustic microscopy*. Optics Letters, 2011. **36**(2): p. 139-141.
138. Song, L., K. Maslov, and L.V. Wang, *Multifocal optical-resolution photoacoustic microscopy in vivo*. Optics Letters, 2011. **36**(7): p. 1236-1238.
139. Rao, B., L. Li, K. Maslov, and L.H. Wang, *Hybrid-scanning optical-resolution photoacoustic microscopy for in vivo vasculature imaging*. Optics Letters, 2010. **35**(10): p. 1521-1523.
140. Wang, L.D., K. Maslov, J.J. Yao, B. Rao, and L.H.V. Wang, *Fast voice-coil scanning optical-resolution photoacoustic microscopy*. Optics Letters, 2011. **36**(2): p. 139-141.
141. Oladipupo, S., S. Hu, J. Kovalski, J.J. Yao, A. Santeford, R.E. Sohn, R. Shohet, K. Maslov, L.H.V. Wang, and J.M. Arbeit, *VEGF is essential for hypoxia-inducible factor-mediated neovascularization but dispensable for endothelial sprouting*. Proceedings of the National Academy of Sciences of the United States of America, 2011. **108**(32): p. 13264-13269.
142. Oladipupo, S.S., S. Hu, A.C. Santeford, J.J. Yao, J.R. Kovalski, R.V. Shohet, K. Maslov, L.V. Wang, and J.M. Arbeit, *Conditional HIF-1 induction produces multistage neovascularization with stage-specific sensitivity to VEGFR inhibitors and myeloid cell independence*. Blood, 2011. **117**(15): p. 4142-4153.
143. Bitton, R., R. Zemp, J. Yen, L.V. Wang, and K.K. Shung, *A 3-D high-frequency array based 16 channel photoacoustic microscopy system for in vivo micro-vascular imaging*. IEEE Trans Med Imaging, 2009. **28**(8): p. 1190-1197.
144. Staley, J., P. Grogan, A.K. Samadi, H. Cui, M.S. Cohen, and X. Yang, *Growth of melanoma brain tumors monitored by photoacoustic microscopy*. Journal of Biomedical Optics, 2010. **15**(4): p. 040510.
145. Cui, H.Z. and X.M. Yang, *In vivo imaging and treatment of solid tumor using integrated photoacoustic imaging and high intensity focused ultrasound system*. Medical Physics, 2010. **37**(9): p. 4777-4781.
146. Li, L., H.F. Zhang, R.J. Zemp, K. Maslov, and L. Wang, *Simultaneous imaging of a lacZ-marked tumor and microvasculature morphology in vivo by dual-wavelength photoacoustic microscopy*. J Innov Opt Health Sci, 2008. **1**(2): p. 207-215.
147. Li, M.L., J.C. Wang, J.A. Schwartz, K.L. Gill-Sharp, G. Stoica, and L.H.V. Wang, *In-vivo photoacoustic microscopy of nanoshell extravasation from solid tumor vasculature*. Journal of Biomedical Optics, 2009. **14**(1): p. 010507.
148. Li, M., J.-T. Oh, X. Xie, G. Ku, W. Wang, C. Li, G. Lungu, G. Stoica, and L.V. Wang, *Simultaneous Molecular and Hypoxia Imaging of Brain Tumors In Vivo Using Spectroscopic Photoacoustic Tomography*. Proceedings of the IEEE, 2008. **96**(3): p. 481-489.

149. Olafsson, R., D.R. Bauer, L.G. Montilla, and R.S. Witte, *Real-time, contrast enhanced photoacoustic imaging of cancer in a mouse window chamber*. Optics Express, 2010. **18**(18): p. 18625-18632.
150. Wang, X.D., G. Ku, M.A. Wegiel, D.J. Bornhop, G. Stoica, and L.H.V. Wang, *Noninvasive photoacoustic angiography of animal brains in vivo with near-infrared light and an optical contrast agent*. Optics Letters, 2004. **29**(7): p. 730-732.
151. Liao, L.D., M.L. Li, H.Y. Lai, Y.Y.I. Shih, Y.C. Lo, S.N. Tsang, P.C.P. Chao, C.T. Lin, F.S. Jaw, and Y.Y. Chen, *Imaging brain hemodynamic changes during rat forepaw electrical stimulation using functional photoacoustic microscopy*. Neuroimage, 2010. **52**(2): p. 562-570.
152. Tsytsarev, V., S. Hu, J. Yao, K. Maslov, D.L. Barbour, and L.V. Wang, *Photoacoustic microscopy of microvascular responses to cortical electrical stimulation*. Journal of Biomedical Optics, 2011. **16**(7): p. 076002.
153. Hu, S., B. Rao, K. Maslov, and L.V. Wang, *Label-free photoacoustic ophthalmic angiography*. Optics Letters, 2010. **35**(1): p. 1-3.
154. Jiao, S.L., M.S. Jiang, J.M. Hu, A. Fawzi, Q.F. Zhou, K.K. Shung, C.A. Puliafito, and H.F. Zhang, *Photoacoustic ophthalmoscopy for in vivo retinal imaging*. Optics Express, 2010. **18**(4): p. 3967-3972.
155. Silverman, R.H., F. Kong, Y.C. Chen, H.O. Lloyd, H.H. Kim, J.M. Cannata, K.K. Shung, and D.J. Coleman, *High-resolution photoacoustic imaging of ocular tissues*. Ultrasound Med Biol, 2010. **36**(5): p. 733-742.
156. Song, W., Q. Wei, T. Liu, D. Kuai, J.M. Burke, S. Jiao, and H.F. Zhang, *Integrating photoacoustic ophthalmoscopy with scanning laser ophthalmoscopy, optical coherence tomography, and fluorescein angiography for a multimodal retinal imaging platform*. Journal of Biomedical Optics, 2012. **17**(6): p. 061206-7.
157. Zhang, H.F., K. Maslov, M.L. Li, G. Stoica, and L.H.V. Wang, *In vivo volumetric imaging of subcutaneous microvasculature by photoacoustic microscopy*. Optics Express, 2006. **14**(20): p. 9317-9323.
158. Favazza, C., K. Maslov, L. Cornelius, and L.V. Wang, *In vivo functional human imaging using photoacoustic microscopy: response to ischemic and thermal stimuli*. in *Proc. SPIE 7564*. 2010. San Francisco, California, USA: SPIE.
159. Favazza, C.P., L.A. Cornelius, and L.H.V. Wang, *In vivo functional photoacoustic microscopy of cutaneous microvasculature in human skin*. Journal of Biomedical Optics, 2011. **16**(2): p. 026004.
160. Favazza, C., O. Jassim, L.V. Wang, and L. Cornelius, *In vivo photoacoustic microscopy of human skin*. Journal of Investigative Dermatology, 2010. **130**: p. S145.
161. Song, L.A., K. Maslov, K.K. Shung, and L.H.V. Wang, *Ultrasound-array-based real-time photoacoustic microscopy of human pulsatile dynamics in vivo*. Journal of Biomedical Optics, 2010. **15**(2): p. 021303.
162. Yang, J.-M., R. Chen, C. Favazza, J. Yao, Q. Zhou, K.K. Shung, and L.V. Wang, *A 2.5-mm outer diameter photoacoustic endoscopic mini-probe based on a highly sensitive PMN-PT ultrasonic transducer*. in *Proc. SPIE 8223*. 2012. San Francisco, California, USA: SPIE.
163. Yang, J.-M., C. Favazza, R. Chen, J. Yao, X. Cai, K. Maslov, Q. Zhou, K.K. Shung, and L.V. Wang, *Toward dual-wavelength functional photoacoustic endoscopy: laser and*

- peripheral optical systems development*. in *Proc. SPIE 8223*. 2012. San Francisco, California, USA: SPIE.
164. Yao, J., K.I. Maslov, E.R. Puckett, K.J. Rowland, B.W. Warner, and L.V. Wang, *Double-illumination photoacoustic microscopy*. Optics Letters, 2012. **37**(4): p. 659-661.
 165. Yao, J., K.J. Rowland, L. Wang, K.I. Maslov, B.W. Warner, and L.V. Wang. *Double-illumination photoacoustic microscopy of intestinal hemodynamics following massive small bowel resection*. in *Proc. SPIE 8223*. 2012. San Francisco, California, USA: SPIE.
 166. Rowland, K.J., J.J. Yao, L.D. Wang, C.R. Erwin, K.I. Maslov, L.H.V. Wang, and B.W. Warner, *Immediate alterations in intestinal oxygen saturation and blood flow after massive small bowel resection as measured by photoacoustic microscopy*. Journal of Pediatric Surgery, 2012. **47**(6): p. 1143-1149.
 167. Taruttis, A., E. Herzog, D. Razansky, and V. Ntziachristos, *Real-time imaging of cardiovascular dynamics and circulating gold nanorods with multispectral optoacoustic tomography*. Optics Express, 2010. **18**(19): p. 19592-19602.
 168. Wang, B., J.L. Su, A.B. Karpouk, K.V. Sokolov, R.W. Smalling, and S.Y. Emelianov, *Intravascular Photoacoustic Imaging*. Ieee Journal of Selected Topics in Quantum Electronics, 2010. **16**(3): p. 588-599.
 169. Zemp, R.J., L. Song, R. Bitton, K.K. Shung, and L.V. Wang, *Realtime Photoacoustic Microscopy of Murine Cardiovascular Dynamics*. Optics Express, 2008. **16**(22): p. 18551-18556.
 170. Helmrath, M.A., W.E. VanderKolk, G. Can, C.R. Erwin, and B.W. Warner, *Intestinal adaptation following massive small bowel resection in the mouse*. Journal of the American College of Surgeons, 1996. **183**(5): p. 441-449.
 171. Taylor, J.A., C.A. Martin, R. Nair, J. Guo, C.R. Erwin, and B.W. Warner, *Lessons learned: optimization of a murine small bowel resection model*. Journal of Pediatric Surgery, 2008. **43**(6): p. 1018-1024.
 172. McDuffie, L.A., B.T. Bucher, C.R. Erwin, D. Wakeman, F.V. White, and B.W. Warner, *Intestinal adaptation after small bowel resection in human infants*. Journal of Pediatric Surgery, 2011. **46**(6): p. 1045-1051.
 173. Folkman, J., *Is angiogenesis an organizing principle in biology and medicine?* Journal of Pediatric Surgery, 2007. **42**(1): p. 1-11.
 174. Folkman, J., M. Bach, J.W. Rowe, F. Davidoff, P. Lambert, C. Hirsch, A. Goldberg, H.H. Hiatt, J. Glass, and E. Henshaw, *Tumor Angiogenesis - Therapeutic Implications*. New England Journal of Medicine, 1971. **285**(21): p. 1182-&.
 175. Lee, K.D., A. Yamataka, Y. Kato, Y. Kojima, N. Sueyoshi, G.J. Lane, H. Kobayashi, and T. Miyano, *Basic fibroblast growth factor and granulocyte colony-stimulating factor enhance mucosal surface expansion after adult small bowel transplantation without vascular reconstruction in rats*. Journal of Pediatric Surgery, 2006. **41**(4): p. 737-741.
 176. Parvadia, J.K., S.G. Keswani, S. Vaikunth, A.R. Maldonado, A. Marwan, W. Stehr, C. Erwin, E. Uzvolgyi, B.W. Warner, S. Yamano, N. Taichman, and T.M. Crombleholme, *Role of VEGF in small bowel adaptation after resection: the adaptive response is angiogenesis dependent*. American Journal of Physiology-Gastrointestinal and Liver Physiology, 2007. **293**(3): p. G591-G598.
 177. Martin, C.A., E.E. Perrone, S.W. Longshore, P. Toste, K. Bitter, R. Nair, J. Guo, C.R. Erwin, and B.W. Warner, *Intestinal resection induces angiogenesis within adapting intestinal villi*. Journal of Pediatric Surgery, 2009. **44**(6): p. 1077-1083.

178. McMellen, M.E., D. Wakeman, C.R. Erwin, J. Guo, and B.W. Warner, *Epidermal growth factor receptor signaling modulates chemokine (CXC) ligand 5 expression and is associated with villus angiogenesis after small bowel resection*. *Surgery*, 2010. **148**(2): p. 364-70.
179. Ulrich-Baker, M.G., M.E. Hollwarth, P.R. Kvietys, and D.N. Granger, *Blood flow responses to small bowel resection*. *Am J Physiol*, 1986. **251**(6 Pt 1): p. G815-22.
180. Touloukian, R.J. and R.P. Spencer, *Ileal blood flow preceding compensatory intestinal hypertrophy*. *Ann Surg*, 1972. **175**(3): p. 320-5.
181. Jessephe, J.E. and A.J. Jacklin, *Effects of Partial Resection of Mammalian Small Intestine. Iii. Glucose Absorption, Co2 Production and Blood Flow in Residual Ileum in the Dog*. *Rev Surg*, 1963. **20**: p. 384-7.
182. Cassavaugh, J. and K.M. Lounsbury, *Hypoxia-mediated biological control*. *J Cell Biochem*, 2011. **112**(3): p. 735-44.
183. Karhausen, J., G.T. Furuta, J.E. Tomaszewski, R.S. Johnson, S.P. Colgan, and V.H. Haase, *Epithelial hypoxia-inducible factor-1 is protective in murine experimental colitis*. *Journal of Clinical Investigation*, 2004. **114**(8): p. 1098-1106.
184. Carew, T.J., *Behavioral neurobiology : the cellular organization of natural behavior*. 2000, Sunderland, Mass.: Sinauer Associates Publishers. ix, 435 p.
185. Nieuwenhuys, R., H.J.t. Donkelaar, C. Nicholson, W.J.A.J. Smeets, and H. Wicht, *The central nervous system of vertebrates. Volume 1*. 1998, Berlin ; New York: Springer. xii, 757 p.
186. Mink, J.W., R.J. Blumenshine, and D.B. Adams, *Ratio of Central Nervous-System to Body Metabolism in Vertebrates - Its Constancy and Functional Basis*. *American Journal of Physiology*, 1981. **241**(3): p. R203-R212.
187. Fulham, M.J., A. Bizzi, M.J. Dietz, H.H.L. Shih, R. Raman, G.S. Sobering, J.A. Frank, A.J. Dwyer, J.R. Alger, and G. Dichiro, *Mapping of Brain-Tumor Metabolites with Proton Mr Spectroscopic Imaging - Clinical Relevance*. *Radiology*, 1992. **185**(3): p. 675-686.
188. Mosconi, L., R. Mistur, R. Switalski, W.H. Tsui, L. Glodzik, Y. Li, E. Pirraglia, S. De Santi, B. Reisberg, T. Wisniewski, and M.J. de Leon, *FDG-PET changes in brain glucose metabolism from normal cognition to pathologically verified Alzheimer's disease*. *European Journal of Nuclear Medicine and Molecular Imaging*, 2009. **36**(5): p. 811-822.
189. Raichle, M.E. and D.A. Gusnard, *Appraising the brain's energy budget*. *Proceedings of the National Academy of Sciences of the United States of America*, 2002. **99**(16): p. 10237-10239.
190. Schlemmer, H.P.W., B.J. Pichler, M. Schmand, Z. Burbar, C. Michel, R. Ladebeck, K. Jattke, D. Townsend, C. Nahmias, P.K. Jacob, W.D. Heiss, and C.D. Claussen, *Simultaneous MR/PET imaging of the human brain: Feasibility study*. *Radiology*, 2008. **248**(3): p. 1028-1035.
191. Mehagnoul-Schipper, D.J., B.F.W. van der Kallen, W.N.J.M. Colier, M.C. van der Sluijs, L.J.T.O. van Erning, H.O.M. Thijssen, B. Oeseburg, W.H.L. Hoefnagels, and R.W.M.M. Jansen, *Simultaneous measurements of cerebral oxygenation changes during brain activation by near-infrared spectroscopy and functional magnetic resonance imaging in healthy young and elderly subjects*. *Human Brain Mapping*, 2002. **16**(1): p. 14-23.

192. Itoh, Y., T. Abe, R. Takaoka, and N. Tanahashi, *Fluorometric determination of glucose utilization in neurons in vitro and in vivo*. Journal of Cerebral Blood Flow and Metabolism, 2004. **24**(9): p. 993-1003.
193. Cho, E.C., C. Kim, F. Zhou, C.M. Cobley, K.H. Song, J.Y. Chen, Z.Y. Li, L.H.V. Wang, and Y.N. Xia, *Measuring the Optical Absorption Cross Sections of Au-Ag Nanocages and Au Nanorods by Photoacoustic Imaging*. Journal of Physical Chemistry C, 2009. **113**(21): p. 9023-9028.
194. Zhang, H.F., K. Maslov, G. Stoica, and L.V. Wang, *Functional photoacoustic microscopy for high-resolution and noninvasive in vivo imaging*. Nature Biotechnology, 2006. **24**(7): p. 848-51.
195. Li, M.L., J.T. Oh, X.Y. Xie, G. Ku, W. Wang, C. Li, G. Lungu, G. Stoica, and L.V. Wang, *Simultaneous molecular and hypoxia imaging of brain tumors in vivo using spectroscopic photoacoustic tomography*. Proceedings of the Ieee, 2008. **96**(3): p. 481-489.
196. Li, C.H., A. Aguirre, J. Gamelin, A. Maurudis, Q. Zhu, and L.V. Wang, *Real-time photoacoustic tomography of cortical hemodynamics in small animals*. Journal of Biomedical Optics, 2010. **15**(1).
197. Xia, J., Z.J. Guo, K. Maslov, A. Aguirre, Q. Zhu, C. Percival, and L.H.V. Wang, *Three-dimensional photoacoustic tomography based on the focal-line concept*. Journal of Biomedical Optics, 2011. **16**(9).
198. Bem, M., F. Badea, C. Draghici, M.T. Caproiu, M. Vasilescu, M. Voicescu, A. Beteringhe, A. Caragheorgheopol, M. Maganu, T. Constantinescu, and A.T. Balaban, *Synthesis and properties of some new 4-amino-7 nitrobenzoxadiazole derivatives*. ARKIVOC, 2007. **2007**(xiii): p. 87-104.
199. Cheng, Z., J. Levi, Z.M. Xiong, O. Gheysens, S. Keren, X.Y. Chen, and S.S. Gambhir, *Near-infrared fluorescent deoxyglucose analogue for tumor optical imaging in cell culture and living mice*. Bioconjugate Chemistry, 2006. **17**(3): p. 662-669.
200. Gaudreault, N., D.R.L. Scriven, I. Laher, and E.D.W. Moore, *Subcellular characterization of glucose uptake in coronary endothelial cells*. Microvascular Research, 2008. **75**(1): p. 73-82.
201. Langsner, R.J., L.P. Middleton, J. Sun, F. Meric-Bernstam, K.K. Hunt, R.A. Drezek, and T.K. Yu, *Wide-field imaging of fluorescent deoxy-glucose in ex vivo malignant and normal breast tissue*. Biomedical Optics Express, 2011. **2**(6): p. 1514-1523.
202. Millon, S.R., J.H. Ostrander, J.Q. Brown, A. Raheja, V.L. Seewaldt, and N. Ramanujam, *Uptake of 2-NBDG as a method to monitor therapy response in breast cancer cell lines*. Breast Cancer Research and Treatment, 2011. **126**(1): p. 55-62.
203. O'Neil, R.G., L. Wu, and N. Mullani, *Uptake of a fluorescent deoxyglucose analog (2-NBDG) in tumor cells*. Molecular Imaging and Biology, 2005. **7**(6): p. 388-392.
204. Sheth, R.A., L. Josephson, and U. Mahmood, *Evaluation and clinically relevant applications of a fluorescent imaging analog to fluorodeoxyglucose positron emission tomography*. Journal of Biomedical Optics, 2009. **14**(6).
205. Tsytsarev, V., K.I. Maslov, J.J. Yao, A.R. Parameswar, A.V. Demchenko, and L.H.V. Wang, *In vivo imaging of epileptic activity using 2-NBDG, a fluorescent deoxyglucose analog*. Journal of Neuroscience Methods, 2012. **203**(1): p. 136-140.

206. Gamelin, J., A. Maurudis, A. Aguirre, F. Huang, P.Y. Guo, L.V. Wang, and Q. Zhu, *A real-time photoacoustic tomography system for small animals*. Optics Express, 2009. **17**(13): p. 10489-10498.
207. Xu, M.H. and L.V. Wang, *Universal back-projection algorithm for photoacoustic computed tomography (vol 71, art no 016706, 2005)*. Physical Review E, 2007. **75**(5).
208. Yao, J., K. Maslov, S. Hu, and L.V. Wang, *Evans blue dye-enhanced capillary-resolution photoacoustic microscopy in vivo*. Journal of Biomedical Optics, 2009. **14**(5): p. 054049.
209. Wang, L.V. and H.-i. Wu, *Biomedical optics : principles and imaging*. 2007, Hoboken, N.J.: Wiley-Interscience. xiv, 362 p.
210. Vishwanath, K., H. Yuan, W.T. Barry, M.W. Dewhurst, and N. Ramanujam, *Using Optical Spectroscopy to Longitudinally Monitor Physiological Changes within Solid Tumors*. Neoplasia, 2009. **11**(9): p. 889-900.
211. Azzi, L., M. El-Alfy, C. Martel, and F. Labrie, *Gender differences in mouse skin morphology and specific effects of sex steroids and dehydroepiandrosterone*. Journal of Investigative Dermatology, 2005. **124**(1): p. 22-27.
212. Natarajan, A. and F. Srienc, *Dynamics of glucose uptake by single Escherichia coli cells*. Metab Eng, 1999. **1**(4): p. 320-33.
213. Sheinfeld, A. and A. Eyal. *Flow-dependant photothermal modulation of the photoacoustic response*. 2012. San Francisco, California, USA: SPIE.
214. Liu, Z.H.M., K.F. Schmidt, K.M. Sicard, and T.Q. Duong, *Imaging oxygen consumption in forepaw somatosensory stimulation in rats under isoflurane anesthesia*. Magnetic Resonance in Medicine, 2004. **52**(2): p. 277-285.
215. Mandeville, J.B., J.J.A. Marota, B.E. Kosofsky, J.R. Keltner, R. Weissleder, B.R. Rosen, and R.M. Weisskoff, *Dynamic functional imaging of relative cerebral blood volume during rat forepaw stimulation*. Magnetic Resonance in Medicine, 1998. **39**(4): p. 615-624.
216. Ogawa, M., Y. Magata, Y. Ouchi, H. Fukuyama, H. Yamauchi, J. Kimura, Y. Yonekura, and J. Konishi, *Scopolamine Abolishes Cerebral Blood-Flow Response to Somatosensory Stimulation in Anesthetized Cats - Pet Study*. Brain Research, 1994. **650**(2): p. 249-252.
217. Zhang, H.F., J. Wang, Q. Wei, T. Liu, S.L. Jiao, and C.A. Puliafito, *Collecting back-reflected photons in photoacoustic microscopy*. Optics Express, 2010. **18**(2): p. 1278-1282.
218. Zhang, X., M. Jiang, A.A. Fawzi, X. Li, K.K. Shung, C.A. Puliafito, H.F. Zhang, and S. Jiao, *Simultaneous dual molecular contrasts provided by the absorbed photons in photoacoustic microscopy*. Opt. Lett., 2010. **35**(23): p. 4018-4020.
219. Li, L., K. Maslov, G. Ku, and L.V. Wang, *Three-dimensional combined photoacoustic and optical coherence microscopy for in vivo microcirculation studies*. Optics Express, 2009. **17**(19): p. 16450-16455.
220. van Raaij, M.E., M. Lee, E. Cherin, B. Stefanovic, and F.S. Foster. *Femtosecond photoacoustics: integrated two-photon fluorescence and photoacoustic microscopy*. 2010. San Francisco, California, USA: SPIE.
221. Harrison, T., J. Ranasinghesagara, H. Lu, and R.J. Zemp. *Fast-scanning ultrasonic-photoacoustic biomicroscope: in vivo performance*. 2010. San Francisco, California, USA: SPIE.

222. Niederhauser, J.J., M. Jaeger, R. Lemor, P. Weber, and M. Frenz, *Combined ultrasound and optoacoustic system for real-time high-contrast vascular imaging in vivo*. IEEE Transactions on Medical Imaging, 2005. **24**(4): p. 436-440.
223. Li, W.Y., X. Cai, C.H. Kim, G.R. Sun, Y. Zhang, R. Deng, M.X. Yang, J.Y. Chen, S. Achilefu, L.V. Wang, and Y.N. Xia, *Gold nanocages covered with thermally-responsive polymers for controlled release by high-intensity focused ultrasound*. Nanoscale, 2011. **3**(4): p. 1724-1730.
224. Akers, W.J., C. Kim, M. Berezin, K. Guo, R. Fuhrhop, G.M. Lanza, G.M. Fischer, E. Daltrozzo, A. Zumbusch, X. Cai, L.V. Wang, and S. Achilefu, *Noninvasive photoacoustic and fluorescence sentinel lymph node identification using dye-loaded perfluorocarbon nanoparticles*. Acs Nano, 2011. **5**(1): p. 173-182.
225. Yang, J.M., K. Maslov, H.C. Yang, Q.F. Zhou, K.K. Shung, and L.H.V. Wang, *Photoacoustic endoscopy*. Optics Letters, 2009. **34**(10): p. 1591-1593.
226. Ye, S.Q., R. Yang, J.W. Xiong, K.K. Shung, Q.F. Zhou, C.H. Li, and Q.S. Ren, *Label-free imaging of zebrafish larvae in vivo by photoacoustic microscopy*. Biomedical Optics Express, 2012. **3**(2): p. 360-365.
227. Yang, J.-M., C. Favazza, R. Chen, J. Yao, X. Cai, K. Maslov, Q. Zhou, K.K. Shung, and L.V. Wang. *Toward dual-wavelength functional photoacoustic endoscopy: laser and peripheral optical systems development*. 2012. San Francisco, California, USA: SPIE.
228. Wei, W., X. Li, Q.F. Zhou, K.K. Shung, and Z.P. Chen, *Integrated ultrasound and photoacoustic probe for co-registered intravascular imaging*. Journal of Biomedical Optics, 2011. **16**(10): p. 106001.
229. Karpiouk, A.B., B. Wang, and S.Y. Emelianov, *Development of a catheter for combined intravascular ultrasound and photoacoustic imaging*. Review of Scientific Instruments, 2010. **81**(1): p. 014901.
230. Yang, J.M., C. Favazza, R.M. Chen, J.J. Yao, X. Cai, K. Maslov, Q.F. Zhou, K.K. Shung, and L.H.V. Wang, *Simultaneous functional photoacoustic and ultrasonic endoscopy of internal organs in vivo*. Nature Medicine, 2012. **18**(8): p. 1297-1303.
231. Yang, J.-M., R. Chen, C. Favazza, J. Yao, C. Li, Z. Hu, Q. Zhou, K.K. Shung, and L.V. Wang, *A 2.5-mm diameter probe for photoacoustic and ultrasonic endoscopy*. Opt. Express, 2012. **20**(21): p. 23944-23953.
232. Zhang, E.Z. and P.C. Beard. *A miniature all-optical photoacoustic imaging probe*. 2011. San Francisco, California, USA: SPIE.
233. Hasegawa, N., Y. Niwa, T. Arisawa, S. Hase, H. Goto, and T. Hayakawa, *Preoperative staging of superficial esophageal carcinoma: comparison of an ultrasound probe and standard endoscopic ultrasonography*. Gastrointestinal Endoscopy, 1996. **44**(4): p. 388-93.